A Study on Improvement of Tensile and Fatigue Properties of Type 316 Austenitic Stainless Steel by High-Density Pulsed Electric Current

Department of Micro-Nano Mechanical Science and Engineering
Nagoya University

Sungmin Yoon

List of contents

List of contents I

Abbreviation V

Nomenclature VI

Chapter 1 Introduction

1.1 Background 1

1.1.1 General stainless steels 1

1.1.2 Type 316 austenitic stainless steel and its problem 3

1.2 Strength of materials and fracture mechanics 5

1.2.1 Tensile fracture 5

1.2.2 Fatigue fracture 8

1.3 Effect of electric current in metals 10

1.4 Research objectives 12

1.5 Thesis organization 15

References 16

Chapter 2 Experimental and simulation approach

2.1 Material and sample preparation 22

2.2 Investigation of mechanical properties 22

2.2.1 Tensile tests 23

2.2.2 Fatigue tests 24

2.3 Application of HDPEC 25

2.4 Microstructure observation 25

2.5 Formulation of finite element analysis 27

References 28

Chapter 3 Tensile fracture behavior modified by HDPEC

3.1 Introduction 29

3.2 Analysis procedure 30

3.2.1 Tensile test 31

3.2.2 Finite element analysis 32

3.3 Results 33

3.3.1 Evaluation of fracture toughness 33

3.3.2 Improved fracture thresholds 36

3.3.3 Evaluation by crack profiles 40

3.4 Discussion 42

3.4.1 Evaluation of improved fracture parameters 43

3.4.2 Strengthening role of HDPEC 44

3.5 Summary 44

References 45

Chapter 4 Material strengthening through the modification of microstructure

4.1 Introduction 49

4.2 Tensile tests under controlled temperature rising 52

4.3 Results 53

4.3.1 Grain boundary characteristics and grain refinement 53

4.3.2 Effect of pulse number 55

4.3.3 Dissolution of $Cr_{23}C_6$ 60

4.4 Discussion 63

4.4.1 Strengthening mechanism 63

4.4.2 Reduction of $Cr_{23}C_6$ 65

4.4.3 Role of EWF 66

4.5 Summary 67

References 68

Chapter 5 Low-cycle fatigue behavior improved by HDPECs

5.1 Introduction 72

5.2 Application methods of HDPEC for fatigue tests 74

5.3 Results 76

5.3.1 Fatigue crack growth behavior 76

5.3.2 Low-cycle fatigue properties 78

5.3.3 Fractography 85

5.3.4 Pitch effect 87

5.4 Discussion 89

5.4.1 Delay in fatigue crack growth 89

5.4.2 Effectiveness of multiple HDPECs 89

5.5 Summary 90

References 91

Chapter 6 Fatigue crack healing based on crack-tip temperature-controlled method

6.1 Introduction 96

6.2 Investigation of temperature-controlled fatigue crack healing 99

6.3 Results 101

6.3.1 Measured raised temperature 101

6.3.2 Fatigue crack healing 103

6.3.3 Evaluation of efficiency of fatigue crack healing ……..... 110

6.4 Discussion 111

6.4.1 Microstructure features 111

6.4.2 Efficiency of fatigue crack healing 112

6.4.3 Irregularity from over-application of HDPEC 112

6.5 Summary 113

References 114

Chapter 7 Conclusions 117

Acknowledgements 120

Abbreviation

BMC	Basquin-Manson-Coffin	HDPEC	high-density pulsed electric current
COD	crack opening displacement	IPFs	inverse pole figures
CSA	cross-section area	LAGBs	low angle grain boundaries
CSL	coincidence site lattice	LCF	low-cycle fatigue
CTOD	crack tip opening displacement	LEFM	linear elastic fracture mechanics
EBSD	electron backscatter diffraction	ND	normal direction
EDM	electro-discharge machining	PFs	pole figures
EDS	energy-dispersive X-ray spectroscopy	RD	rolling direction
EWF	electron wind force	SAED	selected area electron diffraction
FCG	fatigue crack growth	SIF	stress intensity factor
FEA	finite element analysis	SSY	small-scale yielding
FESEM	field-emission scanning electron microscopy	STEM	scanning transmission electron microscopy
GBs	grain boundaries	SWT	Smith-Watson-Topper
GBCD	grain boundary characteristics distribution	TBs	twin boundaries
GBE	grain boundary engineering	TD	transverse direction
HAGBs	high angle grain boundaries	TEM	transmission electron microscopy
HCF	high-cycle fatigue		

Nomenclature

a	actual crack length	K_c	fracture toughness
a^*	effective crack length	K_ε	strain intensity factor
a_c	critical crack length	ΔK_ε	strain intensity factor range
a_c^*	plasticity-corrected critical crack length	l_s	period lengths of striations
a/w	crack length per sample width	m	strain hardening coefficient
da/dN	fatigue crack growth rate	N	number of fatigue cycles
$B.\sigma_p$	interior plastic term	N_d	dislocation density
C_p	specific heat capacity	N_f	fatigue life
d	displacement	$2N_f$	number of reversals to failure
d_m	density of a material	N_I	increased fatigue cycles
E, $\mathbb{E}$, E_{ijkl}	elastic modulus	$N_i\ (x)$	interpolation function
e	electron charge	N_p	cycle pitch
F	external force	N_s	stop cycles
F_{EW}	electron wind force	n	strain hardening exponent
F^R	reaction nodal force	n_e	electron density
F^S	surface nodal force	p	number of pulses
F^V	volumetric nodal force	R	stress or strain ratio
f_Ω	domain force	r	distance from crack tip
j	current density	r_y	length of plastic yielding zone
ΔK	stress intensity factor range	T	temperature
K^e	elastic stiffness	ΔT_{ct}	crack tip temperature rising
K	stress intensity factor in mode I fracture	ΔT_J	temperature rising

T_{R}	raised temperature	ρ	electrical resistivity
T_{r}	room temperature	ρ_{d}	specific resistivity due to dislocation
T_{s}	surface force	σ	stress field
t_{d}	duration time of current	σ_a	applied or alternating stress
U	displacement in mesh nodes	σ_{ac}	critical applied stress
u	displacement field	σ_{cm}	critical von Mises stress
$\nabla_{\mathrm{s}} u$	symmetric gradient from u	σ_{f}'	fatigue strength
v^{h}	displacement field of mesh	σ_{ij}	triaxial state stress
v_{i}	discretized displacement field	σ_{max}	maximum stress
δ	crack tip opening displacement	σ_{min}	minimum stress
δ_{c}	critical crack tip opening displacement	σ_{p}	plastic stress
$\Delta\varepsilon$	total strain range	σ_{s}	stress at fatigue stop
ε_a	strain amplitude	σ_{u}	ultimate strength
$\varepsilon_a^{\mathrm{e}}$	elastic strain amplitude	σ_{vm}	von Mises stress
$\varepsilon_a^{\mathrm{p}}$	plastic strain amplitude	σ_{y}	yield stress
ε_{f}	strain at fracture	σ_∞	remote tensile stress
$\varepsilon_{\mathrm{f}}'$	ductility coefficient	$\sigma_1, \sigma_2, \sigma_3$	principal stresses
$\varepsilon_{\mathrm{ij}}^{\mathrm{e}}$	elastic strain	Ω	material domain
$\varepsilon_{\mathrm{ij}}^{\mathrm{p}}$	plastic strain	$\partial\Omega_{\mathrm{d}}$	boundary of displacement
$\varepsilon_{\mathrm{max}}$	maximum strain	Ω^{h}	mesh domain
$\varepsilon_{\mathrm{min}}$	minimum strain	$\partial\Omega_{\mathrm{T}}$	boundary of surface force
θ	angular degree from straight crack		

Chapter 1 Introduction

1.1 Background

1.1.1 General stainless steels

Stainless steels are iron (Fe) based alloys that include more than 11 % chromium (Cr). It has been widely used in a variety of engineering fields as a promising material for good corrosion resistivity, formability, machinability and weldability [1]. Representative types have been defined as austenitic, ferritic, martensitic and dual-phase stainless steels (duplex: austenitic and ferritic mixtures) based on their chemical compositions and phase structures. A series of mostly used types graded by international standards such as Japanese Industrial Standards (JIS), GuoBiao standards (GB), Korean Standards (KS) and American Iron and Steel Institute standards (AISI), and their main chemical compositions are listed in Table 1.1. Five main elements such as Fe, carbon (C), Cr, nickel (Ni) and molybdenum (Mo) have been purposely mixed for metallurgical manufacturing.

Table 1.1 Category of stainless steels by grades and main chemical compositions.

Category	Grade	Main chemical composition (%, balanced Fe)			
		C	Cr	Ni	Mo
Austenitic	304	≤0.08	18.0~20.0	8.0~10.5	-
	316	≤0.08	16.0~18.0	10.0~14.0	2.0~3.0
Martensitic	410	≤0.15	11.5~13.5	≤0.6	-
	420	0.16~0.25	12.0~14.0	≤0.6	-
Ferritic	405	≤0.08	11.5~14.5	-	-
	430	≤0.12	16.0~18.0	-	-
Duplex	329	≤0.08	23.0~28.0	2.5~5.0	1.0~2.0

In industrial applications, austenitic stainless steels have been broadly employed for mechanical components since they contain a large amount of Ni which promotes stabilizing austenitic grains leading to significantly good ductility. It can lead to an increase in the formability required for metal forming. Martensitic stainless steels promote the aspects of material strength by increasing the amount of C content, which is designed to allow heat treatments such as quenching and tempering for strengthening material. Although ferritic stainless steels do not contain an amount of Ni, they are less costly and have comparable corrosion resistance because it still contains the amount of Cr. Duplex stainless steels are a kind of the most recently developed stainless steel and contain a large amount of Cr, which exhibits excellent resistance of stress corrosion cracking and also shows significant material strength owing to dual-phases in grain structure. As such, various stainless steels have been chosen for industrial applications by engineers depending on their properties.

Figure 1.1 shows a pie chart (unit: %) explaining proportionately the usage of stainless steel in various application fields [2]. Main industrial applications are considered for chemical vessel/piping components, power engineering fields, building construction fields, products for the food industry and automobile industries. Their anti-corrosion performance with a moderate strength has been advantageously highlighted owing to the formation of the self-produced surface passive film. This film prevents material oxidation when the mechanical components experience a corrosive environment. In brief, two main considerations of the material for industrial purposes are corrosion resistance and material strength. Main elements such as Cr and Ni, as well as additional elements such as Mo, nitrogen (N), titanium (Ti) and copper (Cu), play an important role in material properties and could be purposely modified for better material and mechanical properties.

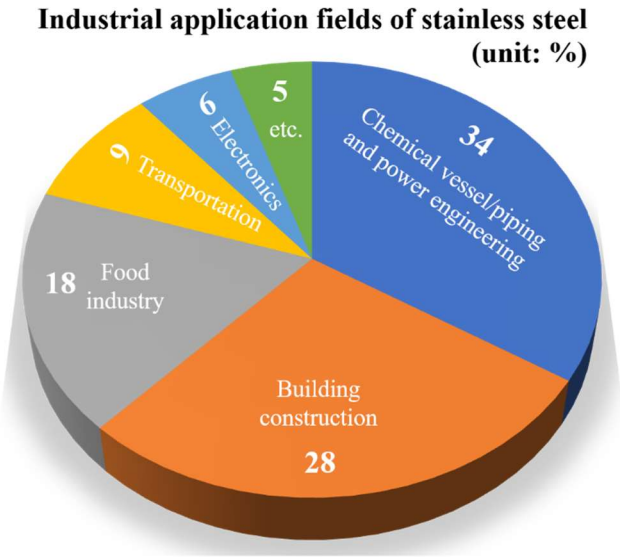

Fig. 1.1 General information of stainless steel. The relative percentage of the main application fields [2].

1.1.2 Type 316 austenitic stainless steel and its problem

In the four types of stainless steel listed in Table 1.1, austenitic stainless steel has been classified as one of the frequently used stainless products. The material, which is also called type 300 series stainless steel, contains large amounts of key elements such as Cr and Ni. From the fundamental point of view, austenitized microstructures formed by adding the amount of Ni benefit to good ductility instead of losing their material strength. On the other hand, its limited material strength gives sometimes a disadvantage in the use of the material. Further, strengthening by heat treatment is rarely achieved due to the low C content, as well as strengthening by surface modification such as shot peening results in uni-directional microstructure near its treated surface. Thus, the aspects of material strength under stable microstructure are always an interesting issue for the material.

Type 304 austenitic stainless steel (18Cr-8Ni) as a basic type has a microstructural harmful issue such as pitting and has been required to modify appropriately. Pitting can occur when the material experiences an aggressive corrosion environment, and the self-produced surface passive film for surface prevention is partly delaminated. The delaminated pitting location can significantly expose corrosion. The pitting problem has been solved through the thermodynamic process during metallurgical fabrication [3]. Adding Mo (2~3 %) contributes to enhancing the resistance against pitting. The role of Mo was found that the formation of a surface passive film with a more highly developed interfacial barrier film composed of Cr_2O_3 plays an important role in solving the pitting problem [4]. The material modified by this process reducing the pitting has been called type 316 austenitic stainless steel. It has been widely used for various steel structures owing to its excellent cost-performance ratio and advanced corrosion resistance [5].

However, type 316 austenitic stainless steel has also metallurgical and mechanical issues such as metal-rich carbide and material strength even though the pitting problem has been solved. Especially, sensitization in austenitic stainless steels has been known to cause intergranular stress corrosion cracking due to Cr-rich precipitations ($Cr_{23}C_6$). Such precipitation easily forms in the surrounding of grain boundaries (GBs) and twin boundaries (TBs) when the material experiences a thermal process between 450 and 900°C or it passes slowly under this temperature range [6-11]. It can lead to Cr depletion near $Cr_{23}C_6$ in a corrosive environment. In general, when the level of Cr in the depletion zone falls below 12-13 wt %, it can become weak and has an adverse effect on the strength and fracture toughness of the material [7,8].

To reduce the sensitization, it has been developed a modified version of type 316, which is called type 316L. Where L denotes a low quantity of C. In this steel, reducing the C

element leads to the decreased risk of formation of $Cr_{23}C_6$, however, it significantly loses its material strength. To recover its material strength, type 316LN was purposely developed. Where N denotes that it contains nitrogen. Although it seems to compensate the loss of yield and ultimate strength compared with the type 316L, strain at fracture has not been preserved [11,12]. Even, type 316LN gives better strength but it sometimes loses the strain at fracture at room temperature [13].

Further, in the case of type 321 fabricated by adding Ti, TiC carbides which are precipitated proportionally at grains and GBs instead of $Cr_{23}C_6$, it contributes to preventing intergranular stress corrosion. Uniform dispersion of TiC in grains and GBs plays a decisive role to improve tensile and fatigue, creep strength [14,15]. Nevertheless, all modification approaches are metallurgical methods, and improving the listed disadvantages could make fabrication costs too high. In addition, the presented methods cannot easily be applicable after mechanical usage of the material. It must be thought of in terms of re-fabrication after usage. Therefore, technical issues such as material strengthening and the reduction of $Cr_{23}C_6$ have been highlighted to be scientifically solved. A proposing modification method has been required, and mechanisms how to improve material disadvantages should be understood.

1.2 Strength of materials and fracture mechanics

1.2.1 Tensile fracture

Fracture mechanics has first introduced approximately a hundred years ago. Griffith and Irwin are the pioneers of theoretical and experimental fracture mechanics that no one can deny until now. Griffith proposed an energetic balance between external force F and actual crack length a to explain the criterion to cracking from a pre-existing defect in

quasi-brittle material [16]. Irwin made historical progress in fracture mechanics by introducing the energy release rate and stress intensity factor (SIF) [17]. This leads to significant development in the field of strength of materials in terms of linear elastic fracture mechanics (LEFM). The main assumption of LEFM is that the deformable material has a cracking driving force under small-scale yielding (SSY) which is proposed by Rice [18]. Figure 1.2 shows the schematics of the cracking material with a plastic regime. Where the distance from crack tip r and an angular degree from straight crack θ are the locational components in polar coordinates, and X and Y are cartesian coordinates from the crack tip. A typical regime of plastic zone based on the uniaxial tensile state is displayed in Fig. 1.2 (a). In Fig. 1.2 (b), the yield stress σ_y and the length of the plastic yielding zone r_y along with X are determined by the degree of material ductility. If the ductility is high, σ_y decreases and r_y increases.

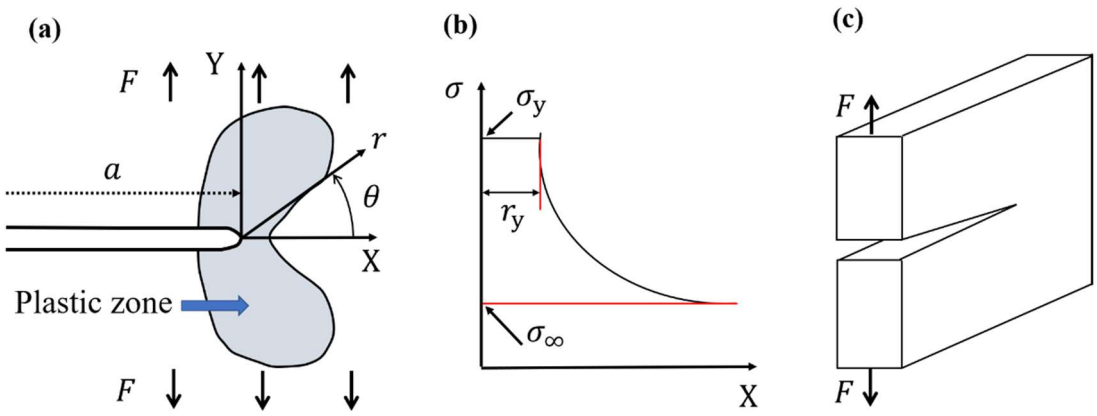

Fig. 1.2 Schematic of the crack tip and corresponding plastic zone under uniaxial tensile state, (a) plastic zone based on coordinates at crack tip singularity, (b) yield stress and length of the plastic yielding zone and (c) illustration of the mode I fracture.

A remote tensile stress σ_∞ is defined as a stress state of sufficiently far location from the crack tip. The mode I fracture illustrated in Fig. 1.2 (c) can be expected under uniaxial tensile or fatigue loading. This type of fracture mode can devise a straight crack propagation pattern in a direction perpendicular to the F.

To identify quantitatively the cracking criterion for elastic-plastic fracture, a classical approach, so-called SSY approximation [18,19], can be used when $r_\mathrm{y} \to 0$,

$$\sigma_\mathrm{ij} = \frac{K}{(2\pi r)^{\frac{1}{2}}} f_\mathrm{ij}(\theta) \ , \tag{1.1}$$

where K is the SIF in the mode I fracture and the function $f_\mathrm{ij}(\theta)$ varies depending on θ and the corresponding triaxial state stress σ_ij. To define correctly the value of a as fracture criterion of elastic-plastic materials, a plasticity correction form by effective crack length a^* has been considered [20]. It can be written as follows,

$$a^* = a + r_\mathrm{y} \ , \tag{1.2}$$

considering the common values for r_y, the a^* can be re-written in terms of K and σ_y [20],

$$a^* = a + \lambda \left(\frac{K}{\sigma_\mathrm{y}}\right)^2 \ , \tag{1.3}$$

where the λ can be defined as the following three options by geometrical assumptions,

$$\lambda = \frac{1}{2\pi} \ , \qquad \text{for plane stress} \tag{1.4.1}$$

$$\lambda = \frac{1}{6\pi}, \qquad \text{for plane strain} \qquad (1.4.2)$$

$$\lambda = \frac{\pi}{16}, \qquad \text{for Dugdale model} \qquad (1.4.3)$$

then it calculates the elastic-plastic fracture criterion. If we assume the limitation as $r_y \ll a$, the relationship between the applied stress σ_a and a^* can give $K = \alpha\sigma_a\sqrt{\pi\, a^*}$. Where α is a geometrical constant depending on a width w. It is generally applied as 1 for inside crack and 1.12 for surface crack. From Eq. (1.3), it can be re-expressed as follows,

$$K = \sqrt{\frac{\pi a {\sigma_a}^2}{1/\alpha - \pi\lambda\left(\sigma_a/\sigma_y\right)^2}}, \qquad (1.5)$$

the critical applied stress σ_{ac} can finally be calculated based on the plasticity-corrected critical crack length a_c^* with the critical expression in terms of fracture toughness $K_c = \alpha\sigma_{ac}\sqrt{\pi\, a_c^*}$ as follows,

$$\sigma_{ac} = \frac{K_c}{\alpha\sqrt{\pi(a_c + r_y)}}, \qquad (1.6)$$

where a_c is the critical crack length. Equations (1.5 and 1.6) can be used to evaluate the σ_{ac} and elastic-plastic fracture based on tensile cracking of the material in this thesis.

1.2.2 Fatigue fracture

In terms of fatigue failure, Paris extended the theory of LEFM to the fatigue analysis in the middle of the 20th century [21]. Plenty of experimental validity was proposed to explain the fatigue crack growth (FCG) law. It describes that the FCG rate da/dN can

be related with SIF range ΔK, i.e., $da/dN = f(\sigma_a, a, \alpha) = f(\Delta K)$. Where α and a are the same symbolic expressions with α and a in tensile fracture but it is the crack length subjected by fatigue loading. N is the number of fatigue cycles. Based on the relationship between da/dN and ΔK, the following Eq. (1.7) has been widely used to assess the FCG behavior,

$$\frac{da}{dN} = A(\Delta K)^B \ , \tag{1.7}$$

where A and B are the intersection and the slope in the data plot of the log-log scale, respectively. In general, SIF can be used when SSY at the crack tip is satisfied. Because the ΔK requiring fatigue cracking is generally low, the plastic zone size in Fig. 1.2 (a) under fatigue loading is small enough for most metallic materials. In general, the FCG tests under a stress-controlled fatigue test have been permitted to evaluate crack propagation behavior in the high-cycle fatigue (HCF) regime. However, an evaluation way for low-cycle fatigue (LCF) analysis has been required because LCF tests need to perform under a strain-controlled test. Thus, the strain intensity factor K_ε has been suggested as a replacement for the SIF approach [22,23]. It assumes that the plastic strain component under a higher level of strain amplitude ε_a in the LCF regime is more dominant than elastic strain component in the HCF regime ($\geq \sim 10^5$ cycles). Thus, the strain intensity factor range ΔK_ε can be defined as the following Eq. (1.8) [22,23],

$$\Delta K_\varepsilon = f_c \Delta\varepsilon \sqrt{\pi a} \ , \tag{1.8}$$

where f_c is a constant that is set to 1 in this study. $\Delta\varepsilon$ is the total strain range. The unit of

ΔK_ε is mm$^{1/2}$. This equation with da/dN has been used to evaluate the FCG behavior in LCF analysis.

To assess the fatigue life, the theoretical approaches for HCF and LCF should be different. The Basquin-Manson-Coffin (BMC) model is one of the widely used equations to evaluate fatigue properties in the LCF and HCF regimes and to determine the required material constants at the strain ratio of $R = -1$, where R is the stress or strain ratio, $R = \sigma_{\min}/\sigma_{\max} = \varepsilon_{\min}/\varepsilon_{\max}$, and here $\sigma_{\max}$ and $\varepsilon_{\max}$, and $\sigma_{\min}$ and $\varepsilon_{\min}$ are the maximum and minimum components for stress and strain, respectively. The expression of the number of reversals to failure $2N_{\mathrm{f}}$ is practically common because one fatigue cycle has two affected reversals in LCF loading by high deformation. To evaluate the relationship between the ε_a and the $2N_{\mathrm{f}}$, the following Eq. (1.9) can be used [24],

$$\frac{\Delta\varepsilon}{2} = \varepsilon_a = \varepsilon_a^{\mathrm{e}} + \varepsilon_a^{\mathrm{p}} = \frac{\sigma_{\mathrm{f}}'}{E}(2N_{\mathrm{f}})^{\mathrm{b}} + \varepsilon_{\mathrm{f}}'\,(2N_{\mathrm{f}})^{\mathrm{c}}\,, \tag{1.9}$$

where E is the elastic modulus, ε_a denotes the half of $\Delta\varepsilon$, which is composed of $\varepsilon_a^{\mathrm{e}}$ as the elastic ε_a in the Basquin model and $\varepsilon_a^{\mathrm{p}}$ as the plastic ε_a in the Manson-Coffin model, respectively. Further, b and c are the exponential constants, and σ_{f}' and $\varepsilon_{\mathrm{f}}'$ are the fatigue strength and ductility coefficients, respectively.

1.3 Effect of electric current in metals

The application of electric current in conductive materials such as metals including stainless steels can simultaneously induce the electron wind force (EWF) [25] and Joule heating. Based on these two phenomenological definitions, a microstructural change can be possible owing to the motion of metal atoms by momentum transfer from electron flow.

When a metallic material experiences the effect of electric current, an increase in a temperature T (℃) induced by the Joule heating is generated. In other words, the effects of the EWF and the Joule heating are accompanied simultaneously and irreversibly. In this way, various reports have been introduced so far. Rapid microstructural modification due to highly raised temperature by Joule heating with the existence of EWF has been only regarded as one of potentiality as the effect of pulsed electric current. For example, cold-rolled magnesium alloy exhibits high-efficiency recrystallization compared with its traditional heat treatment method [26]. An aluminum alloy shows an increase in strain at fracture and decreases in material strength owing to the dissolution of precipitations under lower temperature rising compared with its traditional heat treatment [27]. Ti alloy presents that electric current induced recrystallization with a different type of microstructure could be distinguishable compared with conventional heat treatment temperature. The effect of pulsed electric current on NiTi alloy contributes to changing grain size [28]. On the other hand, the problem of existing conclusions was only a consequential prediction that the current application method was thought to go through the recrystallization process such as atomic diffusion, nucleation, recrystallization leading to grain growth, not a comprehensive process confirmation. Even though the EWF acts as an influential factor and can annihilate dislocations, it only concluded that it is different compared with existing heat treatments. There has been an argument what is the role of EWF. The effect of EWF must be clarified through experimental verifications. Further, it has been strongly required to establish and propose a reliable mechanism to clarify the role of EWF. If there is a comprehensive mechanism than the current argument, the effect of HDPEC has to shift to a new paradigm in terms of EWF.

Since EWF can change essentially dislocation structures, the EWF can be expressed as

the following equation [29],

$$F_{\mathrm{EW}} = \frac{\rho_{\mathrm{d}}}{N_{\mathrm{d}}} n_{\mathrm{e}} e j \ , \tag{1.10}$$

where F_{EW} is the EWF, ρ_{d} is the specific resistivity due to dislocation, N_{d} is the dislocation density, n_{e} is the electron density, e is the electron charge and j is the density of electric current, respectively. Based on this concept, there have been several reports that the EWF could modify microstructures such as dislocation network, grain size and phase structure in a wide variety of materials [29-31].

Further, the application of electric current in a material necessarily accompanies a temperature rising ΔT_{J} (℃) by the Joule heating. Here, ΔT_{J} can be predicted using the following Joule heating equation [30],

$$\Delta T_{\mathrm{J}} = T_{\mathrm{R}} - T_{\mathrm{r}} = \frac{\rho j^2 t_{\mathrm{d}}}{C_{\mathrm{p}}\, d_{\mathrm{m}}} \ , \tag{1.11}$$

where ρ is the electrical resistivity, t_{d} is the duration time of current, C_{p} is the specific heat capacity, and d_{m} the density of a material, respectively. A raised temperature T_{R} (℃) can be determined by the summation of ΔT_{J} and the room temperature T_{r} (℃).

1.4 Research objectives

In the aspects of material strength, the material is often limited by its relatively low strength, and methods strengthened by heat treatment are costly as well as rarely achieved due to the low C content. Therefore, there were several attempts to overcome the strength

limitations through chemical and mechanical processes. For example, nitrogen-containing in the metallurgical process gives an improved material strength [32], and surface nanocrystallization by shot peening could contribute to strengthening 316L owing to surface grain refinement and compressive residual stress [33,34]. Nevertheless, most methods lead to losing the ductility of the material with increased strength. The strength-ductility trade-off has been thought nature limitation of materials. To break this rule is one of a standing scientific interest in material science [35]. In the aspects of $Cr_{23}C_6$, the reduction of $Cr_{23}C_6$ is also the main requirement to prevent sensitization. Metallurgical processes and thermodynamic dissolution are costly and do not respond to requests for modification during the use of mechanical parts. Thus, post-treatment has been limited.

Figure 1.3 shows the schematics of general requirements for type 316 stainless steel and conventional methods to overcome the disadvantages of the material based on the literature survey presented in sub-chapter 1.1.2.

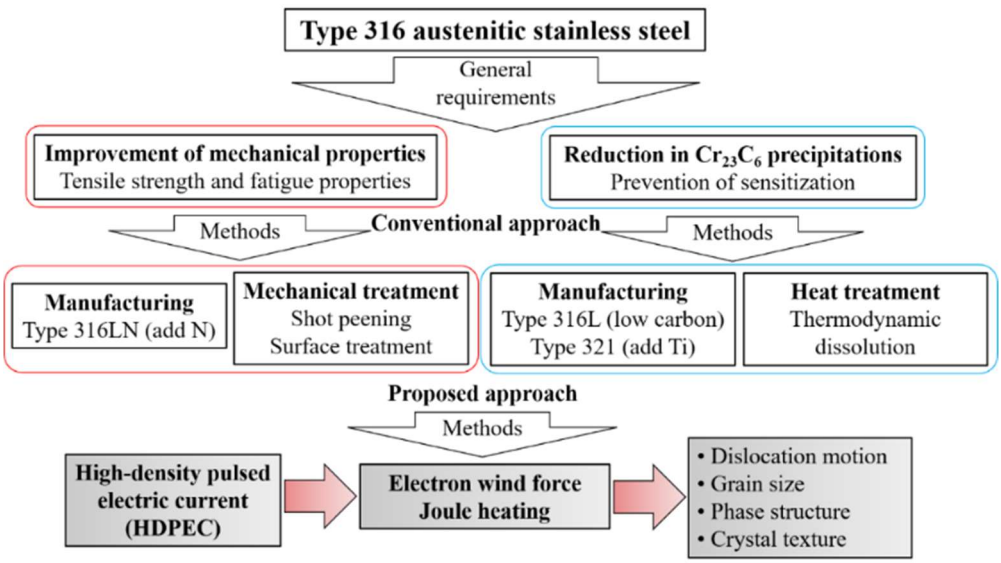

Fig. 1.3 Schematics of general requirements for type 316 stainless steel, a series of conventional methods and proposal of HDPEC.

Recent reports emphasize that the fatigue and fracture properties of metallic materials could be improved by the application of high-density pulsed electric current (HDPEC) [36-43]. It leads to the delay of FCG based on the crack healing phenomenon and microstructural modification such as the annihilation of dislocations. The investigated method has been interestingly regarded as one of the modification ways to improve mechanical properties. Based on methodological simplicity and cost-performance, the HDPEC method become a promising way in the maintenance of mechanical components in industrial sites. Especially, the main advantages are less requirement of time-consuming and less effort to disassemble components of a running mechanical system.

In this thesis, it has been elaborated to prove the potentiality of the HDPEC application based on its effects. It is stated whether the effect of HDPEC can solve the previously described disadvantageous issues such as the material strength and the reduction of $Cr_{23}C_6$. A series of tensile and fatigue tests are conducted to demonstrate the improvement of mechanical properties as the effect of HDPEC. Characterizing understandable microstructural evidence is an important work to define describable mechanisms. Mechanisms associated with improved mechanical properties and desirable microstructures will be proposed in this thesis. The effect of EWF and Joule heating will be discussed under an assumption of temperature-controlled and enhanced EWF. Further, this thesis aims also to report for the enhancement of material strength without loss of strain at fracture based on dislocation motion, change of grain size, crystal texture and phase structure, as well as the reduction of $Cr_{23}C_6$. Finding new phenomena to describe strengthening the material and the dissolution of $Cr_{23}C_6$ by the effect of HDPEC is main interesting. It is emphasized that the effect of HDPEC is a post-treatment way without metallurgical processes and thermodynamic dissolution.

1.5 Thesis organization

In Fig. 1.4, the flowchart of the working procedure for this thesis is introduced to demonstrate the effect of HDPEC in the material. The main hypothesis is the modification of mechanical properties and microstructure under the controlled ΔT_{J}. In chapter 1, unsolved problems in the range of improvement of mechanical properties and conditions of HDPEC are classified based on literature surveys. Although fatigue damage recovery in the range of HCF has been extensively demonstrated [36-43], some cases such as tensile fracture and LCF regime remain unclear and it should be clarified with HDPEC conditions such as j, t_{d} and the number of pulses p. In chapter 2, experimental, theoretical and simulation approaches are explained to demonstrate tensile and fatigue tests. Geometrical aspects such as the presence or absence of notches and cracks were also examined. From chapters 3 to 6, stress/strain relations and fatigue properties are the main issues to determine the effect of HDPEC. Accordance with theory and simulation based on experimental results will be shown as a series of outputs. If proper agreements come, achievements in the improvements of tensile and fatigue properties will be explained microstructural features. A series of assessments and evaluations will be performed with the explanation of matching between material properties and microstructure. The efficiency of HDPEC methods will be discussed based on results in fatigue analysis and fatigue crack healing. Finally, in chapter 7, this thesis proposes that the effect of HDPEC can give several advantages in the modification of mechanical and material properties, thereby proposing microstructural mechanisms. A step-by-step explanation to overcome the disadvantages of the material will be presented.

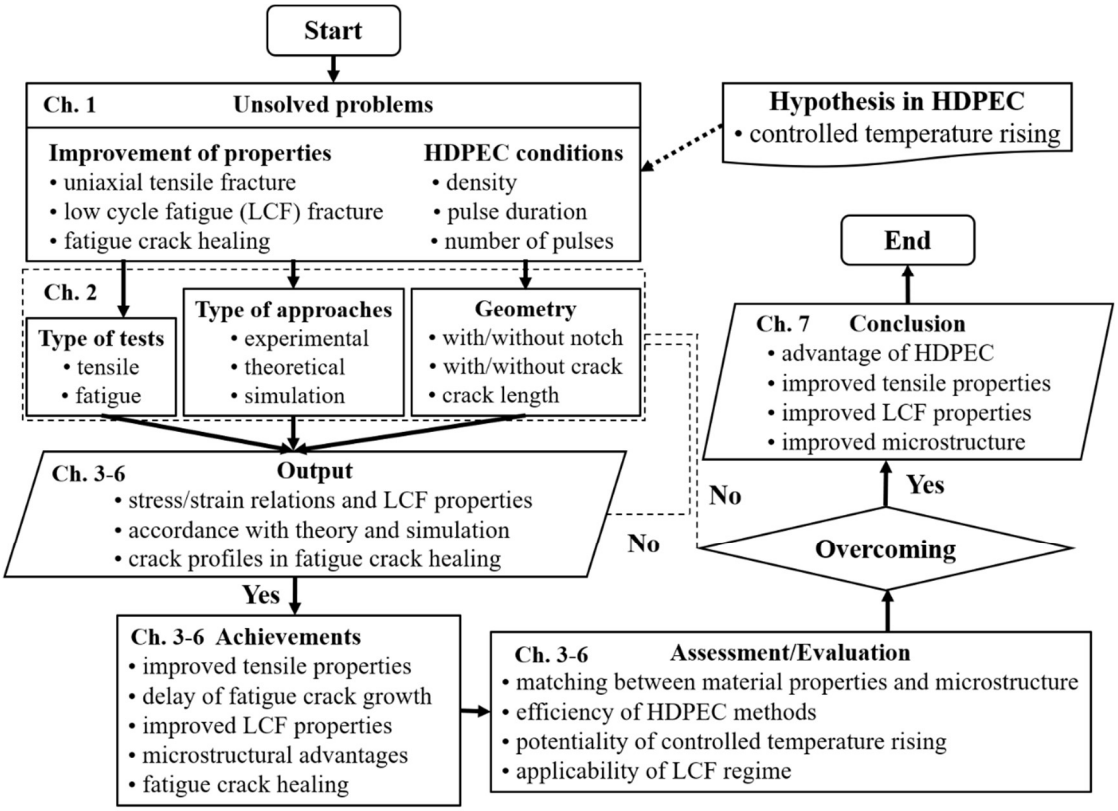

Fig. 1.4 Schematic diagram of the working procedure for the organization of the thesis.

Reference

[1] N.R. Baddoo, Stainless steel in construction: A review of research, applications, challenges and opportunities, Journal of Constructional Steel Research. 64 (2008) 1199–1206. https://doi.org/10.1016/j.jcsr.2008.07.011.

[2] ASM international Alloy digest sourcebook, 2000

[3] C.-O.A. Olsson, D. Landolt, Passive films on stainless steels—chemistry, structure and growth, Electrochimica Acta. 48 (2003) 1093–1104. https://doi.org/10.1016/S0013-4686(02)00841-1.

[4] C. R. Clayton, Y. C. Lu, A Bipolar model of the passivity of stainless steel: The Role of Mo Addition, Journal of the Electrochemical Society. 133 (1986) 2465–2473. https://doi.org/10.1149/1.2108451.

[5] W. J. Mills, Fracture toughness of type 304 and 316 stainless steels and their welds, International Materials Reviews. 42 (1997) 45–82. https://doi.org/10.1179/imr.1997.42.2.45.

[6] R. Jones, V. Randle, Sensitisation behaviour of grain boundary engineered austenitic stainless steel, Materials Science and Engineering: A. 527 (2010) 4275–4280. https://doi.org/10.1016/j.msea.2010.03.058.

[7] K. Han, Y. Xin, R. Walsh, S. Downey, P. N. Kalu, The effects of grain boundary precipitates on cryogenic properties of aged 316-type stainless steels, Materials Science and Engineering: A. 516 (2009) 169–179. https://doi.org/10.1016/j.msea.2009.03.009.

[8] R.L. Tobler, A. Nishimura, J. Yamamoto, Design-relevant mechanical properties of 316-type steels for superconducting magnets, Cryogenics. 37 (1997) 533–550. https://doi.org/10.1016/S0011-2275(97)00071-4.

[9] D. Wasnik, Precipitation stages in a 316L austenitic stainless steel, Scripta Materialia. 49 (2003) 135–141. https://doi.org/10.1016/S1359-6462(03)00220-3.

[10] K. Kaneko, T. Fukunaga, K. Yamada, N. Nakada, M. Kikuchi, Z. Saghi, J. S. Barnard, P. A. Midgley, Formation of $M_{23}C_6$-type precipitates and chromium-depleted zones in austenite stainless steel, Scripta Materialia. 65 (2011) 509–512. https://doi.org/10.1016/j.scriptamat.2011.06.010.

[11] J. B. Vogt, J. Foct, C. Regnard, G. Robert, J. Dhers, Low-temperature fatigue of 316L and 316LN austenitic stainless steels, Metallurgical Transactions A. 22 (1991) 2385–2392. https://doi.org/10.1007/BF02665004.

[12] V. Ganesan, M. D. Mathew, K. B. Sankara Rao, Influence of nitrogen on tensile properties of 316LN SS, Materials Science and Technology. 25 (2009) 614–618. https://doi.org/10.1179/174328408X317066.

[13] K. Ishio, H. Nakajima, Effects of nitrogen on the mechanical properties of 316LN stainless steel, Tetsu-to-Hagane. 92 (2006) 90-96.

[14] K. Min, S. Lee, S. Nam, Effects of TiC and $Cr_{23}C_6$ carbides on creep-fatigue properties in AISI 321 stainless steel, Materials Transactions. 43 (2002) 2808–2812. https://doi.org/10.2320/matertrans.43.2808.

[15] A. S. Grot, J. E. Spruiell, Microstructural stability of titanium-modified type 316 and type 321 stainless steel, Metallurgical Transactions A. 6 (1975) 2023–2030. https://doi.org/10.1007/BF03161827.

[16] A. A. Griffith, The phenomena of rupture and flow in solids, Philosophical Transactions of the Royal Society A. 221 (1921) 163–198. https://doi.org/10.1098/rsta.1921.0006.

[17] G. R. Irwin, Fracture Dynamics, Fracturing of Metals. (1948) 147–166.

[18] J. R. Rice, A path independent integral and the approximate analysis of strain concentration by notches and cracks, Journal of Applied Mechanics. 35 (1968) 379–386. https://doi.org/10.1115/1.3601206.

[19] J. R. Rice, Limitations to the small-scale yielding approximation for crack tip plasticity, Journal of the Mechanics and Physics of Solids. 22 (1974) 17–26. https://doi.org/10.1016/0022-5096(74)90010-6.

[20] D. E. Hauf, D. M. Parks, H. Lee, A modified effective crack-length formulation in elastic-plastic fracture mechanics, Mechanics of Materials. 20 (1995) 273–289. https://doi.org/10.1016/0167-6636(94)00058-1.

[21] P. Paris, F. Erdogan, A critical analysis of crack propagation laws, Journal of Basic Engineering. 85 (1963) 528–533. https://doi.org/10.1115/1.3656900.

[22] M. Kamaya, M. Kawakubo, Strain-based modeling of fatigue crack growth–an

experimental approach for stainless steel, International Journal of Fatigue. 44 (2012) 131–140. http://dx.doi.org/10.1016/j.ijfatigue.2012.05.006.

[23] M. Kamaya, Influence of strain range on fatigue life reduction of stainless steel in PWR primary water, Fatigue & Fracture of Engineering Materials & Structures. 40 (2017) 2194–2203. https://doi.org/10.1111/ffe.12650.

[24] R. I. Stephens, A. Fatemi, R. R. Stephens and H. O. Fuchs: *Metal fatigue in engineering*, (John Wiley & Sons, New York, 2000).

[25] M. Saka, K. Sasagawa, M. Muraoka, H. Tohmyoh, Y. Ju, Metallic micro and nano materials, Engineering Materials, Springer-Verlag Berlin, Heidelberg, (2011) 15–18. https://doi.org/10.1007/978-3-642-15411-9_2.

[26] Y. Jiang, G. Tang, C. Shek, W. Liu, Microstructure and texture evolution of the cold-rolled AZ91 magnesium alloy strip under electropulsing treatment, Journal of Alloys and Compounds. 509 (2011) 4308–4313. https://doi.org/10.1016/j.jallcom.2011.01.052.

[27] W. Wu, Y. Wang, J. Wang, S. Wei, Effect of electrical pulse on the precipitates and material strength of 2024 aluminum alloy, Materials Science and Engineering A. 608 (2014) 190–198. https://doi.org/10.1016/j.msea.2014.04.071.

[28] R. Zhu, J. Liu, G. Tang, S. Shi, M. Fu, Z. Tse, The improved superelasticity of NiTi alloy via electropulsing treatment for minutes, Journal of Alloys and Compounds. 584 (2014) 225–231. https://doi.org/10.1016/j.jallcom.2013.09.040.

[29] H. Conrad, Electroplasticity in metals and ceramics, Materials Science and Engineering A. 287 (2000) 276–287. https://doi.org/10.1016/S0921-5093(00)00786-3.

[30] D. Waryoba, Z. Islam, B. Wang, A. Haque, Recrystallization mechanisms of Zircaloy-4 alloy annealed by electric current, Journal of Alloys and Compounds. 820 (2020) 153409. https://doi.org/10.1016/j.jallcom.2019.153409.

[31] Z. Islam, H. Gao, A. Haque, Synergy of elastic strain energy and electron wind force on thin film grain growth at room temperature, Materials Characterization. 152 (2019) 85–93. https://doi.org/10.1016/j.matchar.2019.04.008.

[32] T. H. Lee, C. S. Oh, S. J. Kim, Effects of nitrogen on deformation-induced martensitic transformation in metastable austenitic Fe–18Cr–10Mn–N steels, Scripta Materialia. 58 (2008) 110–113. https://doi.org/10.1016/j.scriptamat.2007.09.029.

[33] G. Liu, J. Lu, K. Lu, Surface nanocrystallization of 316L stainless steel induced by ultrasonic shot peening, Materials Science and Engineering: A. 286 (2000) 91–95. https://doi.org/10.1016/S0921-5093(00)00686-9.

[34] S. Bagherifard, S. Slawik, I. Fernández-Pariente, C. Pauly, F. Mücklich, M. Guagliano, Nanoscale surface modification of AISI 316L stainless steel by severe shot peening, Materials & Design. 102 (2016) 68–77. https://doi.org/10.1016/j.matdes.2016.03.162.

[35] Y. Wei, Y. Li, L. Zhu, Y. Liu, X. Lei, G. Wang, Y. Wu, Z. Mi, J. Liu, H. Wang, H. Gao, Evading the strength–ductility trade-off dilemma in steel through gradient hierarchical nanotwins, Nature Communication. 5 (2014) 3580. https://doi.org/10.1038/ncomms4580.

[36] A. Hosoi, T. Nagahama, Y. Ju, Fatigue crack healing by a controlled high density electric current field, Materials Science and Engineering: A. 533 (2012) 38–42. https://doi.org/10.1016/j.msea.2011.11.024.

[37] A. Hosoi, T. Kishi, Y. Ju, Healing of fatigue crack by high-density electropulsing in austenitic stainless steel treated with the surface-activated pre-coating, Materials. 6 (2013) 4213–4225. https://doi.org/10.3390/ma6094213.

[38] A. Hosoi, T. Yano, Y. Morita, Y. Ju, Quantitative evaluation of the displacement

distribution and stress intensity factor of fatigue cracks healed by a controlled high-density electric current field, Fatigue & Fracture of Engineering Materials & Structures. 37 (2014) 1025–1033. https://doi.org/10.1111/ffe.12175.

[39] Y. Tang, A. Hosoi, Y. Iwase, Y. Ju, Effect of high-density electric current on the microstructure and fatigue crack initiation of stainless steel, Materials Transactions. 54 (2013) 2085–2092. https://doi.org/10.2320/matertrans.M2013198.

[40] Y. Tang, A. Hosoi, Y. Morita, Y. Ju, Restoration of fatigue damage in stainless steel by high-density electric current, International Journal of Fatigue. 56 (2013) 69–74. http://dx.doi.org/10.1016/j.ijfatigue.2013.08.012.

[41] J. Jung, Y. Ju, Y. Morita, Y. Toku, Effect of pulsed electric current on the growth behavior of fatigue crack in Al alloy, Procedia Structural Integrity. 2 (2016) 2989–2993. https://doi.org/10.1016/j.prostr.2016.06.374.

[42] J. Jung, Y. Ju, Y. Morita, Y. Toku, Enhancement of fatigue life of aluminum alloy affected by the density of pulsed electric current, International Journal of Fatigue. 103 (2017) 419–425. https://doi.org/10.1016/j.ijfatigue.2017.06.021.

[43] J. Jung, Y. Ju, Y. Morita, Y. Toku, Y. Uematsu, Delaying effect of high-density electric current on fatigue crack growth in A6061-T6 Aluminum Alloy, Materials Transactions. 57 (2016) 2104–2109. https://doi.org/10.2320/matertrans.M2016240.

Chapter 2 Experimental approach

2.1 Material and sample preparation

Commercial type 316 stainless steel (SUS316), standardized according to JIS G 4305, has been used for a series of research works presented in this thesis. Table 2.1 lists its chemical composition. All samples for tensile and fatigue tests were cut using electro-discharge machining (EDM) for dumbbell-shaped geometry. After cutting the samples, annealing heat treatment was applied to release the residual stress induced by the EDM process and to generalize the microstructure of samples. The temperature was gradually increased to 900 °C for 4 h, kept for 10 min, and cooled to room temperature in a furnace. After that, the samples were mirror-like polished with emery papers of grades 180–2000. DiaPro-Mol 1 and 3 μm (Struers, Denmark) were purposely used to be able to observe microstructures.

2.2 Investigation of mechanical properties

A series of tensile and fatigue tests were performed using a Shimadzu servo-pulser (EHF-EV051K1, Japan), which generates tensile or fatigue loading through uniaxial tension and sinusoidal cyclic amplitudes at room temperature.

Table 2.1 Chemical composition of type 316 austenitic stainless steel. (wt %)

C	Si	Mn	P	S	Ni	Cr	Mo	Fe
≤0.08	≤1.00	≤2.00	≤0.045	≤0.03	10.0～14.0	16.0～18.0	2.0～3.0	Bal.

2.2.1 Tensile tests

The detailed geometry for the tensile tests is illustrated in Fig. 2.1 (a). The HDPEC was applied to both ends of the sample using copper electrodes. Then, a series of tensile tests was performed to demonstrate the effect of HDPEC on mechanical properties compared with the untreated sample. The tensile speed was controlled by the crosshead speed of the tensile machine and uniquely applied as 0.03 mm/sec. The true tensile stress σ and strain ε were measured using the following approximation under an assumption of uniform deformation, $\sigma = \sigma_e(1 + \varepsilon_e)$ and $\varepsilon = \ln(1 + \varepsilon_e)$. Where σ_e and ε_e are the engineering stress and strain, respectively.

Typical mechanical properties of the untreated sample after the heat treatment are listed in Table 2.2. Based on the presented tensile properties, this thesis seeks specified conditions of HDPEC to improve the mechanical properties. In Fig. 2.1 (b), the geometry of a single-center notch was introduced. It is additionally processed at one edge of the center in the geometry of Fig. 2.1 (a) if the notch is purposely required.

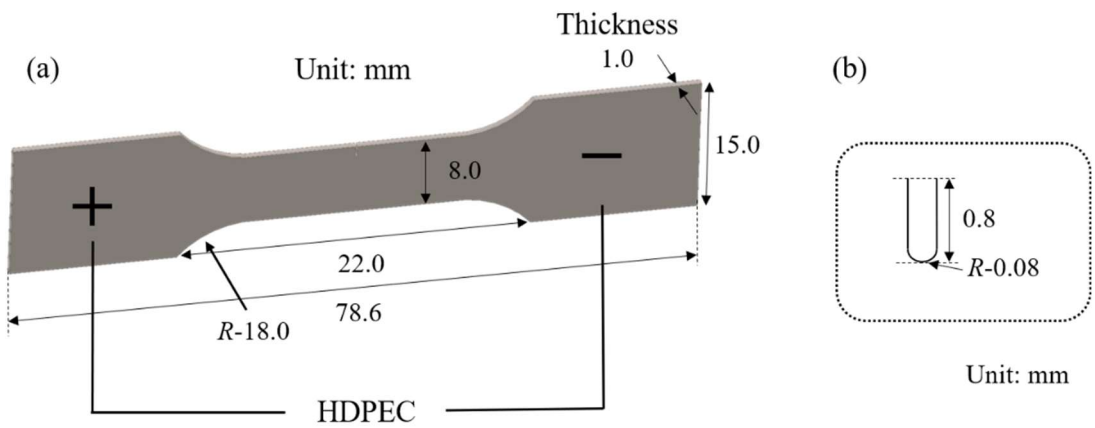

Fig. 2.1 Illustration of the sample for tensile tests and application method of HDPEC, (a) geometry of sample and (b) geometry of notch.

Table 2.2 Mechanical properties of the material from the tensile test.

True yield stress (MPa)	True ultimate stress (MPa)	True strain at fracture	Elastic modulus (GPa)	Poisson's ratio
363±13	698±30	0.477±0.008	195	0.295

2.2.2 Fatigue tests

Figure 2.2 (a-c) shows schematics of the fatigue tests, the notch geometry and the sample geometry with applying method of HDPEC. A single notch with a length of 2 mm and a radius of 0.15 mm was made to induce Mode I FCG. To assess the LCF properties, strain-controlled fatigue tests were applied as the most accessible approach [1]. All fatigue tests were conducted under a frequency of 1 Hz. The strain ratios of $R = -1$ and 0.5 were purposely examined. The definition of fatigue regimes is summarized in Table 2.3 [2].

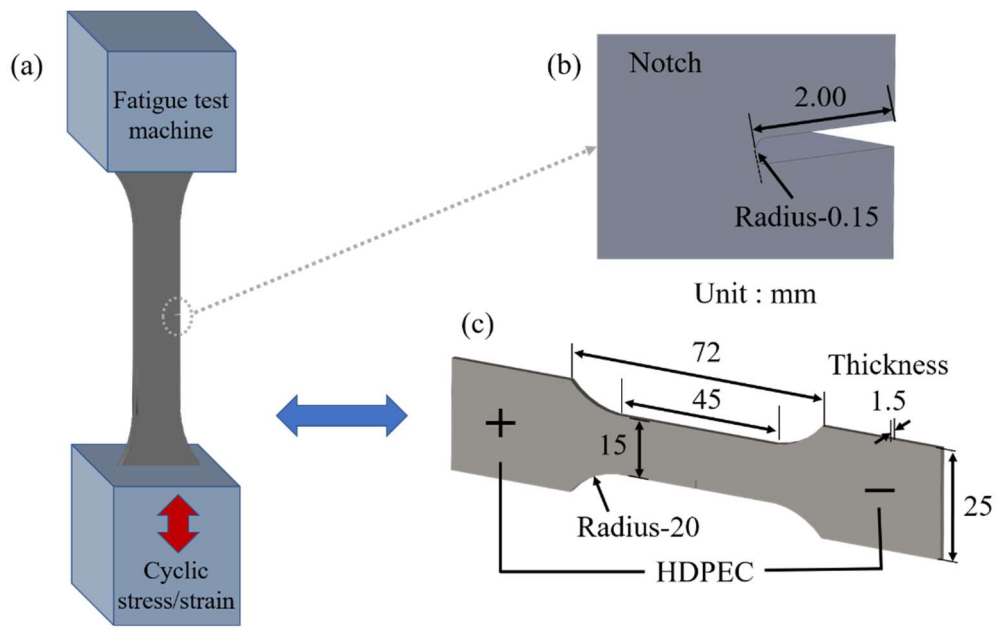

Fig. 2.2 3D schematics associated with the fatigue tests, (a) illustration of the fatigue test machine, (b) that of the notch geometry and (c) that of sample geometry with applying HDPEC method.

Table 2.3 Definition of fatigue regimes and typical types of application methods.

Regimes	Failure cycle	Control method	Dominant deformation type
LCF	$\leq 10^5$	Strain	Elastic and plastic
HCF	10^5 to 10^7	Stress	Elastic
VHCF	$\geq 10^7$	Stress	Elastic

2.3 Application of HDPEC

Tensile and fatigue properties were evaluated based on the conditions of HDPEC. An electric current machine (Miyachi, MDA-8000B, Japan) was used to apply the HDPEC. The main factors of HDPEC Conditions such as j, t_{d} and p were purposely considered to be dealt with in corresponding chapters. The effectiveness of the HDPEC application determined by the main factors is evaluated. The application of HDPEC is always accompanied by ΔT_{J} due to Joule heating. To consider the controlled temperature method assumed in this thesis, the prediction of ΔT_{J} by Eq. (1.11) of chapter 1 and measurement of T_{R} using an infrared thermometer (GTL, OPTEX FA, Japan) were performed. The measurement accuracy is ±0.1°C and the sampling frequency is 1000 Hz. The measurement of T_{R} was performed more than twice to identify exceptional errors due to instantaneously and locally occurring ΔT_{J}.

2.4 Microstructure observation

The field-emission scanning electron microscopy (FESEM, JSM-7200F, JEOL, Japan) was preferentially used to characterize microstructure features in both tensile and fatigue tests.

Table 2.4 Definition of misorientation-angles of GBs.

LAGBs (°)	HAGBs (°)	∑ 3 TBs (°)
3-15	15-63	60±1

For the corresponding crystallographic analysis, the electron backscatter diffraction (EBSD) mappings were performed using the EBSD detector (NordlysNano, Oxford, United Kingdom) equipped with FESEM. EBSD samples were prepared by chemical polishing after mechanical polishing, and then Ar ion milling was conducted on the selected samples requiring a high-quality surface finish. Each EBSD scan was performed with a step size of 1 μm. The post-process of scanned EBSD data was carried out using M-TEX 5.3 software. GB definitions are applied as typical misorientation angles of GBs in stainless steels as listed in Table 2.4. Typical types of GBs such as low angle grain boundaries (LAGBs), high angle grain boundaries (HAGBs) and ∑ 3 TBs are defined. Additionally, ∑ 3^n coincidence site lattice (CSL) boundaries such as ∑ 9 (38.94° around <110>), ∑ 27a (31.59° around <110>) and ∑ 27b (35.43° around <210>), which are usually presented in this material, were also considered [3-5].

For elemental analysis, the energy-dispersive X-ray spectroscopy (EDS, 151MS, JEOL, Japan) was used for the top view of the selected grain. A cross-sectional area (CSA) perpendicular to current flow was examined based on the scanning transmission electron microscopy (STEM) configuration using the transmission electron microscopy (TEM, JEM-2100F, JEOL, Japan) equipped with a high-angle annular dark-field. EDS mappings of CSA were also conducted in the TEM environment.

2.5 Formulation of finite element analysis

In a material domain Ω given by a force f_Ω, a surface force T_s on a boundary $\partial\Omega_T$ and a displacement d on a boundary $\partial\Omega_d$ can be considered. The equilibrium of continuous material can be defined as $div\ \sigma + f_\Omega = 0$ on Ω, $\sigma.n = T$ on $\partial\Omega_T$, and $u = d$ on $\partial\Omega_d$, where σ and u are the stress and displacement fields, respectively. A series of constitutive equations can be expressed based on elastic and plastic strains ($\varepsilon_{ij}^e + \varepsilon_{ij}^p$) as follows,

$$\varepsilon_{ij} = \varepsilon_{ij}^e + \varepsilon_{ij}^p \ , \tag{2.1}$$

$$\sigma_{ij} = E_{ijkl}\varepsilon_{kl}^e = \mathbb{E}: \nabla_s u + \sigma_p \ , \tag{2.2}$$

where $\mathbb{E}$ is the elasticity tensor with the matrix E_{ijkl}, $\nabla_s u$ is the symmetric gradient from u, which is related with the elastic strain ε_{kl}^e, and σ_p is plastic stress. Then, the von Mises yield criterion can be expressed by Eq. (2.3), where σ_1, σ_2, and σ_3 denote respectively the principal stresses of triaxial state,

$$f\left(\sigma_{ij}, \varepsilon_{ij}^p\right) = \sqrt{\frac{1}{2}[(\sigma_1 - \sigma_2)^2 + (\sigma_1 - \sigma_3)^2 + (\sigma_2 - \sigma_3)^2]} - \sigma_y \varepsilon_{ij}^p = 0. \tag{2.3}$$

Thus, finite element discretization in mesh domain Ω^h on Ω can be given by Eq. (2.4),

$$v^h(x) = \sum_i v_i N_i\ (x)\ , \tag{2.4}$$

the displacement field of mesh v^h on Ω^h can be discretized to the displacements v_i by an interpolation function $N_i\ (x)$. Thus, finite element formulation can be given by Eq. (2.5),

$$\int_{\partial\Omega^{\mathrm{h}}} TN\, dS + \int_{\partial\Omega_{\mathrm{d}}^{\mathrm{h}}} TN\, dS + \int_{\Omega^{\mathrm{h}}} fN\, dV - \int_{\Omega^{\mathrm{h}}} \sigma_{\mathrm{p}} \nabla N\, dV = \int_{\Omega^{\mathrm{h}}} \mathbb{E}\, u_{\mathrm{j}} \nabla N_{\mathrm{i}} \nabla N_{\mathrm{j}}\, dV, \quad (2.5)$$

$$K^{\mathrm{e}}.U = F^{\mathrm{S}} + F^{\mathrm{R}} + F^{\mathrm{V}} - B.\sigma_{\mathrm{p}}\ , \quad (2.6)$$

where K^{e} is the elastic stiffness, and U is the displacement in mesh nodes. Equivalent nodal forces are constructed by a surface nodal force F^{S}, volumetric nodal force F^{V}, reaction nodal force F^{R} on the imposed displacement and interior plastic term $B.\sigma_{\mathrm{p}}$.

Reference

[1] R. I. Stephens, A. Fatemi, R. R. Stephens and H. O. Fuchs: *Metal fatigue in engineering*, (John Wiley & Sons, New York, 2000).

[2] S. Murakami: *Continuum damage mechanics: a continuum mechanics approach to the analysis of damage and fracture*, (Springer, Dordrecht, 2012).

[3] D. G. Brandon, The structure of high-angle grain boundaries, Acta Metallurgica. 14 (1966) 1479–1484. https://doi.org/10.1016/0001-6160(66)90168-4.

[4] K. Yvell, T. M. Grehk, P. Hedström, A. Borgenstam, G. Engberg, Microstructure development in a high-nickel austenitic stainless steel using EBSD during in situ tensile deformation, Materials Characterization. 135 (2018) 228–237. https://doi.org/10.1016/j.matchar.2017.11.046.

[5] M. Rout, R. Ranjan, S. K. Pal, S. B. Singh, EBSD study of microstructure evolution during axisymmetric hot compression of 304LN stainless steel, Materials Science and Engineering: A. 711 (2018) 378–388. https://doi.org/10.1016/j.msea.2017.11.059.

Chapter 3 Tensile fracture behavior modified by HDPEC

This chapter elaborates on the evaluation of tensile fracture behavior modified by HDPEC. Based on the fracture criterion like critical fracture strength and fracture toughness, improved fracture thresholds owing to the effect of HDPEC were demonstrated using tensile tests and finite element analysis (FEA). It has been written based on the copyright permission of the following published article: Evaluation of electric current-induced improvement of fracture characteristics in SUS316, Materials Transactions. 62 (2021) 748–755.

3.1 Introduction

The prediction of crack initiation and propagation is important for the reliability of mechanical and material systems since most materials are finally broken starting from a tiny pre-existing crack [1-3]. For assessments of fracture criterion in the material, an analysis of elastic-plastic behavior at the crack tip is important because crack propagation is determined by stress distribution near the crack tip. Although it is not easy to enhance the fracture thresholds of materials, there exist feasible methods that have been broadly used. For instance, crack resistance by the crack tip dulling can slow crack propagation in certain loading conditions [4-6], and improvements of fracture strength and toughness owing to metallurgical reorganization can increase fracture thresholds [7-8].

The application of HDPEC in metals, which is introduced in chapter 1, has become one of the possible methods to improve fracture properties from a few decades ago [9-13]. To optimize conditions of HDPEC for a given material has recently been required to improve the efficiency of HDPEC application. Improved material properties by HDPEC

application depend on the applied conditions such as j, t_{d} and p, which can lead to different fracture characteristics. To estimate the degree of modified qualities, FEA is one of the broadly used methods because it is a low-cost approach to describe a fracture model in a material [14].

In this chapter, the prediction of mechanical responses such as σ_{y} and strain hardening exponent n, which can be modified by the application of HDPEC, is the main interesting issue to understand fracture behavior of the material. Based on the framework of fracture mechanics [15-19], fracture parameters were assessed based on a combination between the fracture theory and the FEA. Modified material properties were obtained by a series of tensile tests under various conditions of HDPEC. The obtained mechanical properties were used to determine modified fracture properties. FEA was used to evaluate modified fracture strength near a crack tip. The evolution of increased fracture criterion by HDPEC was provided. In addition, crack profiles such as the crack opening displacements (CODs) and the crack tip opening displacements (CTODs) were predicted to demonstrate the fracture threshold improved with the application of HDPEC.

3.2 Analysis procedure

The flowchart of investigated analysis for this chapter is shown in Fig. 3.1. Starting with the HDPEC application on samples, a series of tensile tests was performed. The E, σ_{y} and n with a coefficient m were respectively obtained from the tensile tests. Elastic-plastic fracture theories were considered to predict the value of K_{c}. The analytical outputs such as σ_{ac}, r_{y} and a_{c} were used to perform the FEA with the isotropic hardening model. Each FEA calculation was repeatably conducted to quantify a series of data sets.

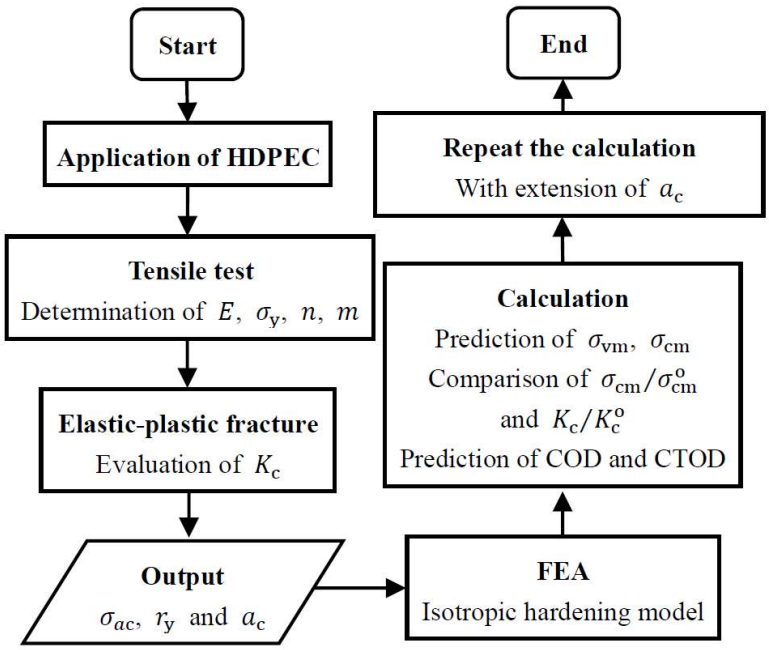

Fig. 3.1 Flowchart of investigated simulation procedure in chapter 3.

The FEA model was investigated to calculate the local stress distribution by von Mises stress σ_{vm} and its critical value σ_{cm} near a crack tip. Increased ratio $\sigma_{cm}/\sigma_{cm}^o$ by HDPEC application was verified based on a comparison with its initial value σ_{cm}^o. Ratio K_c/K_c^o between enhanced K_c and its initial value K_c^o was determined. The CODs and CTODs were supplementally simulated to explain the enhanced fracture thresholds. Evaluation based on the original and the fracture parameters enhanced by the application of HDPEC was demonstrated.

3.2.1 Tensile test

Tensile tests were performed based on samples without the notch to identify tensile properties changed by the application of HDPEC. Different HDPEC conditions were applied to demonstrate the effect of HDPEC. The conditions of HDPEC such as j, t_d and p were listed in Table 3.1.

Table 3.1 Case definitions by the condition of HDPEC in tensile tests.

Cases	**A**	**B**	**C**	**D**	**E**
Density (j), A/mm^2	Untreated	150	150	300	300
Duration time (t_d), ms	-	5	10	5	10
Applied number (p), times	-	2	1	2	1

The untreated sample was denoted by case A. The treated samples were denoted by cases B, C, D and E. Based on the same total applied time ($t_\mathrm{d} \times p = 10$ ms), cases B and D are divided by 2 p with t_d of 5 ms whereas cases C and E are applied by 1 p with t_d of 10 ms.

3.2.2 Finite element analysis

In fracture theories, equation (1.6) in chapter 1 can be used to determine the relationship between σ_{ac} and a given a_c in FEA. Figure 3.2 (a) represents the generated meshes and the investigated half-cut model for FEA. A two-dimensional model under plane stress assumption was considered because the geometry used for the tensile test is a thin plate. At the right upper side, which is equal to the center of the full model, a single notch under the same geometry used for the tensile tests was designed to describe the cracking model. Displacement boundary conditions were applied, u (y) = 0 for symmetric boundaries and u (x) = 0 for directional fixation boundaries. A simulation case for illustrating deformed meshes and their calculated stress contours is depicted in Fig. 3.2 (b). A mesh refinement box in Fig. 3.2 (c) shows the calculated contour of σ_vm distribution based on an arbitrarily given σ_{ac} and a_c.

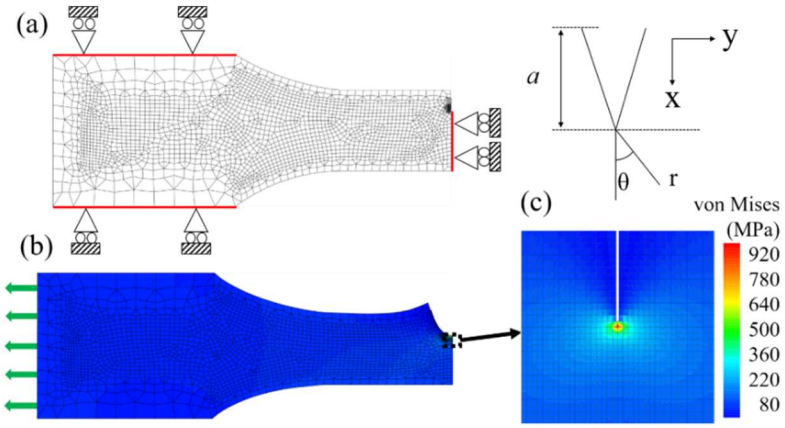

Fig. 3.2 Investigated FEA model, (a) finite element meshes based on half-cut geometry with a single notch, (b) half-cut stress distribution and (c) detailed mesh refinement box including the crack tip.

The FEA model with the mesh refinement area was designed, which includes a crack. In the refinement box, 1152 elements were used based on the quadratic interpolation function. If the a varies, it can be moved in the corresponding location including further crack tip. The meshes as much as available were considered under our calculation resources. The data sets were analyzed based on the two-dimensional von Mises yield criterion.

3.3 Results

3.3.1 Evaluation of fracture toughness

The true stress-strain results are plotted in Fig. 3.3. The modified mechanical properties affected by the conditions of HDPEC were listed in Table 3.2. A series of σ_y was determined from the 0.2 % proof stress. Plasticity constants such as m and n were estimated by the data-fitting based on the following working hardening rule [2],

$$\varepsilon = \frac{\sigma}{E} + \left(\frac{\sigma}{m}\right)^{1/n}. \tag{3.1}$$

Here, the E was determined by elastic rule $\sigma = E\ \varepsilon_{\mathrm{e}}$. Based on Table 2.2 of chapter 2, E =195 GPa and ν = 0.295 [9] were used for FEA evaluations. The tensile result of case D could be deemed as the most effective application manner. It was caused by increasing the p under the same total applied time.

Table 3.2 Material properties determined by the fitting with tensile results.

Cases	**A**	**B**	**C**	**D**	**E**
σ_{y} (MPa)	352.3	360.1	366.4	408.1	390.2
n	0.363	0.366	0.358	0.313	0.323
m	1272.1	1280.1	1285.7	1338.2	1282.6

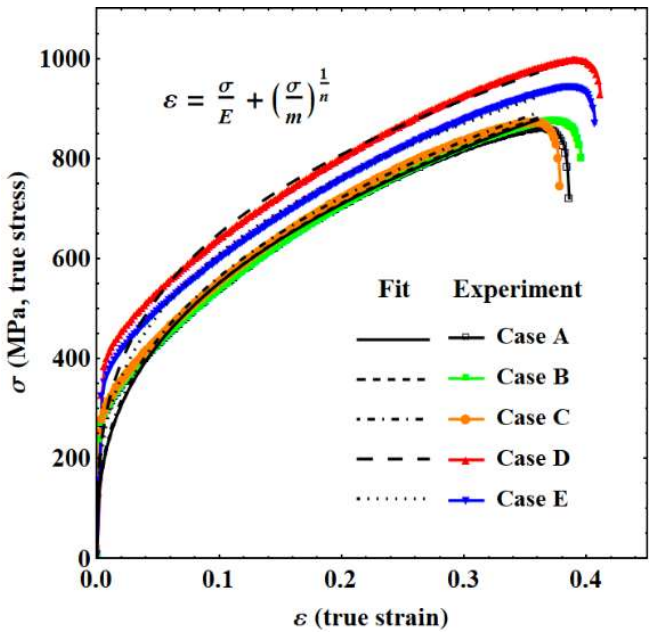

Fig. 3.3 True stress-strain results from the tensile tests for cases A, B, C, D and E.

Uncertainty of the curve fitting in the elastic regime was shown. It has been reported in quasi-ductile materials [20]. Nonetheless, a prediction of the plasticity constants by the fitting can provide a practical application to reduce the calculation cost of FEA. Based on the variables such as E, ν, σ_y and n depending on m, the simulation inputs were determined and the corresponding analysis made it possible. Numerically predicted K_c for each condition of HDPEC was plotted in the inset figure of Fig. 3.4. Typical K_c of case A was used as the reference value of this material, which is approximately 101 MPa·m$^{1/2}$ [21]. To predict the modified values of K_c by the applied HDPEC, a crack length calculated by the evaluation of case A was substituted to the Eq. (1.5) in chapter 1, thereby could be calculated for other cases.

Figure 3.4 illustrates the predicted relationship between σ_{ac} and a_c based on Eq. (1.6) of chapter 1 and FEA calculation. Where the r_y was predicted by a combination of Eq. (1.2) of chapter 1 and $r_y = 1/[6\pi(1+n)](K/\sigma_y)^2$. The data-sets plotted by symbols indicate the calculated values in FEA as the critical fracture.

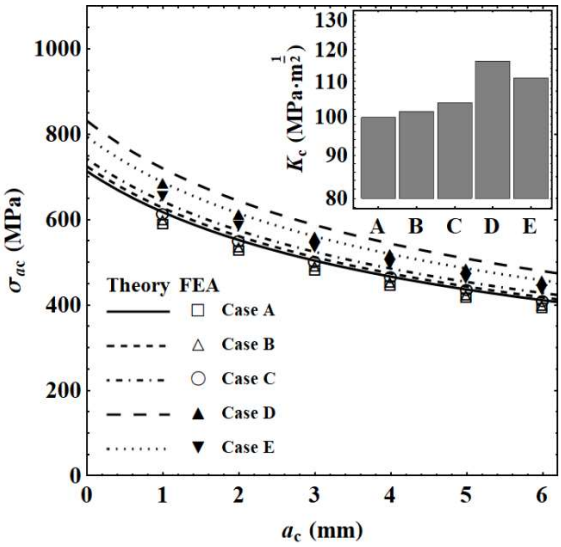

Fig. 3.4 Evaluated results for the relationship between critical applied stresses and critical crack lengths. Inset: bar plot of evaluated fracture toughness.

The evaluated K_c increases with increasing the j, that is, higher σ_{ac} at the given a_c is required to reach the corresponding K_c. The higher j (cases D and E) has a better effect than that of the lower one such as case B and case C. In terms of critical fracture conditions, it can suggest that a higher j induces higher σ_{ac} in threshold cracking. Furthermore, the evaluated result shows that the HDPEC condition of two pulses such as case D has more effectiveness than that of one pulse such as case E, even though they were the same total applied time ($t_d \times p = 10$ ms). The evaluated results indicate that the modified mechanical properties play a significantly crucial role in the evaluated values of σ_{ac} and a_c.

3.3.2 Improved fracture thresholds

Based on the evaluated critical fracture values in Fig. 3.4, the stress distribution near the crack tip at fracture was calculated with the FEA. Figure 3.5 shows the calculated values of σ_{vm} based on Eq. (2.3) as a function of the distance r along with X-direction from the crack tip, which is the propagation direction ($\theta = 0$). A constant value of a_c = 1 mm was used to make typically an example of fracture crack for this simulation. The evaluated values of σ_{vm} in cases B, C, D and E were higher than those of case A under any distance. The calculated values of σ_{vm} were plotted in the range of $r \geq r_y$. An assumption by singularity-dominated condition was used as follows [3],

$$\sigma_{vm} = \frac{\sigma_a\,(a+r)}{\sqrt{2ar+r^2}} \qquad \left(r \geq r_y\right). \tag{3.2}$$

Thus, the values of σ_{cm} could be evaluated by the calculated values of σ_{vm} at $r = r_y$.

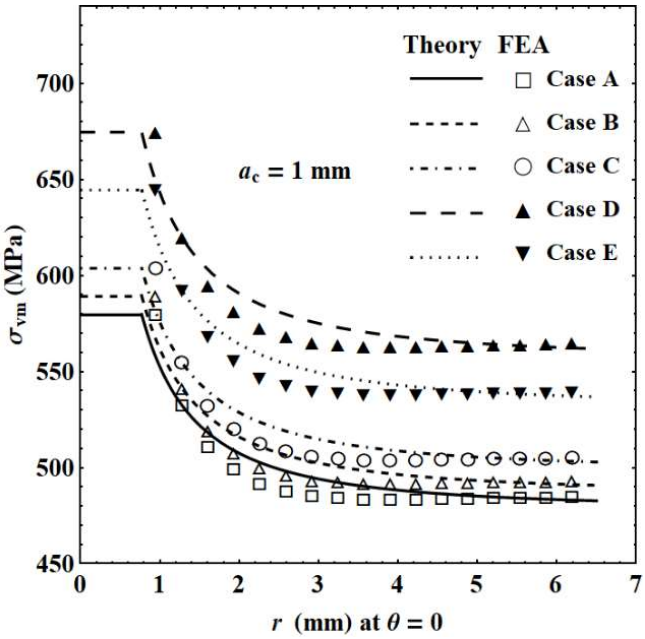

Fig. 3.5 Calculated stress distribution by von Mises criterion as a function of the distances from crack tips at $\theta = 0$.

Figure 3.6 illustrates the determination of $\sigma_{\mathrm{cm}}/\sigma_{\mathrm{cm}}^{\mathrm{o}}$, i.e., σ_{cm} normalized by $\sigma_{\mathrm{cm}}^{\mathrm{o}}$ from σ_{cm} of case A. The repeat calculations for different crack lengths could give data-sets of $\sigma_{\mathrm{cm}}/\sigma_{\mathrm{cm}}^{\mathrm{o}}$, thereby the enhanced values were determined, where a/w is a series of a per w in the geometry of FEA. To evaluate quantitatively the effectiveness of fracture resistance, the inset equation of Fig. 3.6 was used. The inset figure depicts the increased ratio of σ_{cm} based on the HDPEC condition. The increasing effect of HDPEC was verified. The increased ratio of cases B, C, D and E is entirely higher than the ratio of case A. Remarkably, case D reveals the increased ratio of 17.2 % which can be thought of as the best HDPEC condition.

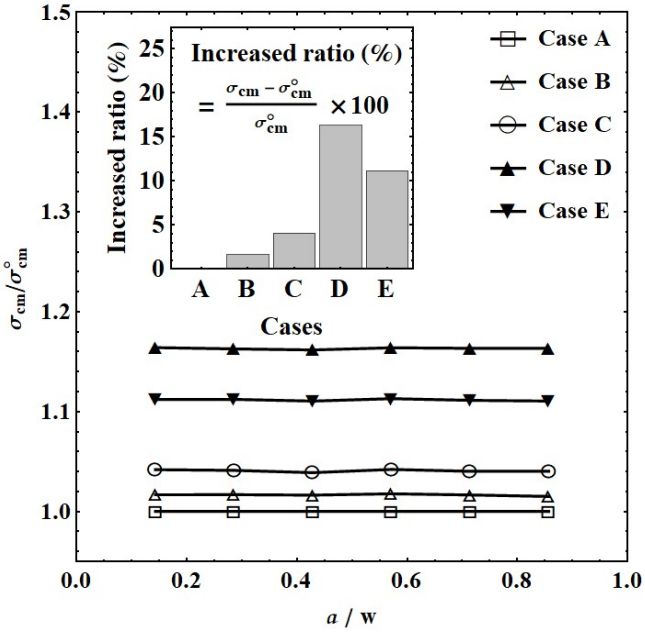

Fig. 3.6 Calculated FEA results for normalized local fracture strength as a function of normalized crack length. Inset: increased ratio of local fracture strength of each case.

To evaluate quantitatively the value of K_c, the following equation can be proposed [3,22],

$$K = \sigma_a \sqrt{\pi\, a}\, f(\frac{a}{w}) \,, \tag{3.3}$$

then critical conditions of Eq. (3.3) gives Eq. (3.4),

$$K_c \propto \sigma_{cm} \sqrt{a_c}\, f\left(\frac{a}{w}\right) , \tag{3.4}$$

where the location function $f(a/w)$ depending on a and w can be used with an assumption for periodic collinear cracks, $f(a/w) = [2\, w/(\pi a) \tan(\pi a/(2\, w))]^{1/2}$. The inset figure of Fig. 3.7 depicts the evaluated values of K versus the a/w with analytical

and FEA results. It shows an agreement between the two approaches. Because typical fracture can occur when the K reaches the K_c as a critical value, i.e., $K/K_c = 1$, equation (3.5) can be proposed to decide the increased ratio as the effect of HDPEC,

$$\frac{K_c}{K_c^o} = \frac{\sigma_{cm}}{\sigma_{cm}^o}\sqrt{\frac{a_c}{a_c^o}}, \tag{3.5}$$

where K_c^o, σ_{cm}^o, and a_c^o are the initial values of K_c, σ_{cm}, and a_c. Figure 3.7 indicates the evaluated values of K_c/K_c^o. The increased ratio is plotted as a bar scale in Fig. 3.8. The enhancement of K_c/K_c^o in cases B, C, D, and E is successfully revealed. The increased ratio of case D was evaluated to be 16.26 % as the highest one. It would be thought that the improvement of K_c could be achieved under the HDPEC condition of case D.

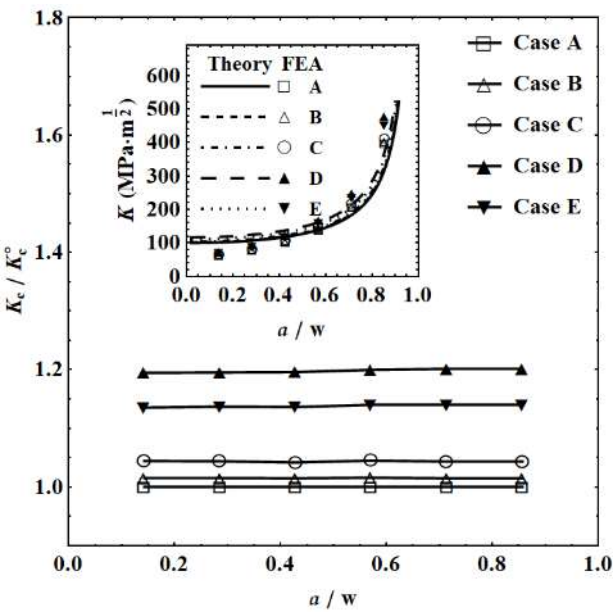

Fig. 3.7 Evaluation of normalized critical fracture toughness along with crack length. Inset: evaluated values of K based on FEA and analytical results.

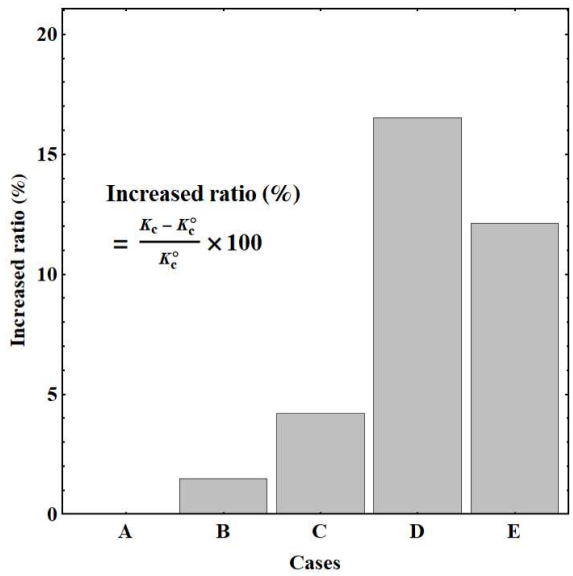

Fig. 3.8 Increased ratio (%) of improved fracture toughness compared with original fracture toughness.

3.3.3 Evaluation by crack profiles

In terms of fracture parameters to understand the level of improvement, the CTODs (δ) can also be taken into account. Equation (3.6) yields the relationship between K and δ based on the values of E and σ_y [3],

$$\delta = \frac{K^2}{\beta\, E\, \sigma_y}\,, \tag{3.6}$$

where β indicates a non-dimensional constant. The critical values of CTOD (δ_c) can be calculated based on the strip-yield assumption as follows,

$$\delta_c = \frac{{K_c}^2}{\beta\, E\, \sigma_y} = \frac{8\, \sigma_y\, a_c}{\beta\, \pi\, E} \ln \sec\left(\frac{\pi\, \sigma_a}{2\, \sigma_y}\right)\ . \tag{3.7}$$

It is a criterion by crack profiles at fracture. A fracture occurs when δ reached δ_c.

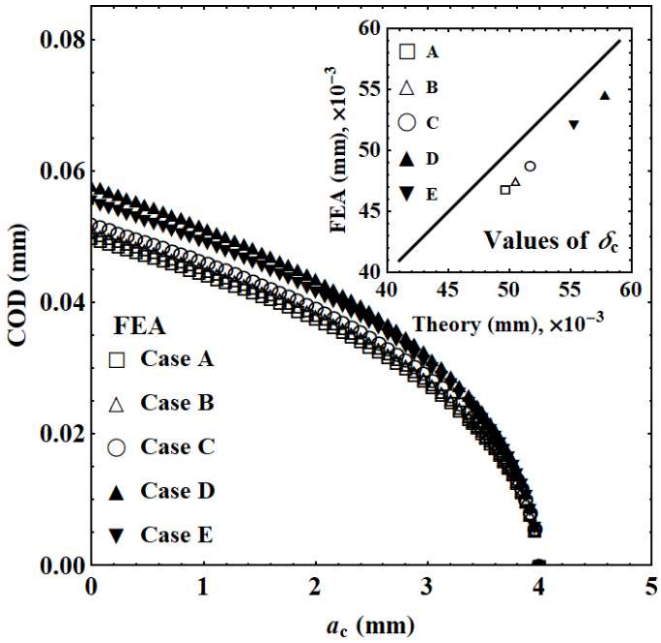

Fig. 3.9 COD profiles calculated by FEA. Inset: comparison of critical CTODs using FEA and theoretical approaches.

Figure 3.9 illustrates the simulated profiles of COD in cases A, B, C, D and E. Here, the a_c of 4 mm was used. The calculated values of cases B, C, D and E were larger than case A at any crack position. In the inset figure of Fig. 3.9, a comparison of CTODs between the analytical and FEA results was shown. The resulted values of δ_c in the theory-axis of the inset figure were calculated by Eq. (3.7). Where $\beta = 2$ was assumed. The analytical predicted by Eq. (3.7) and FEA results have an agreement, in which the values of K_c and σ_y are associated with crack tip dulling. In Fig. 3.10, the critical values of CTOD were simultaneously plotted with the predicted lines of cases A and D based on Eq. (3.7). The values of CTOD obtained in cases B, C, D, and E are larger than those of case A. In general, a crack tip tends to be blunted because of the dominant plasticity. These simulation results show the dulling near the crack tip due to their plasticity.

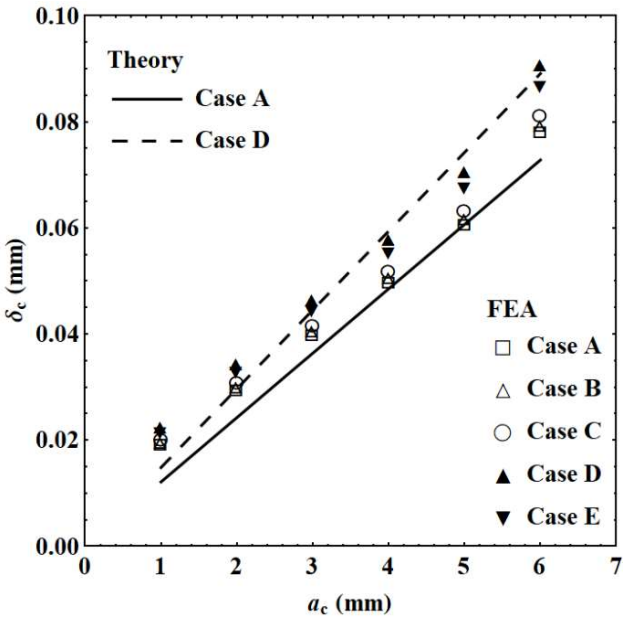

Fig. 3.10 Critical CTOD calculated by FEA as a function of critical crack length. The predicted lines of cases A and D are simultaneously plotted.

The prediction in Fig. 3.10 could provide an alternative approach in terms of fracture parameters. The calculated FEA results show a gradual increase in δ_c. The CODs are determined by equivalent state between σ_{ac} and a_c. The increase in σ_y would provide higher crack tip dulling than initial material, which means the improvement of resistance in crack propagation.

3.4 Discussion

This chapter has been elaborated on fracture mechanics-based FEA evaluation of the improved fracture parameters by the application of HDPEC. The material properties obtained in tensile tests were used to evaluate critical fracture parameters such as σ_{cm}, K_c, and CTOD. Based on the presented results, the following discussion can be made.

3.4.1 Evaluation of improved fracture parameters

To assess the improved quality of critical fracture affected by HDPEC, the following equations can be used,

$$\frac{K_c}{K_c^o} > 1 \,, \tag{3.8}$$

$$\frac{K_c}{K_c^o} = 1 \,, \tag{3.9}$$

$$\frac{K_c}{K_c^o} < 1 \,. \tag{3.10}$$

Equations (3.8-3.10) describe whether the material has an improved critical value of fracture or not. Based on the improved and original states of critical value, i.e., K_c/K_c^o, if $K_c/K_c^o > 1$, the K_c is improved by the application of HDPEC. By contrast, $K_c/K_c^o < 1$ indicates that damage to the material can be caused. As shown in Fig. 3.8, the improvement of K_c was demonstrated. It could provide a method to evaluate the degree of improved K_c by the application of HDPEC. This simulation results with changed material properties showed an increase in ductility as the effect of HDPEC. Dulled crack tip indicates the increment of ductility. In general, residual compressive stress at the crack by the application of HDPEC plays a significantly important role in the resistance of crack propagation, while residual tensile stress has a harmful effect [23]. The increase of ductility presented in this chapter can coexist with the effect of residual compressive stress, thereby both effects could resist crack propagation.

3.4.2 Strengthening role of HDPEC

As the effect of HDPEC, getting a higher value of σ_y and a lower value of n was verified. When the j is high, the improved fracture property is high. The cases of 150 A/mm^2 were not significantly influenced by the type of applied p of HDPEC, whereas the different improvement was revealed in cases of 300 A/mm^2 even though the total applied time of HDPEC was the same. One reason resulted in the different results, which is induced by different densities of HDPEC, can be thought due to ΔT_J. Based on the Eq. (1.11) of chapter 1 [24] with material constants ($\rho = 7.4 \times 10^{-7}\ \Omega \cdot \mathrm{m}$, $C_p = 502\ \mathrm{J/(kg\ K)}$, and $d_m = 7.87 \times 10^3\ \mathrm{kg/m^3}$) and $t = 10\ \mathrm{ms}$, the values of ΔT_J for 150 A/mm^2 and 300 A/mm^2 were predicted as 42.1 and 168.6°C, respectively. The higher ΔT_J could often have more energy, thereby could promote the modification of material properties. On the other hand, the high-density electric current can induce the collective drift electrons. The EWF defined in chapter 1 can push atoms as a force to promote their motion [25]. It has been demonstrated that the microstructures such as dislocation, crystal texture, grain size, and phase structure could be changed by the high-density electric current [9-13,24,26,27]. Thus, the most important factor for the effect of HDPEC is considered to be owing to EWF. The increased effect of EWF with increasing the j increases the improvement of material strength. Furthermore, cases of two pulses could increase the EWF compared with one pulse owing to the abrupt increment of voltage under the same total applied time of HDPEC.

3.5 Summary

In this chapter, the improvement of fracture characteristics of the material by the application of HDPEC was demonstrated based on a combination of a fracture mechanics-

based theoretical framework and cracking simulation using FEA.

The σ_{y} was increased and the n decreased with the increased j. The improved mechanical properties can be considered to be owing to the EWF because EWF can modify the microstructure and necessarily accompanies changes in mechanical properties. Results from the FEA depict that the distribution of σ_{cm} near the crack tip was increased with the increased j. The modified degree by higher j and more p of HDPEC shows the higher improvement of σ_{cm}. Cases applied by HDPEC need more stress to further propagate a crack than those without the application of HDPEC. The improvement of K_{c} was also demonstrated by FEA. It shows the best efficiency under the higher j and multiple p of HDPEC. The results of CTODs indicate the plasticity-induced dulling of the crack tip. An agreement between the theory and FEA was verified.

Consequently, the application of HDPEC could give advantages to resist crack propagation based on the modified material properties. The improvement of σ_{cm} near the crack tip, K_{c} and δ_{c} was achieved.

References

[1] A. A. Griffith, The phenomena of rupture and flow in solids, Philosophical Transactions of the Royal Society A. 221 (1921) 163–198. https://doi.org/10.1098/rsta.1921.0006.

[2] R. I. Stephens, A. Fatemi, R. R. Stephens and H. O. Fuchs: *Metal fatigue in engineering*, (John Wiley & Sons, New York, 2000).

[3] T. L. Anderson: *Fracture mechanics fundamentals and applications*, (CRC press Taylor&Francis, Florida, 2017).

[4] S. Suresh, R. O. Ritchie, A geometric model for fatigue crack closure induced by

fracture surface roughness, Metallurgical Transactions A. 13 (1982) 1627–1631. https://doi.org/10.1007/BF02644803.

[5] Ilhamdi, T. Kakiuchi, H. Miura, T. Fukihara, Y. Uematsu, Fatigue behavior of multi-directionally forged commercial purity grade 2 Ti plate in laboratory air and Ringer's solution, Materials Transactions. 59 (2018) 1296–1303. https://doi.org/10.2320/matertrans.M2018075.

[6] A. G. Evans, Slow crack growth in brittle materials under dynamic loading conditions, International Journal of Fracture. 10 (1974) 251–259. https://doi.org/10.1007/BF00113930.

[7] H. Somekawa, Effect of alloying elements on fracture toughness and ductility in magnesium binary alloys; a review, Materials Transactions. 61 (2020) 1–13. https://doi.org/10.2320/matertrans.MT-M2019185.

[8] H. Y. Liu, G. T. Wang, Y. W. Mai, Y. Zeng, On fracture toughness of nano-particle modified epoxy, Composites Part B: Engineering. 42 (2011) 2170–2175. https://doi.org/10.1016/j.compositesb.2011.05.014.

[9] A. Hosoi, T. Nagahama, Y. Ju, Fatigue crack healing by a controlled high density electric current field, Materials Science and Engineering: A. 533 (2012) 38–42. https://doi.org/10.1016/j.msea.2011.11.024.

[10] Y. Tang, A. Hosoi, Y. Morita, Y. Ju, Restoration of fatigue damage in stainless steel by high-density electric current, International Journal of Fatigue. 56 (2013) 69–74. http://dx.doi.org/10.1016/j.ijfatigue.2013.08.012.

[11] Y. Tang, A. Hosoi, Y. Iwase, Y. Ju, Effect of high-density electric current on the microstructure and fatigue crack initiation of stainless steel, Materials Transactions. 54 (2013) 2085–2092. https://doi.org/10.2320/matertrans.M2013198.

[12] J. Jung, Y. Ju, Y. Morita, Y. Toku, Y. Uematsu, Delaying effect of high-density electric current on fatigue crack growth in A6061-T6 aluminum alloy, Materials Transactions. 57 (2016) 2104–2109. https://doi.org/10.2320/matertrans.M2016240.

[13] J. Jung, Y. Ju, Y. Morita, Y. Toku, Enhancement of fatigue life of aluminum alloy affected by the density of pulsed electric current, International Journal of Fatigue. 103 (2017) 419–425. https://doi.org/10.1016/j.ijfatigue.2017.06.021.

[14] K. Toishi, Y. Miki, N. Kikuchi, Simulation of crack initiation on the slab in continuous casting machine by FEM, ISIJ International. 59 (2019) 865–871. https://doi.org/10.2355/isijinternational.ISIJINT-2018-679.

[15] D. Kujawski, F. Ellyin, On the size of plastic zone ahead of crack tip, Engineering Fracture Mechanics. 25 (1986) 229–236. https://doi.org/10.1016/0013-7944(86)90219-5.

[16] K. H. Benrahou, M. Benguediab, M. Belhouari, M. Nait-Abdelaziz, A. Imad, Estimation of the plastic zone by finite element method under mixed mode (I and II) loading, Computational Materials Science. 38 (2007) 595–601. https://doi.org/10.1016/j.commatsci.2006.04.001.

[17] S. D. Antolovich, R. W. Armstrong, Plastic strain localization in metals: origins and consequences, Progress in Materials Science. 59 (2014) 1–160. https://doi.org/10.1016/j.pmatsci.2013.06.001.

[18] J. R. Rice, A path independent integral and the approximate analysis of strain concentration by notches and cracks, Journal of Applied Mechanics. 35 (1968) 379–386. https://doi.org/10.1115/1.3601206.

[19] D. E. Hauf, D. M. Parks, H. Lee, A modified effective crack-length formulation in elastic-plastic fracture mechanics, Mechanics of Materials. 20 (1995) 273–289. https://doi.org/10.1016/0167-6636(94)00058-1.

[20] M. Kamaya, Ramberg–Osgood type stress–strain curve estimation using yield and ultimate strengths for failure assessments, International Journal of Pressure Vessels and Piping. 137 (2016) 1–12. https://doi.org/10.1016/j.ijpvp.2015.04.001.

[21] W. J. Mills, Fracture toughness of type 304 and 316 stainless steels and their welds, International Materials Reviews. 42 (1997) 45–82. https://doi.org/10.1179/imr.1997.42.2.45.

[22] M. Kachanov, Elastic solids with many cracks and related problems. Advances in Applied Mechanics. 30 (1993) 259-445.https://doi.org/10.1016/S0065-2156(08)70176-5.

[23] A. Hosoi, T. Yano, Y. Morita, Y. Ju, Quantitative evaluation of the displacement distribution and stress intensity factor of fatigue cracks healed by a controlled high-density electric current field, Fatigue & Fracture of Engineering Materials & Structures. 37 (2014) 1025–1033. https://doi.org/10.1111/ffe.12175.

[24] D. Waryoba, Z. Islam, B. Wang, A. Haque, Recrystallization mechanisms of Zircaloy-4 alloy annealed by electric current, Journal of Alloys and Compounds. 820 (2020) 153409. https://doi.org/10.1016/j.jallcom.2019.153409.

[25] H. Conrad, Electroplasticity in metals and ceramics, Materials Science and Engineering A. 287 (2000) 276-287. https://doi.org/10.1016/S0921-5093(00)00786-3.

[26] W. Dai, X. Wang, H. Zhao, X. Zhao, Effect of electric current on microstructural evolution in a cold-rolled 3% Si steel, Materials Transactions. 53 (2012) 229–233. https://doi.org/10.2320/matertrans.M2011272.

[27] Y. Sakaida, K. Iwai, S. Asai, Crystal alignment of titanium under simultaneous imposition of electric current and magnetic field, Materials Transactions. 48 (2007) 2872–2876. https://doi.org/10.2320/matertrans.MI200703.

Chapter 4 Material strengthening through the modification of microstructure

In this chapter, it has been elaborated to understand why the application of HDPEC could improve mechanical properties such as σ_y, ultimate strength σ_u and strain at fracture ε_f based on the tensile results of chapter 3. Optimized conditions of HDPEC were examined. Microstructure observations were performed to find out the comprehensive mechanisms, which explain the improved tensile properties such as σ_y and σ_u with an increase in ε_f. Based on grain boundary engineering (GBE), elemental analysis associated with phase transformation, advantages of HDPEC application for the material strength and the reduction of $Cr_{23}C_6$ are proposed in this chapter. The ΔT_J by Joule-heating is controlled to make the effect of EWF stand out.

4.1 Introduction

Over the past few decades, GBE has been regarded as one of the effective methods to improve mechanical properties because intergranular properties play important roles to determine the strength of the material. Many researchers have attempted to ensure better mechanical properties in various stainless steels through modifications of GB characteristics [1-5]. Typical types of GBs such as LAGBs, HAGBs and $\sum 3$ TBs defined by different misorientation angles have been purposely modified with various treatment methods. Creating favorable GB characteristics for the material strength contributes to resolving one of the disadvantages of the material as presented in chapter 1.

In addition, decreasing $Cr_{23}C_6$ in the surrounding of GBs and TBs is the other

requirement to ensure better material properties of the material. From a thermal process point of view, it has been reported that controlling heat processes induces the dissolution of $Cr_{23}C_6$ because the material exhibits thermodynamic equilibrium between austenite grains, ferrite grains and $Cr_{23}C_6$ [6]. The reduction of $Cr_{23}C_6$ by the thermal process improves the material properties, but this can only be considered in metallurgical manufacturing and heat treatment processes. To meet the needs for simple and rapid modification of the material properties, treatment methods without metallurgical manufacturing and heat treatment processes have been always required in industrial sites.

As introduced in Chapter 1 for the effect of HDPEC in metals, this process generally accompanies a ΔT_J by Joule heating. High ΔT_J in metals inevitably changes metallurgical state so that it should be explained in conjunction with the thermally activated modification of material properties rather than that by EWF. In this manner, a comprehensive mechanism in the variation of grain size was recently introduced [7]. The determination of grain refinement or growth depends on conditions of pulsed electric current. Grain refinement can be expected in the relatively lower j whereas grain growth occurs in higher j [7]. Higher ΔT_J by a higher j can often have a synergistic effect with EWF. Remarkably, both effects describe the potential of applied electric current for the modification of microstructures. Many reports show advantages of electric current both/either the Joule-heating and/or EWF [7-10], and a recent report proposed a new avenue, namely thermal phonon effect instead of the effect of EWF and Joule-heating [11]. It was shown to demonstrate the thermal phonon effect through a comparison between under matching temperatures and under steady current levels below 200, 70 and 40 A/mm^2 for copper, iron and titanium, respectively. Nevertheless, microstructure evolution under pulsed electric current instead of steady current conditions was still not

understood to identify the effects of EWF. Abruptly increased pulse effects should be discussed. Further, if the T_R by the application of electric current is significantly controlled below certain temperatures of materials, the effect of EWF can be increased and contribute mainly to the modification of microstructure. Thus, it needs to prove that the effect of EWF dominantly contributes to the modification of microstructure.

In addition, it remains still unclear and has not been reported how grain size could be changed, what mechanisms could contribute to the improvement of material strength, and what is the role of electric current in materials. Furthermore, modification of microstructure by dislocation motion through EWF [8,12,13] could give a motivation to induce strengthening of the material. Thus, it has been required to prove the role of EWF acting in microstructures of the material and to propose a reasonable description of modifications of GB characteristics presented in grains and GBs by the HDPEC.

In this chapter, the modification of microstructure by the EWF-enhanced HDPEC effect was demonstrated. The T_R by HDPEC was significantly confined below a certain temperature of the material so that the effect of Joule-heating can be negligible. In terms of GBE, evolutions of microstructure were examined based on the grain boundary characteristics distribution (GBCD) among LAGBs, HAGBs and $\sum$ 3 TBs using the EBSD method. A selected area was observed using FESEM to verify changed GB characteristics in the GBCD plot. The STEM was used to support the explanation of the results in microstructural evolutions. EDS was also used to examine elemental rearrangements (Cr, Ni and C) in the surrounding of the grains (top view) and CSA of the associated grains. Evolutions of $Cr_{23}C_6$ and δ-ferrite were confirmed in EDS and EBSD phase maps. The eutectoid formula, $Cr_{23}C_6$, + γ ↔ δ, was employed to explain variations of $Cr_{23}C_6$ and δ-ferrite between γ-austenite grains. Mechanisms based on microstructure

evolutions were proposed to explain how to achieve the strengthening of the material with an increase in ε_f as the effect of HDPEC.

4.2 Tensile tests under controlled temperature rising

Uniaxial tensile tests were performed to obtain modified mechanical properties such as σ_y, σ_u and ε_f. In Table 4.1, a series of applied conditions of HDPEC and corresponding maximum T_R are listed. The j, p and t_d are defined as treatment parameters. The untreated sample is denoted as S_1. The treatment through 1 p by j of 200 A/mm^2, the treatment through 1 p by j of 400 A/mm^2 and the treatment through 2 p by j of 400 A/mm^2 are denoted as S_2, S_3 and S_4, respectively. Thus, not only the effect of j is distinguished by S_1, S_2 and S_3 but also the effect of p of HDPEC is considered by S_1, S_3 and S_4. The T_R in Table 4.1 was measured at the center of the sample geometry. It should be noted that a cooling time between two pulses applied to S_4 was sufficiently taken to reach the T_r after the initial pulse. In the predicted T_R, equation (1.11) of chapter 1 was used based on T_r of 25°C. Where the values in this calculation are ρ = 7.4×10^{-7} Ω·m, C_p = 502 J/(kg·K)) and d_m = 7870 kg/m^3.

Table 4.1 Applied conditions of HDPEC and the corresponding temperature rising.

Group	Density (j), A/mm^2	The number of pulses (p), times	Duration time (t_d), ms	Maximum raised temperature (T_R), °C	
				Prediction	Measurement
S_1			Untreated		
S_2	200	1	5	62.5	66.5
S_3	400	1	5	174.8	185.0
S_4	400	2	10	174.8+174.8	185.0+185.0

Remark: the second pulse was applied after the sample reached to T_r.

4.3 Results

4.3.1 Grain boundary characteristics and grain refinement

Figure 4.1 shows the inverse pole figures (IPFs) and corresponding {101} pole figures (PFs) with the measured GBCD and the mechanical properties in uniaxial tensile tests. The entire tendencies were examined based on the EBSD maps of Fig. 4.1 (a and b). The rolling direction (RD), transverse direction (TD) and normal direction (ND) are denoted. In Fig. 4.1 (a), the IPFs of S_3 and S_4 revealed noticeable changes in crystal orientation and grain size while the IPF of S_2 showed a slight difference compared with that of S_1. In Fig. 4.1 (b), the {101} PFs of S_2 and S_3 display a gradual increase in the maximum intensity of the {101} orientations, that is, an increase in the texture intensity was induced by the increased j. Especially, a significant crystallographic re-orientation of {101} was revealed by the pulse effect in the S_4 of Fig. 4.1 (b). It means that the increases in j and p of the HDPEC simultaneously contribute to the increase of the orientations. The corresponding evolutions of GBCD are shown in Fig. 4.1 (c). In the general category, fractions of LAGBs, HAGBs and ∑ 3 TBs were taken into account as defined in Table 2.4 of chapter 2. Relatively high fractions of HAGBs and ∑ 3 TBs and a lower fraction of LAGBs were reached through the heat treatment beforehand. After the HDPEC treatment, a significant increase of the fractions of HAGBs was observed with the decrease of the fraction of ∑ 3 TBs. Meanwhile, the fraction of LAGBs is slightly increased with the enhancement of HDPEC treatment. There were no significant changes in others, ∑ 3^n CSL boundaries such as ∑ 9 (38.94° around <110>), ∑ 27a (31.59° around <110>) and ∑ 27b (35.43° around <210>).

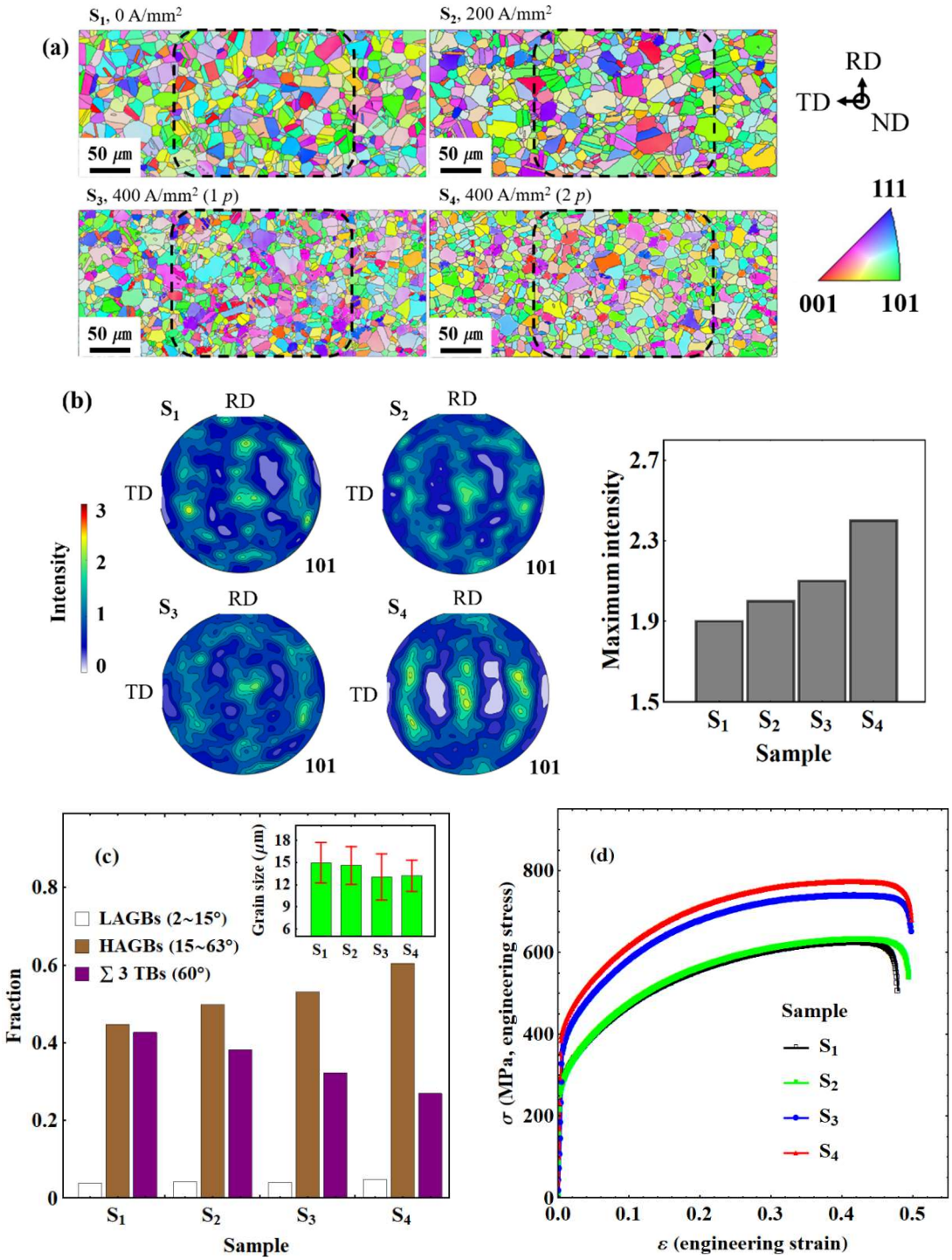

Fig. 4.1 Evolution of the microstructure at the center of sample based on EBSD results and their uniaxial tensile properties, (a) IPFs, (b) PFs and bar-plot of the maximum intensity of {101} orientations, (c) corresponding GBCD plot (Inset: measured grain sizes) and (d) engineering stress-strain curves.

In Fig. 4.1 (d), the results of uniaxial tensile tests show not only an increase in σ_y and σ_u but also a slight increase in ε_f. It can be thought that the effect of HDPEC contributes to improving overall mechanical properties. Invalidation of the strength-ductility trade-off was demonstrated in the stress-strain curves affected by HDPEC. In the inset of Fig. 4.1 (c), measured grain sizes from Fig. 4.1 (a) were plotted with error bars. As the increased effect of HDPEC, the grain size decreases. These results can be explained by the GBCD plot shown in Fig. 4.1 (c). The fractions of LAGBs and HAGBs under the same mapping area increase with the increased effect of HDPEC. Therefore, σ_y can be increased with the decrease of grain size due to the Hall-Petch strengthening [14,15], which has been successfully used to estimate theoretical σ_y and related Hall-Petch grain size d_{HP}, namely, $\sigma_y = \sigma_0 + k_{HP}/\sqrt{d_{HP}}$, where σ_0 and k_{HP} are the material constants. As a result, HDPEC induced Hall-Petch strengthening effect with the increase of LAGBs and HAGBs, which thereby increases the strength of the material owing to grain refinement.

4.3.2 Effect of pulse number

Since the T_R by Joule heating is controlled as listed in Table 4.1 below the certain temperature of the material. The temperature setting in this chapter (≤185°C) was significantly below typical temperatures that could have metallographic effects in the material such as austempering (≈ 350°C) and the minimum intended temperature in the phase diagram of austenitic stainless steel (≈ 400°C). Even there was no holding time at the T_R increased by HDPEC. Thus, we assume that the EWF owing to abruptly increased pulse is one of the main sources for the modification of microstructure. The modification process of microstructure between S_1 and S_3 and S_4 could be estimated based on the results in crystal texture, GBCD and strength of the material were related to grain size.

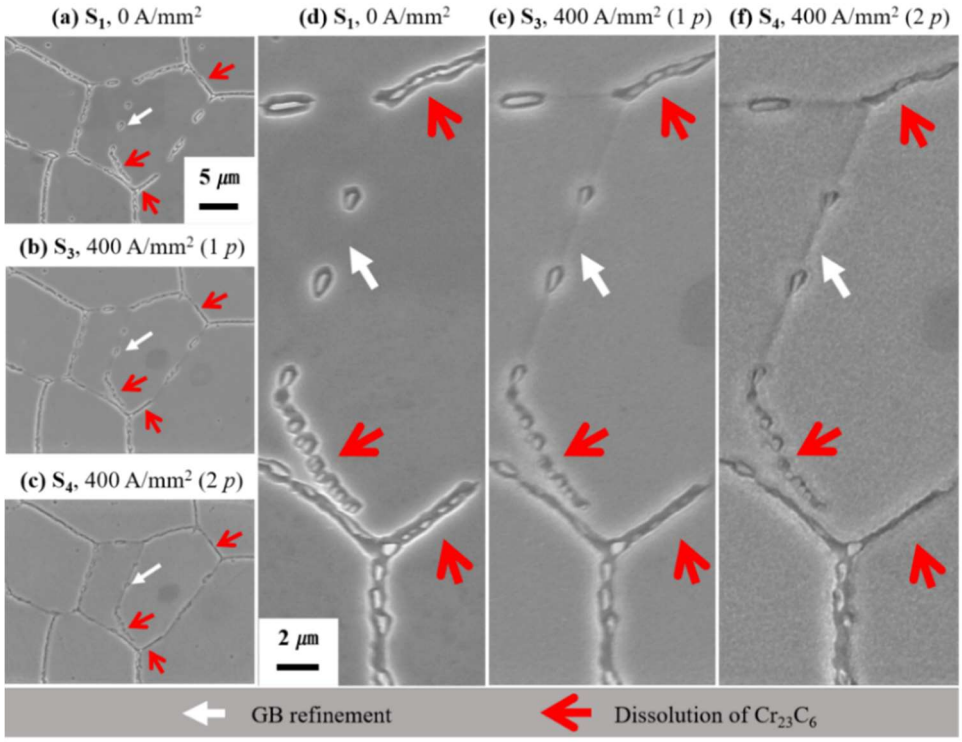

Fig. 4.2 FESEM images showing the variation of the grain by the pulse effect of HDPEC, (a) S_1, (b) S_3, (c) S_4 and (d-f) enlarged view for the area of interest.

The FESEM images in Fig. 4.2 (a-c) show the variation of GBs as the effect of p of HDPEC (enlarged in Fig. 4.2 (d-f)). As etched (Fig. 4.2 (a)) after heat treatment and polishing, the HAGBs and the $Cr_{23}C_6$ in the surrounding of the grain were highlighted. Once the HDPEC treatment was applied, new HAGBs with losing of the integrity of $\sum 3$ TBs occur and grain refinement happens, which is shown in Fig. 4.2 (b and e) by the white arrows. As the p of HDPEC was increased, strong grain refinement was made as shown in Fig. 4.2 (c and f). This phenomenon clarifies the variation of the GBCD plot in Fig. 4.1 (c).

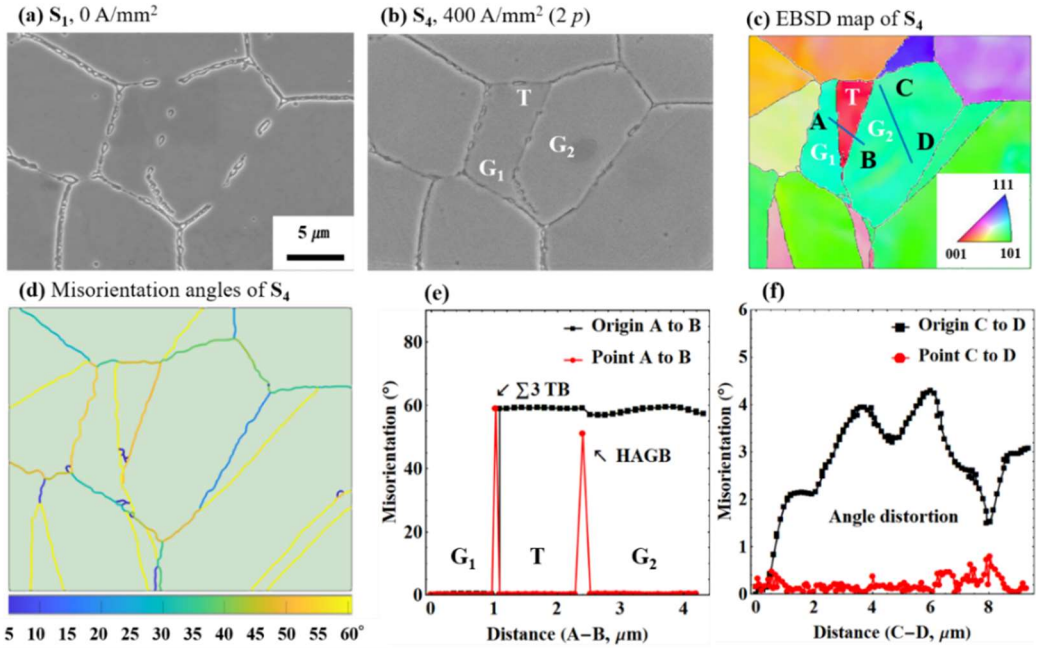

Fig. 4.3 Highlighted area for the grains (G_1, G_2: Grains and T: Twin) showing the transformation of misorientation-angles between GBs, (a-b) FESEM images of S_1 and S_4, (c) corresponding EBSD map of S_4, (d) misorientation-angle plots, (e) profile plots along with the line AB and (f) that of the line CD.

In Fig. 4.3, the EBSD map and the misorientation angles of GBs would help explain the process of grain refinement. The variation of misorientation angles in GBs is depicted with a color bar in Fig. 4.3 (d). In Fig. 4.3 (e), the corresponding profile of misorientation angles crossing over the refined GB was measured through line A-B of Fig. 4.3 (c). The variation in the plot describes the different angles between the G_1-T and T-G_2. In Fig. 4.3 (d), the refined HAGB from ∑ 3 TBs (between T and G_2) shows a lower misorientation angle than that of the ∑ 3 TBs between G_1 and T. Variation of the profile helps explain the misorientation angle plot in Fig. 4.3 (f). The misorientation angles along line C-D show an increasingly fluctuating angle within low angles (misorientation angle < 5°). It indicates that the variation of strain contour in the G_2 could be made by dislocation motion, and such strain field consequently modified the distribution of misorientation angles in

GBs, which led to the increase in HAGBs with the reduction of ∑ 3 TBs as analyzed in Fig. 4.1 (c). The other interesting point is that the fraction of LAGBs in Fig. 4.1 (c) can be explained as due to a higher strain field from dislocation motion (5° < misorientation angle). Once the HDPEC is applied, dislocations would move due to the EWF. In the dislocation pile-up model, moved dislocations inside of grains tend to be located near some structural sources such as GBs, TBs, solid solutions and precipitations. It can be thought that the number of dislocations increases near HAGBs, and add up to create one large LAGBs. The EBSD maps of Fig. 4.4 (c and d) show an increase in LAGBs (<1 μm) by the increased p of HDPEC. An increasing fraction of LAGBs contributes partly to the grain refinement with the creation of new GBs (Fig. 4.4 (c and d)).

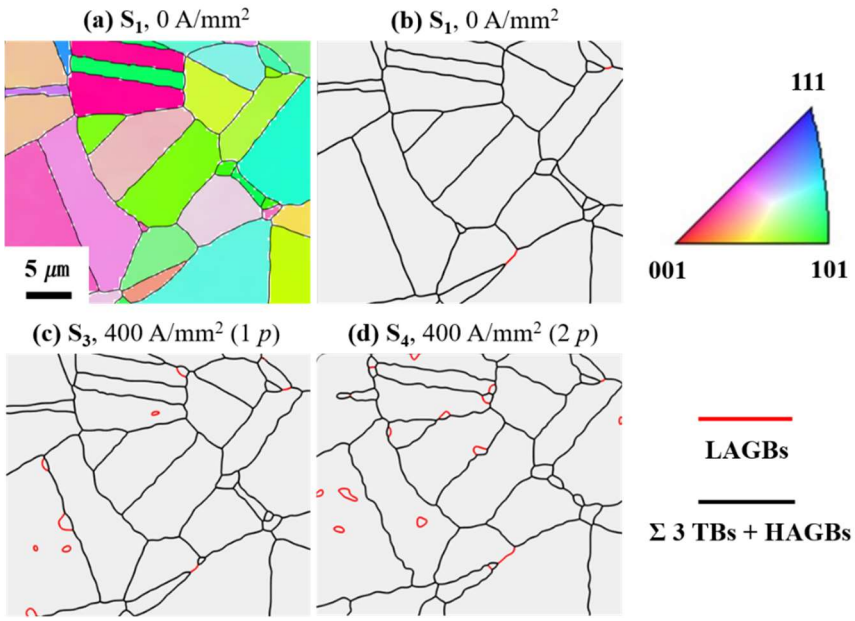

Fig. 4.4 Evolution of LAGBs by the pulse effect, (a) EBSD map of S_1, (b) the state of GBs of S_1 with few LAGBs after the annealing and (c-d) evolution of LAGBs by the effect of pulses for S_3 and S_4.

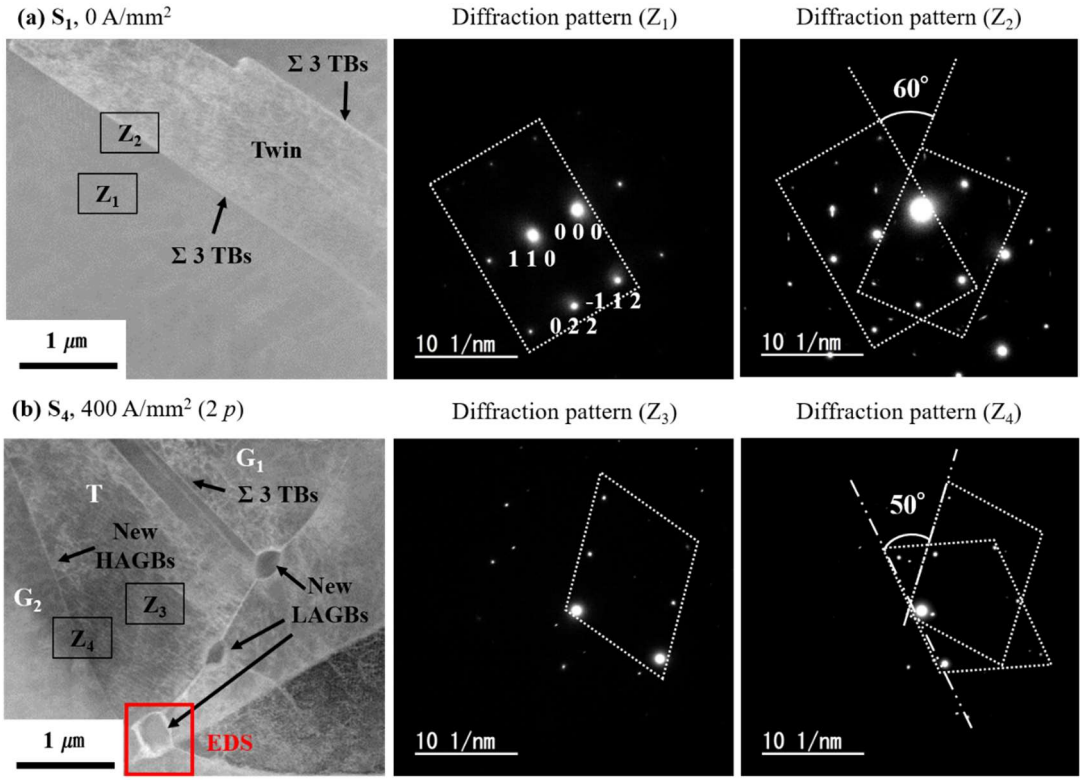

Fig. 4.5 TEM observation (CSA view) without and with the application of HDPEC, (a) TEM image of S_1 and SAED pattern and (b) that of S_4 as the effect of HDPEC.

Figure 4.5 (a) shows the TEM images (CSA view) and their selected area electron diffraction (SAED) patterns of S_1 as annealed. Typical ∑ 3 TBs were recognized. Where Z_1 is inside the grain and Z_2 is the selected area between inside the grain and twin. The SAED pattern in Z_2 depicts a typical crystallographic orientation of 60° owing to ∑ 3 TBs. On the other hand, the STEM images and its SAED pattern of S_4 (Fig. 4.5 (b)) show different aspects. Crystallographic changes were revealed and their orientation is no longer 60° by ∑ 3 TBs. In the EBSD map of Fig. 4.3 (d and e), changed HAGB from ∑ 3 TBs was shown as approximately 50°. The SAED pattern in Z_4 shows consistency with that of Fig.4.3 (e). Further, the creation of new LAGBs is shown in Fig. 4.4 (c and d) was also confirmed in TEM observation. Several LAGBs near GBs were newly formed as the

effect of HDPEC. In general, LAGBs have been specified as high-energy GBs and are known as a source for pinning dislocations. The newly formed LAGBs play a role in the strengthening of the material.

4.3.3 Dissolution of $Cr_{23}C_6$

The red arrows in Fig. 4.2 show the local dissolution of $Cr_{23}C_6$ as the effect of the p of HDPEC. Elemental analysis was employed for the given grain since the chemical feature of GBs is one of the assessment requirements to explain a variation of $Cr_{23}C_6$ for austenitic stainless steels.

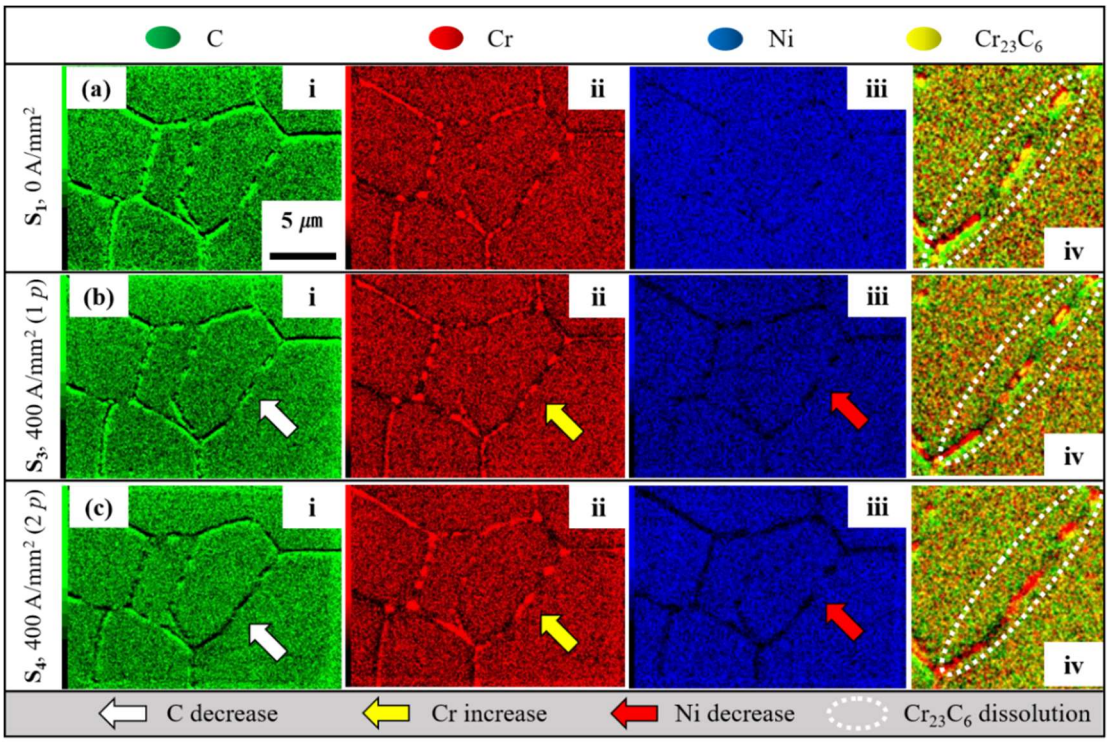

Fig. 4.6 FESEM-EDS elemental analysis of C-i, Cr-ii, Ni-iii, and $Cr_{23}C_6$-iv (C-Cr layered) for the densities and the number of HDPEC, (a) S_1, (b) S_3 and (c) S_4.

Figure 4.6 (a-c) shows elemental evolutions (top view) in C, Cr, Ni and C-Cr stacked ($Cr_{23}C_6$) maps under the conditions of HDPEC of the S_1, S_3 and S_4. In the C map of S_1 (i of Fig. 4.6 (a)), it can be seen that plenty of C along with GBs formed. When the HDPEC is applied as S_3 and S_4 (i of Fig. 4.6 (b and c)), the amount of C was decreased near GBs. The deepened black along with GBs indicates that C atoms tend to move to the inside of the grain as an effect of p of HDPEC. On the other hand, the tendency of Cr was different. The corresponding Cr maps (ii of Fig. 4.6 (a-c)) present the gradual increase of the amount of Cr near GBs as the p of HDPEC increases. In addition, Ni maps show decreasing tendencies along with GBs (iii of Fig. 4.6 (a-c)). As the p of HDPEC increases, an amount of Ni moves into grains from GBs. Based on the elemental evolution in iv of Fig. 4.6 (a-c), the decrease of $Cr_{23}C_6$ could be observed as the effect of the increased p of HDPEC.

To demonstrate elemental rearrangement in the interface (CSA view) between LAGBs and $Cr_{23}C_6$, STEM-EDS was used in the newly formed interface indicated by the red box in Fig. 4.5 (b). Figure 4.7 (a) shows the typical $Cr_{23}C_6$ and surrounding element states based on S_1. The count of elements in location B by the line plot indicates the base elemental distribution of $Cr_{23}C_6$. Compared with the line plot of Fig. 4.7 (a), figure 4.7 (b) depicts the changed distribution of elements. An increase in Cr and a decrease in Ni were revealed, that is, elemental changes explained in Fig. 4.6 are consistent with TEM-EDS observation in CSA. The elemental rearrangement in the surrounding of the grain shows the process of dissolution of $Cr_{23}C_6$ (a decrease in C, an increase in Cr and a decrease in Ni along with the GBs). The application of HDPEC made $Cr_{23}C_6$ dissolved and the dissolved Cr is located near reduced $Cr_{23}C_6$ whereas the amounts of Ni and Fe lost their location instead of the increase in Cr. This elemental change induces crystal rearrangement, thereby new LAGBs, which lead to creating subgrains, could be formed.

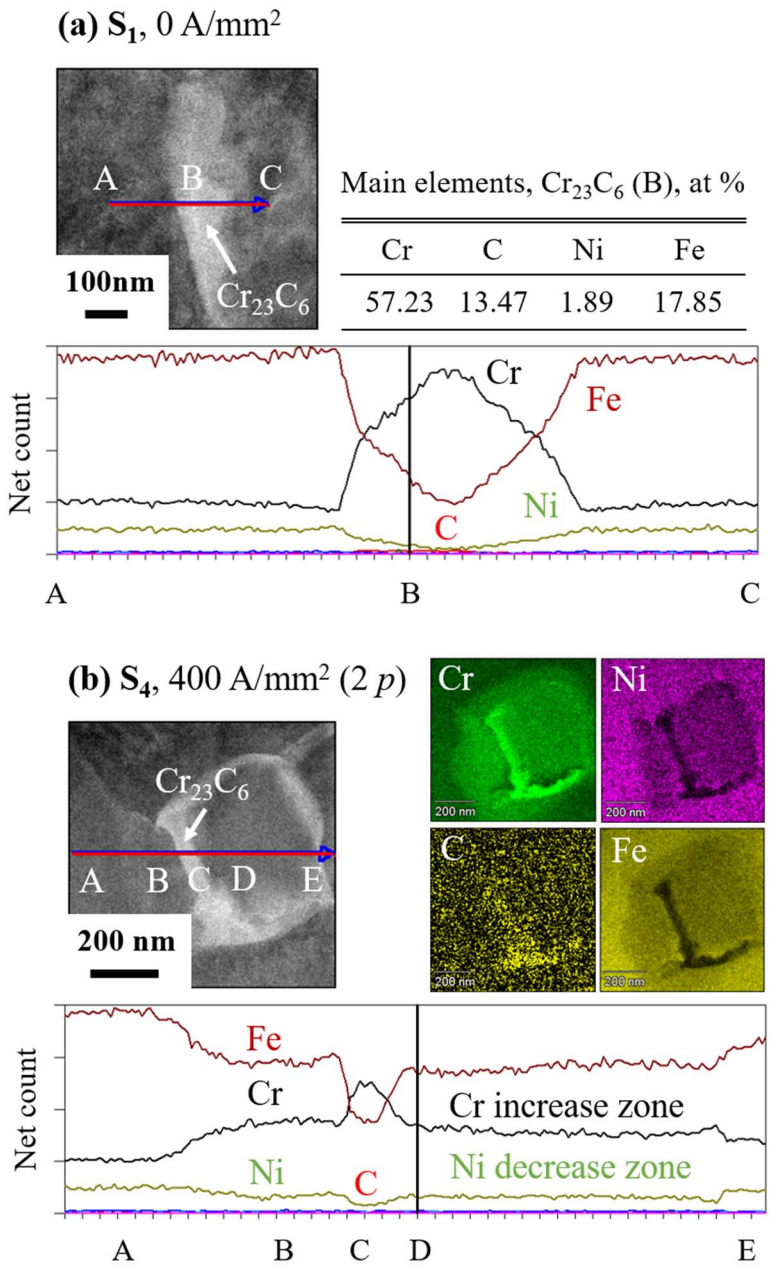

Fig. 4.7 TEM-EDS elemental analysis the interface (CSA view) between LAGBs and $Cr_{23}C_6$, (a) typical elemental distribution of $Cr_{23}C_6$ (S_1) and (b) that changed by $Cr_{23}C_6$ dissolution as the effect of HDPEC (S_4).

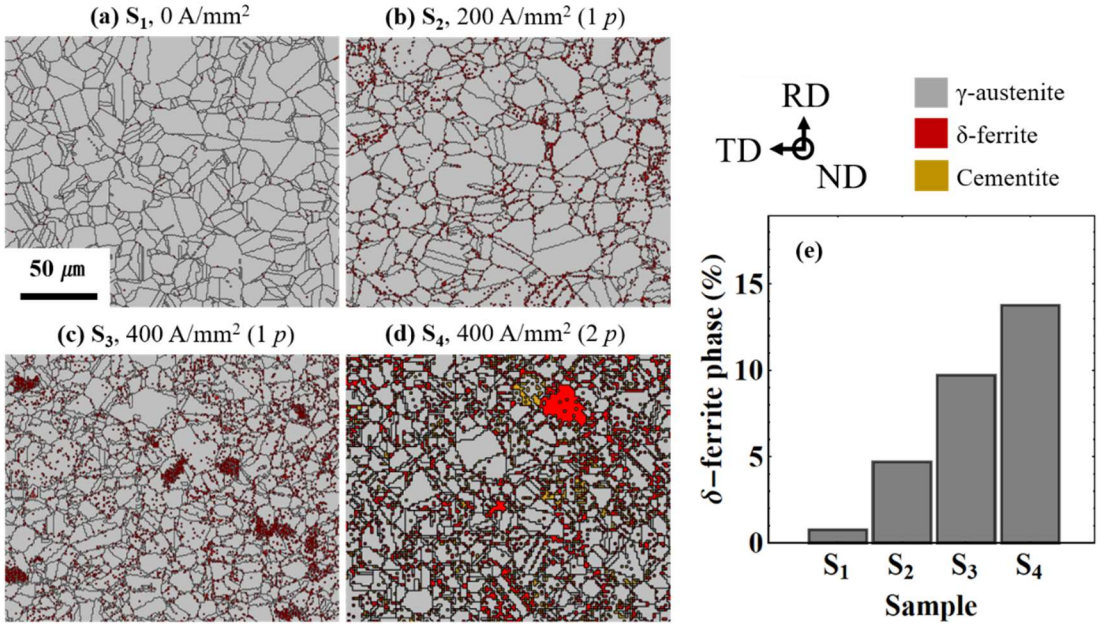

Fig. 4.8 EBSD phase maps for the evolution of δ-ferrite phase, (a-d) S_1, S_2, S_3 and S_4, respectively, and (e) fraction plot of δ-ferrite phase.

In addition, the EBSD phase maps of Fig. 4.8 (a-d) scanned from the dashed squares of Fig. 4.1 (a) show the evolution of δ-ferrite. The fraction of δ increases as the effect of HDPEC increases, namely, 0.77 % for S_1, 4.70 % for S_2, 9.73 % for S_3 and 13.77 % for S_4, respectively. Uniquely, the small amount of cementite phase was revealed in S_4 of Fig. 4.8 (d).

4.4 Discussion

4.4.1 Strengthening mechanism

Fig. 4.9 summarizes the modification process of the material as the effect of HDPEC based on the results of GBCD and elemental analysis. The fraction of ∑ 3 TBs decreased significantly, whereas the increases in LAGBs and HAGBs were revealed (Figs. 4.1-4.4). In general, ∑ 3 TBs have been categorized as low-energy boundaries, as contrasted with high-energy boundaries such as LAGBs and HAGBs [1]. The GB movement from low-

energy ∑ 3 TBs to high-energy HAGBs by the effect of HDPEC could be demonstrated under the control of low-temperature without thermally-activated processes. It could be thought of as the EWF-induced GB refinement. The modification of microstructure could still be available without considering the joule heating effect in the material. The contour of strain fields by pulse effect helps explain the change of GB characteristics from the ∑ 3 TBs to the HAGB (Figs. 4.2 and 4.3). Furthermore, the increased fraction of LAGBs was demonstrated for the grain refinement by dislocation motion since the LAGBs are composed of numerous dislocations. Dislocation motion by EWF participated in creating the subgrains. The increased p of HDPEC mainly contributes to forming new LAGBs. Consequently, the EWF promotes the variation of GBCD as a source of fluctuating force. When the level of HDPEC treatment is higher, the grain refinement becomes stronger, in which the p of HDPEC plays a more important role as presented in this chapter.

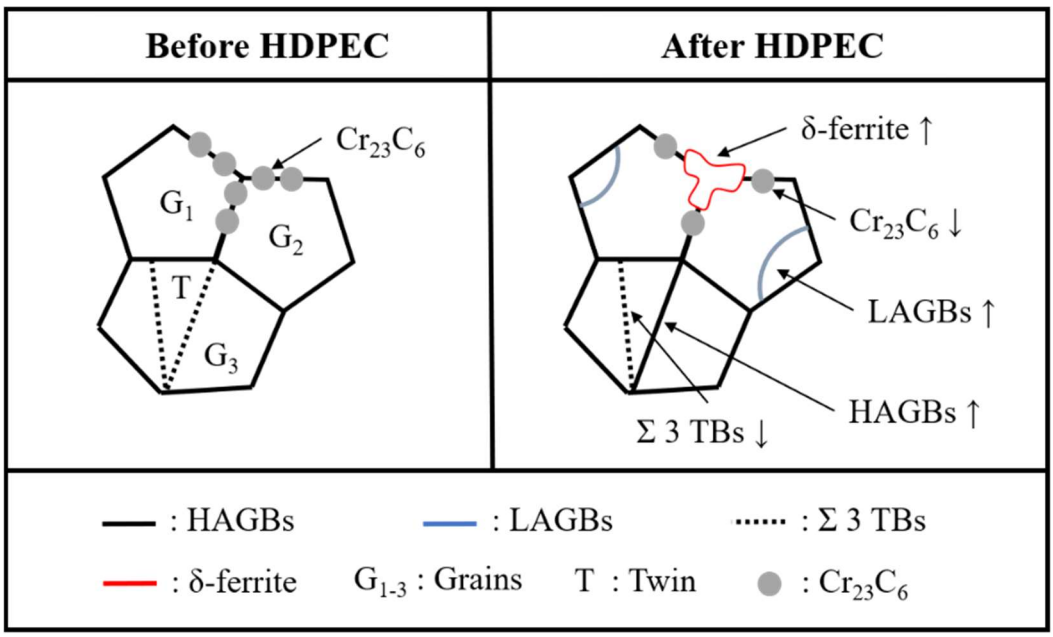

Fig. 4.9 Schematics of the modification process in the grains affected by the HDPEC.

To evaluate the degree of the material strengthening based on the modification of microstructure, the following equations include the Hall-Petch strengthening term with a quantity of δ-ferrite phase in the values of σ_y, which is the so-called Irvine equation [16]. This regression formula has been used to calculate the values of σ_y and σ_u [17-20],

$$\sigma_y = 67.8 + 354.2\ (\mathrm{C}) + 20.0\ (\mathrm{Si}) + 3.7\ (\mathrm{Cr}) + 14.5\ (\mathrm{Mo}) + 2.5\ (\delta) + 7.1\ d^{-1/2}\ , \tag{4.1}$$

$$\sigma_u = 446.6 + 523.6\ (\mathrm{C}) + 41.6\ (\mathrm{Si}) + 2.0\ (\mathrm{Ni}) + 18.5\ (\mathrm{Mo}) + 13.9\ d^{-1/2}\ , \tag{4.2}$$

where the chemical quantities can be substituted by the weight percent. In Eq. (4.1), the amount of δ-ferrite is included, and the amount of δ-ferrite increases in the EBSD phase maps of Fig. 4.8 (a-d) as an effect of HDPEC. Based on the increased amount of δ-ferrite of Fig. 4.8 (e) and the measured grain size, the improvement of σ_y and σ_u can be expected, which agrees well with the stress-strain relationship.

4.4.2 Reduction of $Cr_{23}C_6$

Based on the elemental evolution in iv of Fig. 4.6 (a-c), a process of the dissolution of $Cr_{23}C_6$ could be explained. There have been reports concerning the presence of thermodynamically transformed δ-ferrite between two austenite grains [6,21]. It has been known that the transformation of the phase structure leads to an increase in Cr and a decrease in Ni near GBs [21]. This metallurgical modification could be connected with the process of phase transformation from γ-austenite to δ-ferrite, so-called $Cr_{23}C_6 + \gamma \leftrightarrow$

δ eutectoid reaction. In general, the reaction of $Cr_{23}C_6$ + γ ↔ δ requires a thermally-activated process. On the other hand, the T_R in this study was controlled significantly below the certain temperature associated with the metallurgical process of the material. In addition, locally changed T_R by small line defects due to $Cr_{23}C_6$ can be generally low, thereby it can be assumed that the gap of T_R near line defects by $Cr_{23}C_6$ is negligible because the line defect area per given area is sufficiently small. Thus, the effect of EWF could mainly contribute to the transformation of the phase structure resulting in the dissolution of $Cr_{23}C_6$ and the increase of δ-ferrite near GBs as shown in Figs. 4.6, 4.7 and 4.8. In a recent report, the dissolution of $Cr_{23}C_6$ below the thermodynamic dissolution temperature of the material was achieved through numerous applications of pulsed electric current [22]. Different from the report, our findings show that a few p of HDPEC still play a modification role in the dissolution of $Cr_{23}C_6$. The dissolution process was distinguished between 1 p and 2 p and could be achieved for the modification of the microstructure. Further, the dissolution of $Cr_{23}C_6$ by a few p of HDPEC exhibited the reaction in the form of $Cr_{23}C_6$ + γ ↔ δ. A significant variation in both δ-ferrite and the dissolution of $Cr_{23}C_6$ was demonstrated by the effect of HDPEC without a thermally activated process.

4.4.3 Role of EWF

The role of EWF could be summarized into the following mechanisms in overcoming the strength-ductility trade-off by the effect of HDPEC. An increase in HAGBs and the newly formed LAGBs contribute mainly to the Hall-Petch strengthening by grain refinement. There was a decrease in $\sum 3$ TBs, but it does not lead to a decrease in σ_y and ε_f because the heat-treated material state used in this thesis contains initially a lot of $\sum 3$

TBs (> 40 %). In addition, this is probably expected to have been achieved owing to an increase in strain hardening capacity by a decrease in $Cr_{23}C_6$. Losing ductility by decreasing ∑ 3 TBs could be compensated by the decrease in $Cr_{23}C_6$.

In general, the application of HDPEC inevitably accompanies the increase of ΔT_J. Higher ΔT_J can sometimes promote a decrease of the potential energy barrier to modify the microstructure of materials. The dominant effect of EWF could be assumed under a significantly low ΔT_J. A fluctuating force can be generated by the collective drift electrons, which are caused by the EWF of HDPEC, and can thereby push atoms to activate their dislocation motion. Thus, the EWF contributes mainly to modify the microstructure of the material. The HDPEC of 2 p could better promote both dislocation-activated and δ-ferrite induced strengthening processes than that of 1 p owing to an abrupt increment of voltage.

4.5 Summary

In this chapter, a series of experimental works was performed to clarify the strengthening mechanisms in type 316 austenitic stainless steel. The effect of HDPEC contributes to modifying the GB characteristics that could be explained by the GBCD plot. ∑ 3 TBs lose their misorientation angle resulting in the transformation into HAGBs. In addition, the fraction of LAGBs was increased as an effect of HDPEC. Dislocation motion induced by EWF could result in the accumulation of dislocations around the GBs, thereby forming some new GBs. It could lead to the formation of small grains. This partial grain refinement can decrease the average size of the grain, thus increasing the strength of the material. Both the j and the p of HDPEC contribute to achieving the improvement of σ_y, σ_u and ε_f. The strength-ductility trade-off could be overcome through the HDPEC

conditions used in this chapter.

Two phenomena by elemental kinetics were observed. One is the dissolution of $Cr_{23}C_6$ with a decrease in C, an increase in Cr and a decrease in Ni. The other is the increase in δ-ferrite. The decrease of $Cr_{23}C_6$ and increase of δ-ferrite could be explained by the eutectoid reaction $Cr_{23}C_6 + \gamma \leftrightarrow \delta$. The dissolution of $Cr_{23}C_6$ below the certain temperature of the material was achieved by the proposed conditions of HDPEC. The role of EWF could be explained through the condition of HDPEC. The modification of microstructure by dislocation motion owing to EWF was successfully demonstrated without a thermally activated process. The pulse effect by abruptly increased voltage results in the strengthening of the material.

References

[1] M. Michiuchi, H. Kokawa, Z.J. Wang, Y.S. Sato, K. Sakai, Twin-induced grain boundary engineering for 316 austenitic stainless steel, Acta Materialia. 54 (2006) 5179–5184. https://doi.org/10.1016/j.actamat.2006.06.030.

[2] M. M. Abramova, N. A. Enikeev, R. Z. Valiev, A. Etienne, B. Radiguet, Y. Ivanisenko, X. Sauvage, Grain boundary segregation induced strengthening of an ultrafine-grained austenitic stainless steel, Materials Letters. 136 (2014) 349–352. https://doi.org/10.1016/j.matlet.2014.07.188.

[3] L. Tan, T. R. Allen, J. T. Busby, Grain boundary engineering for structure materials of nuclear reactors, Journal of Nuclear Materials. 441 (2013) 661–666. https://doi.org/10.1016/j.jnucmat.2013.03.050.

[4] S. Sinha, D. I. Kim, E. Fleury, S. Suwas, Effect of grain boundary engineering on the microstructure and mechanical properties of copper containing austenitic stainless steel,

Materials Science and Engineering: A. 626 (2015) 175–185. https://doi.org/10.1016/j.msea.2014.11.053.

[5] R. Jones, V. Randle, Sensitisation behaviour of grain boundary engineered austenitic stainless steel, Materials Science and Engineering: A. 527 (2010) 4275–4280. https://doi.org/10.1016/j.msea.2010.03.058.

[6] A. M. Bettanini, L. Ding, J. D. Mithieux, C. Parrens, H. Idrissi, D. Schryvers, L. Delannay, T. Pardoen, P. J. Jacques, Influence of $M_{23}C_6$ dissolution on the kinetics of ferrite to austenite transformation in Fe-11Cr-0.06C stainless steel, Materials & Design.

[7] D. Waryoba, Z. Islam, B. Wang, A. Haque, Recrystallization mechanisms of Zircaloy-4 alloy annealed by electric current, Journal of Alloys and Compounds. 820 (2020) 153409. https://doi.org/10.1016/j.jallcom.2019.153409.

[8] H. Conrad, Electroplasticity in metals and ceramics. Materials Science and Engineering A. 287 (2000) 276-287. https://doi.org/10.1016/S0921-5093(00)00786-3.

[9] J. Huang, Z. Xu, Y. Deng, L. Peng, Electropulsing-induced α to β phase transformation of Ti–6Al–4V, Journal of Manufacturing Science and Engineering. 141 (2019) 111012. https://doi.org/10.1115/1.4044835.

[10] Z. Islam, H. Gao, A. Haque, Synergy of elastic strain energy and electron wind force on thin-film grain growth at room temperature, Materials Characterization. 152 (2019) 85–93. https://doi.org/10.1016/j.matchar.2019.04.008.

[11] C. Rudolf, R. Goswami, W. Kang, J. Thomas, Effects of electric current on the plastic deformation behavior of pure copper, iron, and titanium, Acta Materialia. 209 (2021) 116776. https://doi.org/10.1016/j.actamat.2021.116776.

[12] Y. Tang, A. Hosoi, Y. Morita, Y. Ju, Restoration of fatigue damage in stainless steel by high-density electric current, International Journal of Fatigue. 56 (2013) 69–74.

https://doi.org/10.1016/j.ijfatigue.2013.08.012.

[13] Y. Tang, A. Hosoi, Y. Iwase, Y. Ju, Effect of high-density electric current on the microstructure and fatigue crack initiation of stainless steel, Materials Transactions. 54 (2013) 2085–2092. https://doi.org/10.2320/matertrans.M2013198.

[14] E. O. Hall, The deformation and ageing of mild steel: III discussion of results. Proceedings of the Physical Society. Section B. 64 (1951) 742-747. https://doi.org/10.1088/0370-1301/64/9/302.

[15] N. J. Petch, The cleavage strength of polycrystals. Journal of the Iron and Steel Institute. 174 (1953) 25-28.

[16] K. J. Irvine, The strength of austenitic stainless steel. Journal of the Iron and Steel Institute. 207 (1969) 1017-1028.

[17] N. Ohkubo, K. Miyakusu, Y. Uematsu, H. Kimura. Effect of alloying elements on the mechanical properties of the stable austenitic stainless steel. ISIJ International. 34 (1994) 764-772. https://doi.org/10.2355/isijinternational.34.764.

[18] K. Kako, E. Kawakami, J. Ohta, M. Mayuzumi, Effects of various alloying elements on tensile properties of high-purity Fe-18Cr-(14-16)Ni alloys at room temperature, Materials Transactions. 43 (2002) 155–162. https://doi.org/10.2320/matertrans.43.155.

[19] A. J. Cooper, W. J. Brayshaw, A. H. Sherry, Tensile fracture behavior of 316L austenitic stainless steel manufactured by hot isostatic pressing, Metallurgical and Materials Transactions A. 49 (2018) 1579–1591. https://doi.org/10.1007/s11661-018-4518-2.

[20] R. Singh, S. Agrahari, S. D. Yadav, A. Kumar, Microstructural evolution and mechanical properties of 316 austenitic stainless steel by CGP, Materials Science and

Engineering: A. 812 (2021) 141105. https://doi.org/10.1016/j.msea.2021.141105.

[21] C. C. Tseng, Y. Shen, S. W. Thompson, M. C. Mataya, G. Krauss, Fracture and the formation of sigma phase, $M_{23}C_6$, and austenite from delta-ferrite in an AISI 304L stainless steel, Metallurgical and Materials Transactions A. 25 (1994) 1147-1158. https://doi.org/10.1007/BF02652290.

[22] X. Liu, X. Zhang, An ultrafast performance regeneration of aged stainless steel by pulsed electric current, Scripta Materialia. 153 (2018) 86-89. https://doi.org/10.1016/j.scriptamat.2018.05.004.

Chapter 5 Low-cycle fatigue behavior improved by HDPECs

In this chapter, the improvement of LCF properties by multiple applications of HDPEC was experimentally demonstrated. The effect of HDPEC in the material damaged by fatigue loading due to repetitive structural responses is different compared with that by tensile loading. Especially, the high loading amplitude in the LCF regime accompanies higher deformation, which can significantly generate dislocation networks, than that of HCF. In the point of view of multiple applications of HDPEC and its application timing, this chapter proposes an effective way to improve the LCF properties of the material. Microstructural evidence such as ductile striation and welded area is provided. The annihilation of dislocations owing to the effect of EWF by multiple HDPECs can make the material ductile after getting brittleness due to the accumulation of dislocations by fatigue loading. It has been written based on the following published article: Improvement of low-cycle fatigue life of austenitic stainless steel by multiple high-density pulsed electric currents, International Journal of Fatigue. 106639 (2021). It has been confirmed supported journal policy that, as one of the authors for this article, I retain the right to include it in a thesis or dissertation, if it is not provided commercially.

5.1 Introduction

In many industrial sites, the mechanical components are frequently exposed to repetitively high ε_a that can fail by the low N. To assess the fatigue properties of materials under high ε_a, the LCF approach is more favorable compared to the HCF approach [1,2].

Many scientists have attempted to set improved fatigue properties in a variety of

materials. For instance, the fatigue properties of carburized austenitic stainless steel were improved by making the discontinuity of surface crack initiation. The carburized material layer leads to tiny surface cracks that precede the initiation of large ductile cracks in the base material. It gives supplementary fatigue lives under any circumstance such as stress level and environmental conditions [3]. Austenitic stainless steel manufactured by 3D printing has an improved fatigue limit than the material state as rolled owing to modified microstructures [4]. The improved surface hardness and fatigue strength in the nitride material were achieved by fine particle peening [5]. In these ways, most modification techniques have been developed based on mechanical and chemical methods [6].

Over the past decades, the application of HDPEC has been considered a promising method for the improvement of the fatigue properties in metals [7–13]. So far, it has been employed for stainless steel [7,8], high-strength steel [9], drawing quality steel [10], polycrystalline copper [11] and aluminum alloy [12]. The electric current could make microstructural changes such as the dislocation motion, grain size and phase structure [8,13–15] based on the presence of the induced EWF and Joule heating [16] as introduced in chapter 1. Although the light has been shed on pertinent mechanisms, improvement in the methodology for the electric current application and its influence on the fatigue properties have not yet been sufficiently addressed. Assessments in methodology are required to determine how this treatment can be properly applied and how much fatigue life can efficiently be improved under given circumstances.

In this chapter, the effects of multiple HDPECs were demonstrated based on a series of LCF tests. FCG tests were first conducted to determine the favorable j. LCF tests under strain control approach were performed to assess the LCF life changed by the p of HDPEC and its application timing. The properties of LCF were evaluated using classical

fatigue models. The BMC and Smith-Watson-Topper (SWT) mean stress models were relevantly used [1,17]. Microstructures in fracture surfaces presented by LCF loading were examined using FESEM. Microstructural variations in fatigue fracture surfaces were determinatively correlated with the improvement of LCF life as the effect of multiple HDPECs.

5.2 Application methods of HDPEC for fatigue tests

In Fig. 5.1, applying the methods and application timing for the multiple HDPECs are shown. The details in the conditions of multiple HDPECs and the fatigue tests are correspondingly listed in Table 5.1. t_{d} for each pulse application was applied samely as 5 ms in the treated groups by HDPEC. In the FCG tests (groups I-IV), the group I denotes for the sample without HDPEC, and groups II, III and IV denote the samples with multiple applications of HDPEC under the j of 100, 150 and 200 A/mm^2, respectively. The initial application of multiple HDPECs for groups II, III and IV was investigated after a pre-crack was made. Multiple HDPECs with a cycle pitch N_{p} were further applied.

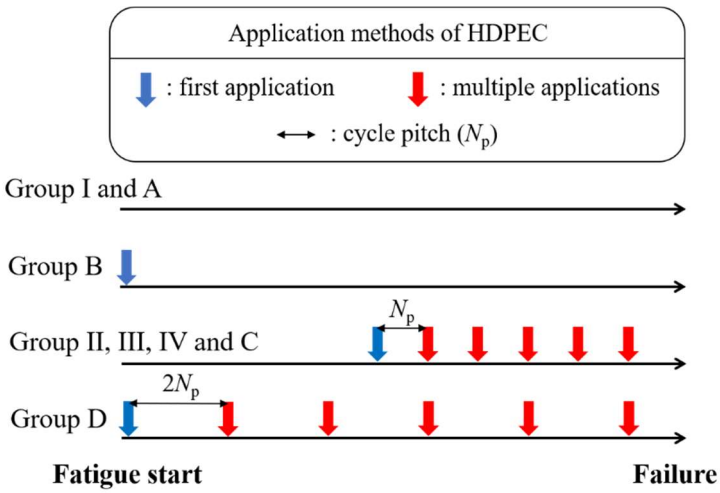

Fig. 5.1 Schematics of the application methods of multiple HDPECs for fatigue tests.

In the LCF tests, group A is denoted as the case without HDPEC, and the groups with multiple HDPECs are consist of three types. Group B was applied with a single pulse before the fatigue test is started. Group C was treated with a single pulse at every N_{p} after the fatigue cycles reach the half-life of group A. Group D was applied with a single pulse before the fatigue test and at every cycle of $2N_{\mathrm{p}}$ through the entire fatigue period. The p of multiple HDPECs in groups C and D was investigated to be equal.

Table 5.1 Conditions of multiple HDPECs related to FCG and LCF tests.

Test group		Density (j), A/mm^2	Duration time (t_{d}), ms	Application methods	Applied number (p), times	Strain ratio (R)	Strain amplitude (ε_a)
FCG	I	-	-	-	-	0.5	0.00275
	II	100	5	After fatigue pre-crack	3		
	III	150	5		4		
	IV	200	5		5		
LCF	A	-	-	-	-	0.5	0.00175–0.00375
						–1	
	B	200	5	Single pulse before fatigue	1	0.5	
						–1	
	C	200	5	During crack propagation	2–17	0.5	
						–1	
	D	200	5	Over the entire period	2–15	0.5	
						–1	

The N_{p} was pre-determined as 2000 cycles based on the accessible p of multiple HDPECs in the predicted LCF life. The p of multiple HDPECs was considered as less than or equal to 17 under the lowest ε_a. The groups I–IV in FCG tests were precedently performed to decide a favorable j of multiple HDPECs between 0 and 200 A/mm^2 under $\varepsilon_a = \varepsilon_{\max} - \varepsilon_{\min} = 0.00275$ and $R = \varepsilon_{\min}/\varepsilon_{\max} = 0.5$. Based on a specified j determined by the FCG tests, the LCF tests (groups A–D) were conducted to valorize the failure cycles from the variation of the p of multiple HDPECs and its application manner. The applied ε_a was assumed as $\varepsilon_a = \Delta\varepsilon$ for the LCF tests of $R = 0.5$ and as $\varepsilon_a = \Delta\varepsilon/2$ for the LCF tests of $R = -1$.

5.3 Results

5.3.1 Fatigue crack growth behavior

Fatigue pre-cracks near the notch were made by mode I fatigue loading into the direction perpendicular to the loading. Figure 5.2 (a) depicts the a versus N, where the red arrows indicate the application timing of multiple HDPECs. The results in groups II-IV showed that the applied multiple HDPECs could contribute to the delay of FCG compared to the result in group I. The delay effect is temporal because FCG behavior returned to the original state after several hundred or thousand cycles, i.e., the effectiveness remains a different duration which depends on the condition of HDPEC. The degree of delay in FCG curves depends obviously on the increased j. As a result, the delay effect was best when the j was 200 A/mm^2, while the efficiency was less when it was 100 A/mm^2. The j of 150 A/mm^2 depicted an equivalent but slightly low efficiency compared to that of 200 A/mm^2. To evaluate FCG behavior in LCF analysis, the strain intensity factor has been broadly employed. Here, an evaluation of FCG was performed based on Eq. (1.8) as

introduced in chapter 1. Where f_c in Eq. (1.8) was applied as a constant set to 1. Figure 5.2 (b) depicts the relationship between da/dN and ΔK_ε. The data-fitting in Fig. 5.2 (b) was obtained from the da/dN data-set of group I (0 A/mm^2), i.e., the Paris' law $da/dN \propto \Delta K_\varepsilon{}^{2.67}$. The results in groups II-IV showed that multiple applications of HDPEC contributed to an overall reduction of da/dN compared to group I (0 A/mm^2). This effect in groups III and IV was generally more prominent than that in group II, i.e., higher j such as 150 and 200 A/mm^2 played a more important role in the resistance of FCG. On the other hand, too high or too low applications of HDPEC, which depends on the material properties, would result in less efficiency in the improvement of fatigue properties [12]. Thus, we choose one j condition as 200 A/mm^2 to perform the LCF tests.

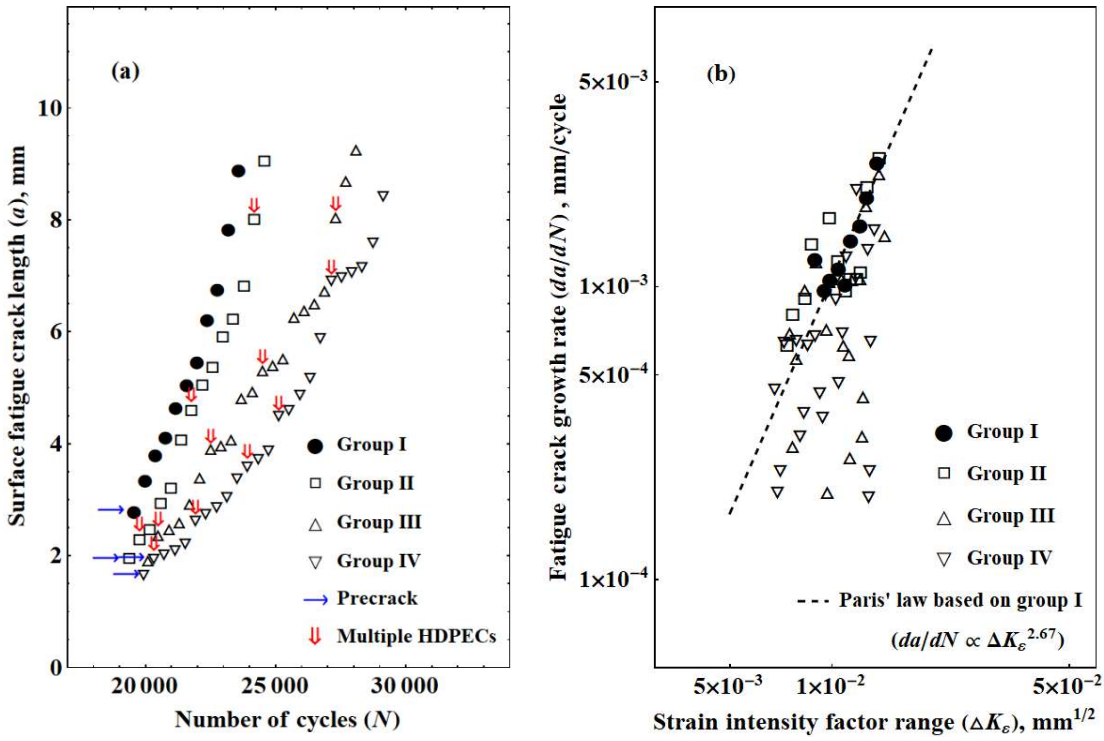

Fig. 5.2 Effect of multiple applications of HDPEC presented by FCG testing, (a) surface fatigue crack length as a function of the number of fatigue cycles and (b) FCG rate as a function of the strain intensity factor range.

5.3.2 Low-cycle fatigue properties

As commonly employed in fatigue analysis for LCF behavior, the strain-life concept was used to assess the LCF properties resulting from multiple HDPECs [1].

In Fig. 5.3, the experimented LCF data-sets under $R = 0.5$ indicate how much the concerned application methods contribute to the improvement of LCF life. The degree of increased LCF life for group C is better than that of group D under the same p of HDPEC. The application method of group B results in a slightly increased LCF life. The inset figure of Fig. 5.3 shows the enhancement of mean increased ratios (%) in LCF life. Not only for groups C (94 %) and D (55 %) were improved but also a lesser extent for group B (19 %) was also achieved. Where the percentage ratios (%) were calculated based on the fatigue life N_f, (N_f in groups B, C and D – N_f in group A)/ (N_f in group A) × 100.

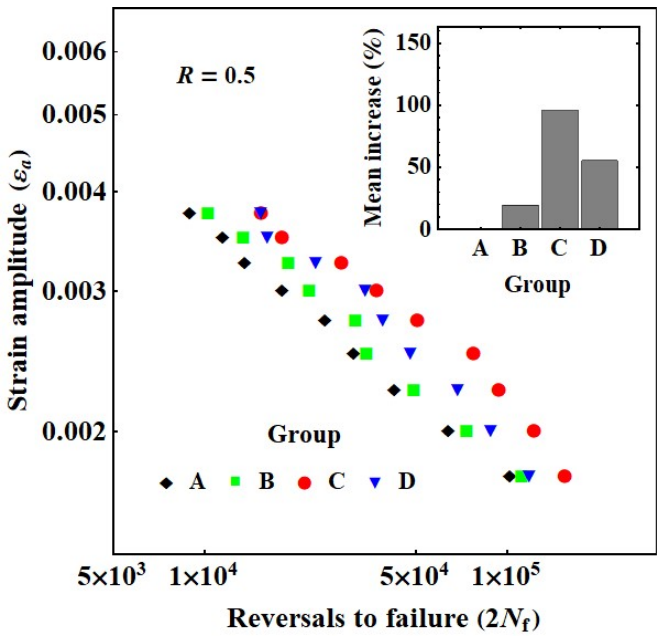

Fig. 5.3 Strain-life curves under $R = 0.5$ by the application methods of HDPEC. Inset: mean increased ratios (%) based on LCF life of groups B, C and D compared with untreated group A.

In the range between $\varepsilon_a = 0.002$ and $\varepsilon_a = 0.003$, the LCF life was noticeably improved in group C compared to that of group D. It implies that the multiple applications of HDPEC are much more efficient during the crack propagation than during the crack initiation. Nonetheless, the effect of group B could not be negligible since the HDPEC application before starting fatigue slightly contributed to improving the LCF life at a relatively high ε_a. The application method of group D could also improve the LCF life in the range of ε_a between 0.003 and 0.00375 as much as improved LCF life of group C.

In usual fatigue analysis for $R = 0.5$, the mean stress effect can be considered as a significant factor due to the existence of non-zero stress between $\sigma_{\max}$ and $\sigma_{\min}$ by asymmetric fatigue loading [1]. To further evaluate the improved LCF life presented in Fig. 5.3, it is mandatory to be examined for the fatigue results at $R = -1$. Therefore, additional series of LCF tests at $R = -1$ were performed in the same range of ε_a as those for $R = 0.5$. As a prediction theory, the SWT mean stress model [1,17,23] was used to comprehensively compensate for the LCF results affected by mean stress. Since the SWT model requires the fitting values of material constants determined by the elastic and plastic components, the classical BMC model was employed to decide the fitting values with the experimented LCF data at $R = -1$. To describe the LCF curves based on the experimental data-sets of ε_a and the $2N_{\mathrm{f}}$, the Eq. (1.9) of chapter 1 can be practically used [1].

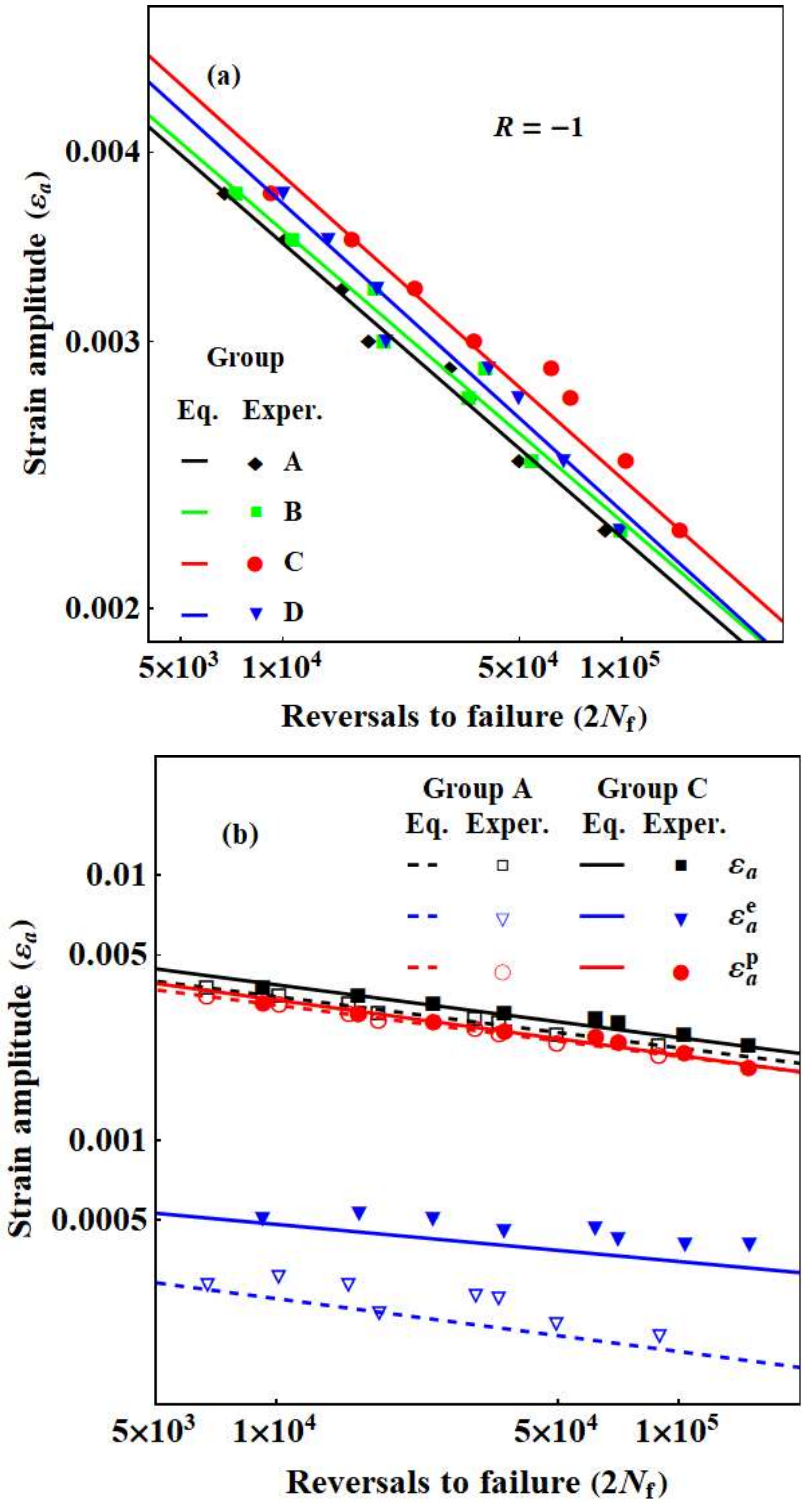

Fig. 5.4 LCF properties for $R = -1$, (a) strain-life curves and (b) decomposition of elastic and plastic terms in groups A and C.

Table 5.2 Determined material constants using the BMC equation.

Group	b	c	σ'_{f}	$\varepsilon'_{\mathrm{f}}$
A	–0.1998	–0.1936	354.79	0.0220
B	–0.1987	–0.1915	361.37	0.0219
C	–0.1402	–0.2087	375.06	0.0267
D	–0.2007	–0.2029	398.40	0.0255

Figure 5.4 (a) shows the experimented LCF results of ε_a as a function of $2N_{\mathrm{f}}$ at $R = -1$ together with the fitting lines that are plotted using the listed values b, c, σ'_{f} and $\varepsilon'_{\mathrm{f}}$ in Table 5.2. A comparable tendency with the results at $R = 0.5$ presented in Fig. 5.3 was depicted in terms of the improvement of LCF life. The application method of group C could also be deemed the best treatment way. Figure 5.4 (b) displays the relationship among the ε_a, $\varepsilon_a^{\mathrm{e}}$ and $\varepsilon_a^{\mathrm{p}}$ versus $2N_{\mathrm{f}}$. It was practically deduced based on the proportional decomposition of $\varepsilon_a^{\mathrm{e}}$ and $\varepsilon_a^{\mathrm{p}}$ at the half-life [1]. The LCF results in groups A and C were selectively plotted. The dominance of $\varepsilon_a^{\mathrm{p}}$ component was demonstrated for both groups A and C. This kind of predominance has been known as the LCF property of the material [18–20].

By using the determined material constants listed in Table 5.2, the strain-life curves of Fig. 5.3 can be modified using the following SWT model [1,17,23],

$$\sigma_{\max}\varepsilon_a = \frac{(\sigma'_{\mathrm{f}})^2}{E}(2N_{\mathrm{f}})^{2\mathrm{b}} + \sigma'_{\mathrm{f}}\varepsilon'_{\mathrm{f}}\,(2N_{\mathrm{f}})^{\mathrm{b+c}}, \tag{5.1}$$

where $\sigma_{\max}$ is the summation of the σ_a and the mean stress. It is measured at half-life in

each ε_a. The SWT parameter $\sigma_{\max}\varepsilon_{\mathrm{a}}$ in left term of Eq. (5.1) can be considered as the compensation of non-zero mean stress presented for $R = 0.5$, which can measure the degree of LCF life. By the substitution of the material constants (b, c, σ_{f}' and $\varepsilon_{\mathrm{f}}'$ in Table 5.2) at $R = -1$, equation (5.1) can provide the prediction of the LCF life presented at $R = 0.5$. The $\sigma_{\max}\varepsilon_a$ versus of $2N_{\mathrm{f}}$ is plotted in Fig. 5.5 using the LCF data-set presented in Fig. 5.3 and SWT mean stress model. Because the mean stress compensation depends on the values of $\sigma_{\max}$, group C could be regarded to be the most effective treatment. A comparison between the experimental life and predicted life based on the SWT model is illustrated in Fig. 5.6. The comparison plot displays an agreement within the twice scattering error band.

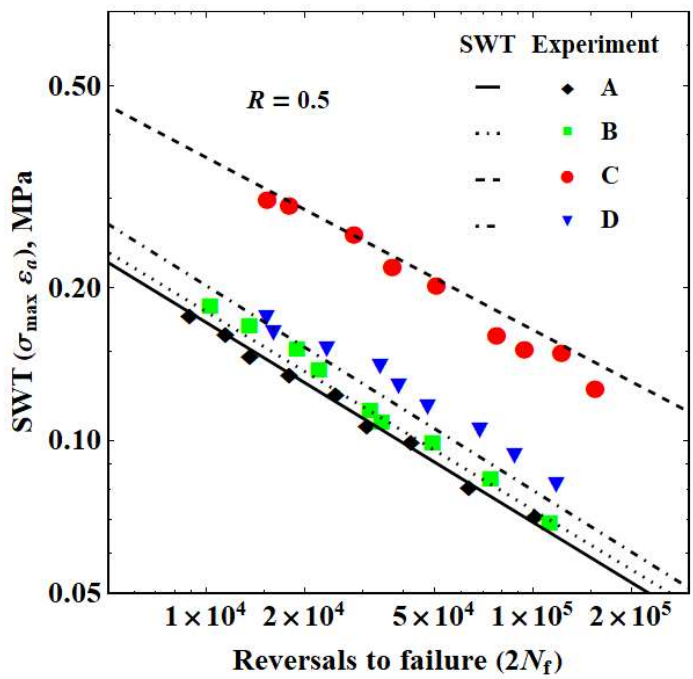

Fig. 5.5 SWT mean stress parameter as a function of reversals to failure based on the experimental and predicted results.

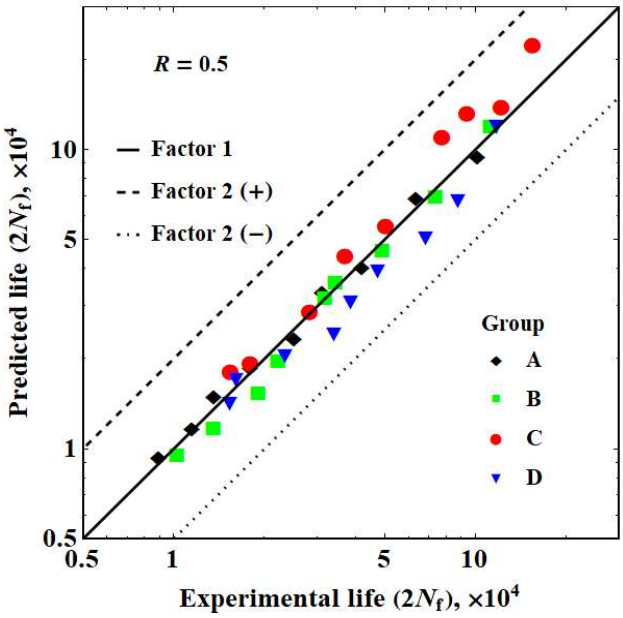

Fig. 5.6 Comparison between the experimental and predicted LCF life.

Figure 5.7 (a) depicts the increased LCF life as a function of ε_a based on the LCF results of $R = 0.5$. In group C, the increased LCF life noticeably reached a peak at $\varepsilon_a = 0.0025$. Then it followed by a gradual decrease with a decrement in ε_a. It implies that the over-application of multiple HDPECs would not guarantee better effectiveness for the improvement of LCF life. A similar tendency could be observed in group D, on the other hand, the result in group B did not significantly depend on the level of ε_a. It is believed that the main mechanism is correlated with the deformation behavior of the material at the crack tip [7]. Applying multiple HDPECs plays also an important role in the synergetic effect with the main mechanism. In Fig. 5.7 (b), a comparison of groups C and D was presented. The plotted data sets were distinguished based on the increased fatigue cycles N_{I} and N_{f} versus the p of multiple HDPECs and the corresponding ε_a. The results in N_{I} depends incrementally on the p of multiple HDPECs and ε_a (the p of HDPEC depends on the ε_a). N_{I} of group C as a function of ε_a at $R = 0.5$ and $R = -1$ is illustrated in the inset figure of Fig. 5.7 (b). The results in N_{I} correspondingly increased regardless of R

values. It means that the effect of multiple HDPECs did not be sensitive to the R values.

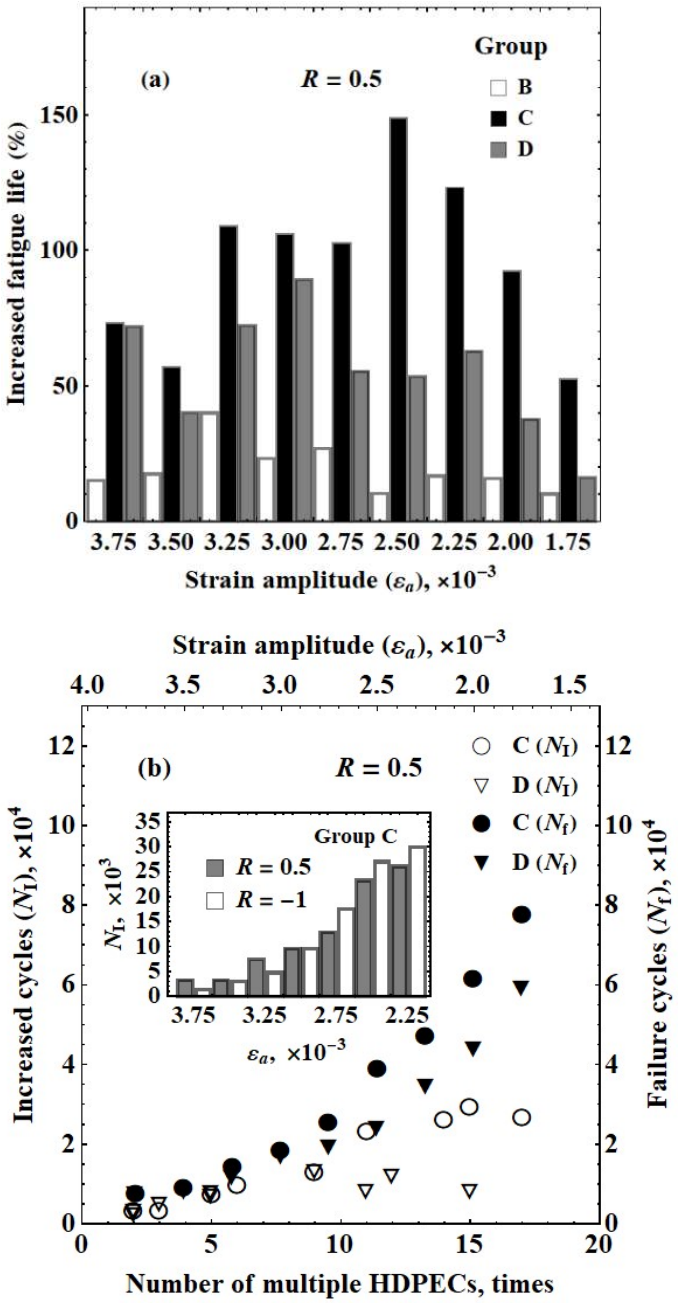

Fig. 5.7 Comparison for improvement of LCF life, (a) ratios of increased fatigue life as a function of the strain amplitude (groups B, C, and D) and (b) increased and failure fatigue cycles versus the applied strain amplitude and the number of multiple HDPECs, respectively. Inset: increased fatigue cycles of group C as a function of the strain amplitudes for $R = 0.5$ and $R = -1$.

5.3.3 Fractography

Microstructural aspects were examined using FESEM to comprehensively explain the LCF results since the fractography induced by fatigue damage can provide understandable evidence generated by fatigue damage. The fracture surfaces obtained under the fatigue conditions of $R = 0.5$ and $\varepsilon_a = 0.002$ were observed because the corresponding crack paths did not friction owing to the asymmetric fatigue loading. Period lengths of the striations l_s were measured to be compared with the results of da/dN.

Figure 5.8 (a–h) depicts the FESEM images of the fracture surfaces traced along the fatigue crack paths in the samples of groups A and C. The entire fracture surfaces, shown in Fig. 5.8 (a) and (b), were obtained through an assemblage of consecutively captured FESEM images. Symbols $p_0 - p_9$ in Fig. 5.8 (b) indicate the applied positions of multiple HDPECs which are the locations affected by multiple HDPECs, and the locations $o_0 - o_9$ in Fig. 5.8 (a) depict the corresponding locations of the sample without the effect of multiple HDPECs. Locations $o_0 - o_9$ were decided based on the locations $p_0 - p_9$. Enlarged FESEM images are shown in Fig. 5.8 (c–h), which are obtained by the high magnification of locations shown in Fig. 5.8 (a) and (b). In Fig. 5.8 (b), crack initiation was given by fatigue loading without the application of multiple HDPECs, and the first application of HDPEC was performed when the N reached at the half-life of N_f in the sample without the application of multiple HDPECs. Its location denotes p_1.

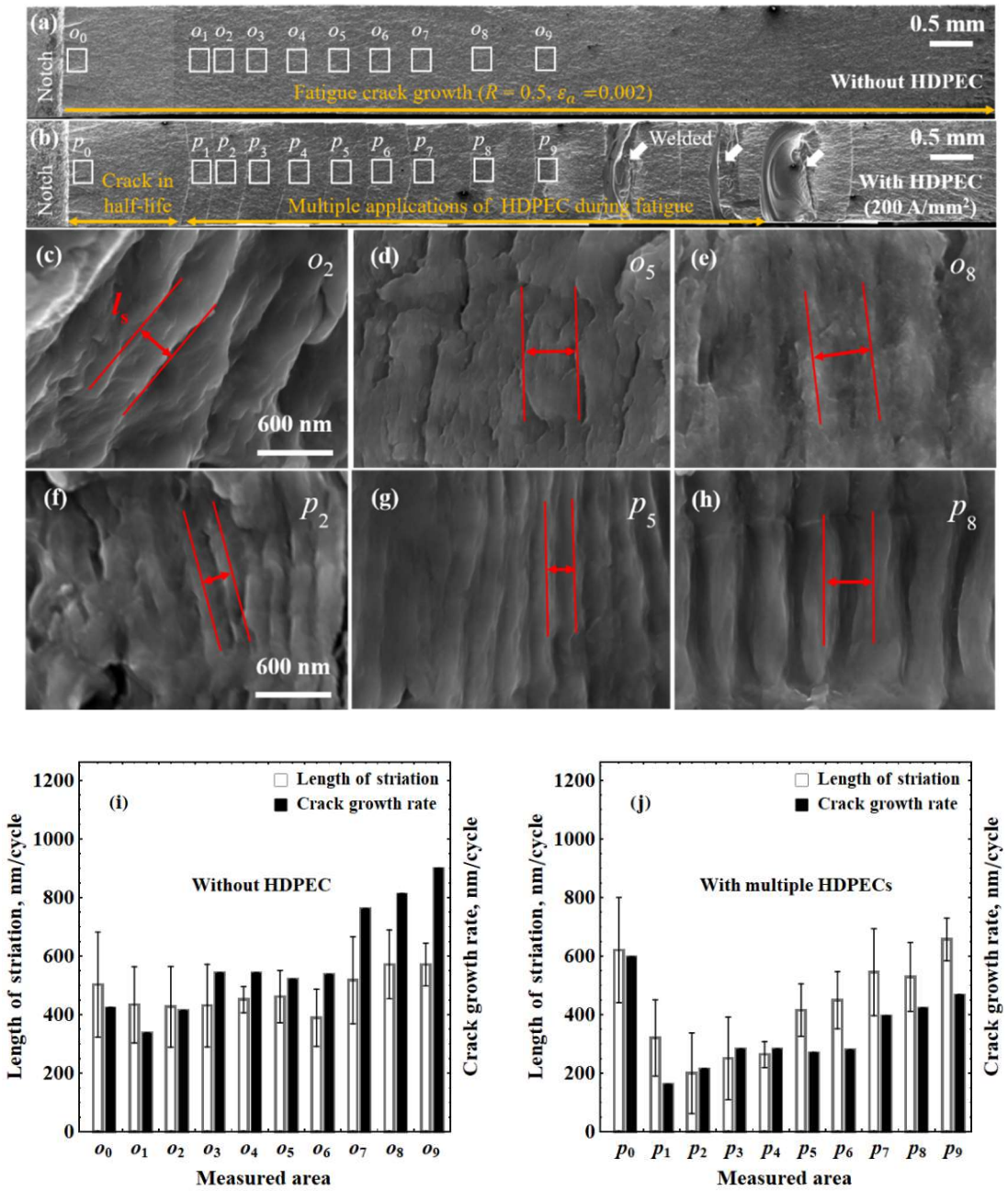

Fig. 5.8 Microstructural evolution of the period lengths of striations as the effect of multiple HDPECs ($R = 0.5$ and $\varepsilon_a = 0.002$), (a) entire fracture surfaces for group A and (b) that for group C, (c–e) obtained ductile striation of locations o_2, o_5 and o_8 (without HDPEC), (f–h) those for p_2, p_5 and p_8 (two, five and eight pulses, respectively), (i) measured mean lengths of striations and FCG rate for the locations of group A and (j) those for group C.

Figure 5.8 (f–h) displays the varied striations as the effect of multiple HDPECs. Compared with l_s of o_2, o_5 and o_8 (Fig. 5.8 (c–e)), l_s of p_2, p_5 and p_8 were noticeably reduced. On the other hand, the depth of striations seemed like be increased. Since the effect of HDPEC could be regarded most pronounced in the regions before half-crack, the differences of l_s between p_2 and p_5 were more compared to l_s between o_2 and o_5. Generally, the spaces of ductile striation like l_s varies on a basis of cycle-by-cycle [24–26], i.e., the spaces of striation are dependent on the level of FCG based on each cycle. Moreover, fractography presented by asymmetric fatigue loading such as $R = 0.5$ provides a clear observation of a cycle-by-cycle morphology than that at $R = -1$ [27]. Under the assumption, a series of l_s was measured to understand the effect of multiple applications of HDPEC. In Fig. 5.8 (I and j), the measured evolutions of l_s and da/dN are depicted in the unit of nm/cycle. A series of l_s plotted in Fig. 5.8 (j) is shorter than those plotted in Fig. 5.8 (i). Both l_s and da/dN show mostly falling within error bars. The results of multiple HDPECs present a certain non-linear evolution. The l_s of p_1–p_5 in Fig. 5.8 (j) was significantly reduced as well as that of p_6–p_9 displays a slight decrement compared with o_0–o_9 in Fig. 5.8 (i). It could improve the LCF properties as the effect of multiple HDPECs.

5.3.4 Pitch effect

The applied method of group C was deemed to be more effective than that of group D. It is found in both cases of $R = 0.5$ and $R = -1$ as shown in Figs. 5.3 and 5.4 (a). Nonetheless, the N_p in group D was applied twice compared with that of group C because the same number of multiple HDPECs was assumed. Thus, supplementary LCF tests were performed to verify whether N_p affects the results in the determination of LCF life. Figure

5.9 displays the N_f versus five $N_p$values (ranges between 1000 and 5000 cycles) with the error bars. The level of ε_a remain unique as $\varepsilon_a = 0.0025$ for both $R = 0.5$ and $R = -1$ with the same application method as that investigated for group C. Therefore, the first HDPEC was applied at the half-life in group A, i.e., 7000 cycles for $R = 0.5$, and 12000 cycles for $R = -1$. Eight pulses were subjected to each case of N_p. As a result, results of N_f by different N_p was barely notable both $R = 0.5$ and -1. It suggests that the application of multiple HDPECs during the period of crack propagation presented more effective than that during crack initiation, thereby the effect of N_p could be regarded negligible.

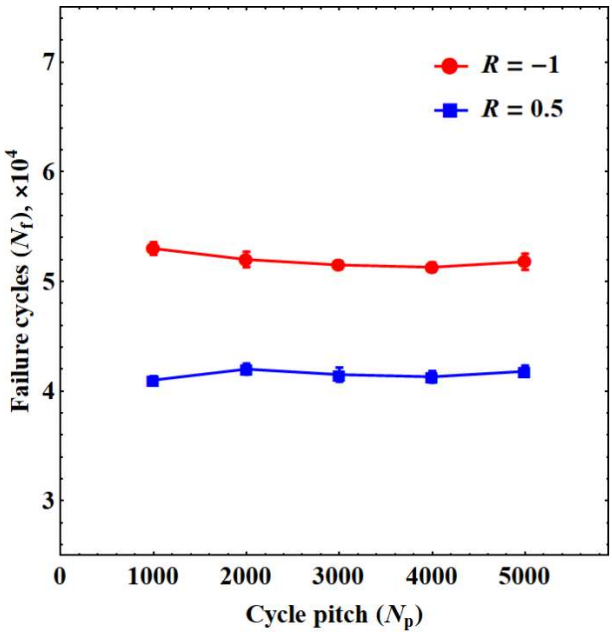

Fig. 5.9 LCF life versus the cycle pitch under $\varepsilon_a = 0.0025$ at $R = 0.5$ and $R = -1$. Where N_p of group C: 2000, N_p of group D: 4000.

5.4. Discussion

5.4.1 Delay in fatigue crack growth

Distinguished fracture surfaces along with the crack paths, which were presented during fatigue, could be observed using FESEM. Ductile striations are generally microstructural indicators that can measure the level of ductility. An increase in ductility can make striations thin and deep [28]. In this chapter, the effect of multiple HDPECs contributed to an increase in the depth of striations as well as a decrease in the l_s, which results in more clear morphologies of ductile striation bands than samples without the application of HDPEC. An increase in N_d in Eq. (1.10) of chapter 1 would be presented when stainless steels experience fatigue damage [29–32]. By contrast, the application of HDPEC could make an annihilation of dislocations [8,13]. Therefore, a decrement of N_d after the application of HDPEC would increase the ductility owing to the annihilation of dislocations. It could result in morphological evidence through an increase in the depth of striations as well as a decrease in the l_s. Different fatigue fracture patterns by the application of multiple HDPECs could contribute to the fluctuation of crack paths. It consequently led to the delay effect of the FCG to improve the LCF life. Further, the change in microstructure such as the formation of small grains and dissolution of $Cr_{23}C_6$, which is shown in chapter 4, made it possible to simultaneously increase the strength and ductility of the material. The formation of small grains can be achieved owing to dislocation motion, thereby improving fatigue performance. Change in phase structure by the dissolution of $Cr_{23}C_6$ is also acknowledged for the formation of small grains.

5.4.2 Effectiveness of multiple HDPECs

The improved LCF life could successfully be achieved with multiple applications of

HDPEC under the investigated application method. One of the important factors is the p of applied HDPEC. It would be noticeably verified that a smaller ε_a can lead to a higher N_{f}, thereby more p of HDPEC are feasible to be applied for the improvement of the LCF life. The degree of improved LCF life showed similarly both $R = 0.5$ and $R = -1$. By contrast, the continuing improvement of the LCF life by increasing the p of multiple HDPECs could not guarantee due to a non-linearity of the HDPEC effects. Further, the efficiency of the improved LCF life is dependent on the application timing and methods. Even though the LCF life was entirely increased by the application of multiple HDPECs during crack initiation and crack propagation (group D), the application during the period of crack propagation (group C) was more effective under the application method based on the same number of HDPECs. Thus, it can be better to apply multiple HDPEC at the crack propagation stage than during crack initiation under the same p of multiple HDPECs.

5.5. Summary

In this chapter, the effects of multiple HDPECs and their application manner were investigated. The improvement of the LCF life in the material was successfully achieved. Based on the presented results, the following issues can be summarized. First, the j of 200 A/mm^2 with multiple applications of HDPEC was regarded as the appropriate j. It is verified based on the FCG test. The delay effect in FCG could be demonstrated as the effect of multiple HDPECs, in which each application could contribute to decreasing da/dN. Second, the p of multiple HDPECs is crucial for the improvement of the LCF life. On the other hand, it could not guarantee a continuous increase in LCF life. Increasing the p of multiple HDPECs could lead to high effectiveness in the improvement

of the LCF life, however, too many applications of HDPECs lead to reducing their efficiency. The N_{p} in multiple applications of HDPEC could not affect the LCF life. Third, controlling the application timing during the crack propagation stage is a better approach than that at the period of crack initiation for the improvement of LCF life within the same p of HDPECs. The application way before the fatigue loading resulted in a slight improvement in LCF life. Nevertheless, all investigated methods give the improvement of LCF life. Finally, more strong ductile striations in the fatigue fracture surface were observed than those without HDPEC as the effect of multiple HDPECs. An increase in the depth and a decrease in the l_{s} of ductile striations were shown owing to multiple applications of HDPEC. The effect of multiple HDPECs contributed to decreasing the N_{d}, then the degree of ductility could be increased, thereby increasing the LCF life.

References

[1] R. I. Stephens, A. Fatemi, R. R. Stephens and H. O. Fuchs: *Metal fatigue in engineering*, (John Wiley & Sons, New York, 2000).

[2] M. F. McGuire: *Stainless steels for design engineers*, (ASM International, Ohio, 2008).

[3] K. Tokaji, K. Kohyama, M. Akita, Fatigue behaviour and fracture mechanism of a 316 stainless steel hardened by carburizing, International Journal of Fatigue. 26 (2004) 543–551. https://doi.org/10.1016/j.ijfatigue.2003.08.024.

[4] Y. Cao, Z. Moumni, J. Zhu, Y. Zhang, Y. You, W. Zhang, Comparative investigation of the fatigue limit of additive-manufactured and rolled 316 steel based on self-heating approach, Engineering Fracture Mechanics. 223 (2020) 106746. https://doi.org/10.1016/j.engfracmech.2019.106746.

[5] S. Kikuchi, Y. Nakahara, J. Komotori, Fatigue properties of gas nitrided austenitic

stainless steel pre-treated with fine particle peening, International Journal of Fatigue. 32 (2010) 403–410. https://doi.org/10.1016/j.ijfatigue.2009.07.019.

[6] M. Sticchi, D. Schnubel, N. Kashaev, N. Huber, Review of residual stress modification techniques for extending the fatigue life of metallic aircraft components, Applied Mechanics Reviews. 67 (2014) 010801. https://doi.org/10.1115/1.4028160.

[7] A. Hosoi, T. Nagahama, Y. Ju, Fatigue crack healing by a controlled high density electric current field. Materials Science and Engineering: A. 533 (2012) 38–42. https://doi.org/10.1016/j.msea.2011.11.024.

[8] Y. Tang, A. Hosoi, Y. Morita, Y. Ju, Restoration of fatigue damage in stainless steel by high-density electric current, International Journal of Fatigue. 56 (2013) 69–74. http://dx.doi.org/10.1016/j.ijfatigue.2013.08.012.

[9] D. Ben, H. Yang, Y. Ma, Q. Wang, Y. Tian, P. Zhang, Declined fatigue crack propagation rate of a high-strength steel by electropulsing treatment, Advanced Engineering Materials. 21 (2019) 1801345. https://doi.org/10.1002/adem.201801345.

[10] A. Kumar A, S. K. Paul, Healing of fatigue crack in steel with the application of pulsed electric current, Materialia. 14 (2020) 100906. https://doi.org/10.1016/j.mtla.2020.100906.

[11] H. Conrad, J. White, W. D. Cao, X. P. Lu, A. F. Sprecher, Effect of electric current pulses on fatigue characteristics of polycrystalline copper, Materials Science and Engineering: A. 145 (1991) 1–12. https://doi.org/10.1016/0921-5093(91)90290-4.

[12] J. Jung, Y. Ju, Y. Morita, Y. Toku, Enhancement of fatigue life of aluminum alloy affected by the density of pulsed electric current, International Journal of Fatigue. 103 (2017) 419–425. https://doi.org/10.1016/j.ijfatigue.2017.06.021.

[13] Y. Tang, A. Hosoi, Y. Iwase, Y. Ju, Effect of high-density electric current on the

microstructure and fatigue crack initiation of stainless steel, Materials Transactions. 54 (2013) 2085–2092. https://doi.org/10.2320/matertrans.M2013198.

[14] H. Conrad, Effects of electric current on solid state phase transformations in metals, Materials Science and Engineering: A. 287 (2000) 227–237. https://doi.org/10.1016/S0921-5093(00)00780-2.

[15] H. Conrad, N. Karam, S. Mannan, Effect of electric current pulses on the recrystallization of copper, Scripta Metallurgica. 17 (1983) 411–416. https://doi.org/10.1016/0036-9748(83)90183-7.

[16] H. B. Huntington, A. R. Grone, Current-induced marker motion in gold wires, Journal of Physics and Chemistry of Solids. 20 (1961) 76–87. https://doi.org/10.1016/0022-3697(61)90138-X.

[17] K. N. Smith, A stress-strain function for the fatigue of metals, Journal of Materials. 5 (1970) 767-778.

[18] J. Colin, A. Fatemi, S. Taheri, Fatigue behavior of stainless steel 304L including strain hardening, prestraining, and mean stress effects, Journal of Engineering Materials and Technology. 132 (2010) 021008. https://doi.org/10.1115/1.4000224.

[19] J. Colin, A. Fatemi, Variable amplitude cyclic deformation and fatigue behaviour of stainless steel 304L including step, periodic, and random loadings, Fatigue & Fracture of Engineering Materials & Structures. 33 (2010) 205–220. https://doi.org/10.1111/j.1460-2695.2009.01429.x.

[20] M. Kamaya, M. Kawakubo, Strain-based modeling of fatigue crack growth – an experimental approach for stainless steel, International Journal of Fatigue. 44 (2012) 131–140. http://dx.doi.org/10.1016/j.ijfatigue.2012.05.006.

[21] M. Kamaya, M. Kawakubo, Mean stress effect on fatigue strength of stainless steel,

International Journal of Fatigue. 74 (2015) 20–29. https://doi.org/10.1016/j.ijfatigue.2014.12.006.

[22] M. Kamaya, Influence of strain range on fatigue life reduction of stainless steel in PWR primary water, Fatigue & Fracture of Engineering Materials & Structures. 40 (2017) 2194–2203. https://doi.org/10.1111/ffe.12650.

[23] S. K. Koh, R. I. Stephens, Mean stress effects on low cycle fatigue for a high strength steel, Fatigue & Fracture of Engineering Materials and Structures. 14 (1991) 413–428. https://doi.org/10.1111/j.1460-2695.1991.tb00672.x

[24] H. Cai, A. J. McEvily, On striations and fatigue crack growth in 1018 steel, Materials Science and Engineering: A. 314 (2001) 86–89. https://doi.org/10.1016/S0921-5093(00)01925-0.

[25] Y. Ogawa, D. Birenis, H. Matsunaga, O. Takakuwa, J. Yamabe, Ø. Prytz, The role of intergranular fracture on hydrogen-assisted fatigue crack propagation in pure iron at a low stress intensity range, Materials Science and Engineering: A. 733 (2018) 316–328. https://doi.org/10.1016/j.msea.2018.07.014.

[26] A. J. McEvily, H. Matsunaga, On fatigue striations, Transaction B: Mechanical Engineering. 17 (2010) 75-82.

[27] Y. Uchida, M. Shimojo, Y. Higo, Relationship between fatigue striation height and stress ratio, Journal of Materials Science. 34 (1999) 2411-2419. https://doi.org/10.1023/A:1004510615621.

[28] R. O. Ritchie, Mechanisms of fatigue-crack propagation in ductile and brittle solids, International Journal of Fracture. 100 (1999) 55-83.

[29] D. Ye, S. Matsuoka, N. Nagashima, N. Suzuki, The low-cycle fatigue, deformation and final fracture behaviour of an austenitic stainless steel, Materials Science and

Engineering: A. 415 (2006) 104–117. https://doi.org/10.1016/j.msea.2005.09.081.

[30] R. Kishor, L. Sahu, K. Dutta, A. K. Mondal, Assessment of dislocation density in asymmetrically cyclic loaded non-conventional stainless steel using X-ray diffraction profile analysis, Materials Science and Engineering: A. 598 (2014) 299–303. https://doi.org/10.1016/j.msea.2014.01.043.

[31] A. K. De, D. C. Murdock, M. C. Mataya, J. G. Speer, D. K. Matlock, Quantitative measurement of deformation-induced martensite in 304 stainless steel by X-ray diffraction, Scripta Materialia 50 (2004) 1445–1449. https://doi.org/10.1016/j.scriptamat.2004.03.011.

[32] S. G. S. Raman, K. A. Padmanabhan, Effect of prior cold work on the room-temperature low-cycle fatigue behaviour of AISI 304LN stainless steel, International Journal of Fatigue. 18 (1996) 71–79. https://doi.org/10.1016/0142-1123(95)00078- X.

Chapter 6 Fatigue crack healing based on crack-tip temperature-controlled method

This chapter was dedicated to investigating the fatigue crack healing process through multiple HDPECs under the crack tip temperature-controlled method. In chapter 4, the improvement of tensile properties was successfully demonstrated with the temperature-controlled method. However, unlike the tensile tests, fatigue loading generally generates the initiation of cracks that lead to a propagating crack, thereby the a of the propagating crack increases as N increases. It leads to different thermal concentrations occurring near a crack tip when the application of HDPEC. In addition, the efficiency of improved fatigue properties was differentiated depending on the type of fatigue stages such as crack initiation and propagation as shown in chapter 5. Application of multiple HDPECs during crack propagation state could be deemed as the best approach. As a result of the changed a in a propagated crack, the distribution of ΔT_{J} due to the Joule heating can change remarkably near the crack and far from the crack. This causes different thermal compressive stress leading to advantageous effects such as crack closure and bridging. Herein, it has been tried that the T_{R} according to the a is measured and controlled significantly below a certain temperature. A fatigue crack healing method investigated in this chapter proposes a way to increase the effectiveness of the EWF and thermal compressive stress rather than direct thermal effects by the Joule heating.

6.1 Introduction

Crack initiation and propagation generally precede fracture of material and accompany

microstructural kinetics with a significant effect on fatigue properties [1,2]. Several parameters such as grain size, slip band, crystallographic orientation, porosity, inclusion and surface roughness influence mainly fatigue cracking behavior in most structural metals [3]. Crack initiation and early-stage crack propagation of the material strongly depend on slip character by dislocation accumulation due to repeated alternating fatigue loading [4], while crack propagation tends to rely on the crack profiles such as sharpness of crack determined by crack closure and bridging [5]. As such, different microstructure features in different unit scales can be presented to be characterized the fatigue properties.

Replacement or repair of the mechanical components by cracking is often determined through the evaluation of the cost performance aspect. Since the replacement is sometimes costly, engineers choose an easy way to repair it. Crack retardation by the arrest of cracks can be considered as repairing of the components because an increase in remaining life indicates extension of component life. Thus, several treatments have been developed to induce crack retardation by the arrest of cracks [6-8]. For example, an abrupt increase of stress concentration by overload during fatigue could make fatigue crack propagation slow owing to crack tip dulling [6]. Surface residual stress by pulsed laser peening induces retardation of crack initiation and propagation in austenitic stainless steels [7]. Drilling an artificial hole in the vicinity of a crack tip enables arresting crack propagation [8]. Nevertheless, most are indirect crack arrest methods and do not induce the resistance of crack propagation through direct modification of microstructure such as crack closure and bridging.

As introduced in chapter 1, the application of electric current in metals is relatively efficient to modify microstructures owing to the presence of EWF and Joule heating [9,10]. Based on two mechanisms, the thermal compressive stress induced by different

locational temperature gradients due to Joule heating and the dislocation motion by the EWF has been regarded as a source of the resistance of crack propagation leading to crack retardation. Crack closure, bridging and annihilation of dislocations could mainly contribute to improving fatigue properties as the effect of HDPEC [11-14]. In addition, local vanishment of slip bands could be achieved with a similar mechanism [15]. They also explained that the main factor is the thermal compressive stress and dislocation motion. Both mechanisms play an important role in the improvement of fatigue performance. To improve the efficiency of crack healing, this process needs to apply multiple HDPECs, but it accompanies surface oxidation along the crack surface due to high T_{R} by the Joule heating. How to avoid surface oxidation and maximize the efficiency are recently main interesting issues in fatigue crack healing by the application of HDPEC [16]. Further, because the ΔT_{J} depends on a/w and crack depth, fatigue crack healing by the effect of HDPEC under different crack profiles should be reported.

Thus, this chapter investigates a method to improve the quality of fatigue crack healing by the application of HDPEC under temperature control near the crack tip. A series of experiment works is organized to verify the method. Changed T_{R} by different crack profiles was first discussed. An application manner determined by the measurement of T_{R} was evaluated in terms of microstructure observation. The efficiency of fatigue crack healing in short and long cracks was examined. A series of CODs were measured to evaluate the degree of the crack closure. Characterized microstructure features near the crack tip are discussed with several effects of HDPEC. Controlled conditions of HDPEC such as j and p depend on crack profiles and play an important role in temperature-controlled fatigue crack healing. Appropriate application manners are controllable.

6.2 Investigation of temperature-controlled fatigue crack healing

The sample geometry used in this chapter was the same as shown in Fig. 2.1 of chapter 2. The notched samples were used. To determine the appropriate j and p, the T_{R} in the basic shape without a notch was first measured at the center of sample geometry using a thermal camera. Then, measurements of T_{R} via three different geometries as described in Fig. 6.1 were performed because the T_{R} can be concentrated in a shape gradient such as notch and crack tip. The measured positions are indicated by positions 1-6 as shown in Fig. 6.1. Each position was measured based on the maximum T_{R} defined by ΔT_{J}+25°C. Changed crack tip temperature rising ΔT_{ct} between position 1 (nearest the notch) and position 2 (5 mm away from the notch), ΔT_{ct} between position 3 (nearest the short crack) and position 4 (5 mm away from it) and ΔT_{ct} between position 5 (nearest the long crack) and position 6 (5 mm away from it) were calculated respectively.

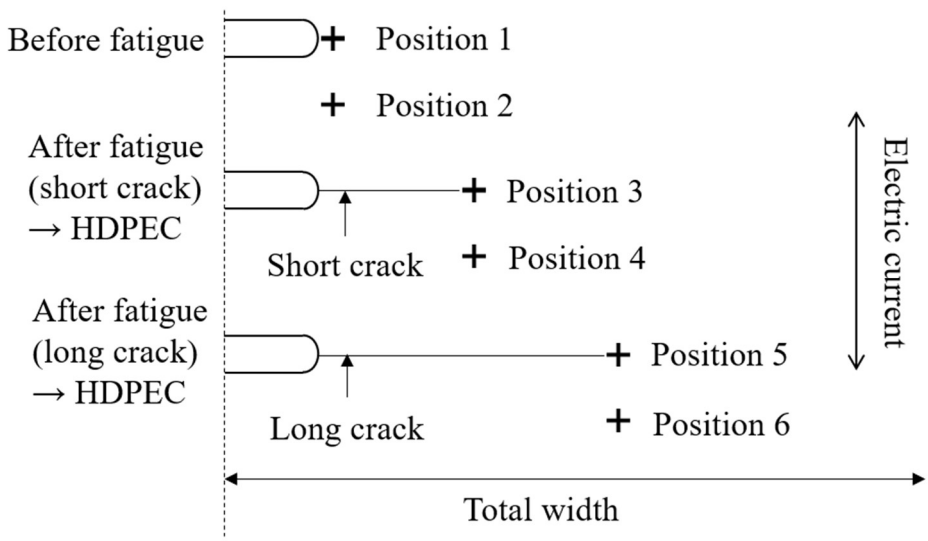

Fig. 6.1 Measured positions (+) for the determination of maximum raised temperature by the application of HDPEC.

The quality of fatigue crack healing was evaluated in terms of microstructure observation. Table 6.1 lists the applied conditions of HDPEC for different crack profiles. The effects of different p and j of HDPEC are distinguished based on the group for short crack (cases A-F) and long crack (cases I-V). The p of HDPEC was limited to 10 times or less, and it was completely cooled reaching T_{r} before the next HDPEC application. Microstructural evolution in the same locations was observed using FESEM. EDS was purposely used to demonstrate the elemental changes along with surface fatigue cracks.

Table 6.1 Applied conditions of HDPEC for short and long cracks.

Group	**Case**	**Density (j), A/mm^2**	**Duration time (t_{d}), ms**	**The number of pulses (p), times**	**Type of cooling between pulses**
Short crack	A	-	-	-	-
	B	200	5	1	Reach to room temperature
	C	200	5	4	
	D	200	5	7	
	E	200	5	10	
	F	400	5	1	
Long crack	I	-	-	-	-
	II	200	5	1	Reach to room temperature
	III	200	5	4	
	IV	200	5	7	
	V	200	5	10	

Table 6.2 Fatigue test conditions for making pre-cracks such as short and long cracks.

Case	f (Hz)	R	N_s	σ_{max} (MPa)	σ_s (MPa)	a (m)	a/w	K_c (MPa·m$^{1/2}$)
A-F	10	0.5	1.28×10^4	247	186	0.00186	0.258	15.92
I-VI			1.81×10^4	249	150	0.00301	0.418	16.33

To make the short and long cracks, strain-controlled fatigue tests were performed as listed in Table 6.2. The f and R remain constant. Fatigue loading was stopped after making a crack profile of $a/w = 0.258$ for the short crack and that of $a/w = 0.418$ for the long crack. At stop cycles N_s, stress at fatigue stop σ_s and σ_{max} were measured. The K_c under fatigue loading can be defined by $K_c = \alpha\sigma_s\sqrt{\pi a}$ [17]. Where α was added as 1.12 for geometrical correction. a/w of ≥ 0.5 was not taken into account because the crack propagation over half-crack length progresses unexpectedly quick and is regarded as close to failure in the analysis of the crack propagation.

6.3 Results

6.3.1 Measured raised temperature

Figure 6.2 shows the variation of maximum T_R and ΔT_{ct} with respect to the p of HDPEC. Based on geometry without the notch, the ΔT_J without thermal gradient was considered. The plotted lines of Fig. 6.2 (a) and (b), which are theoretical and steadily T_R by Joule-heating equation of Eq. (1.11) in chapter 1, were compared with experimental measurements of the maximum T_R. The values of ΔT_J were estimated with the constants of the material, i.e., $\rho = 7.4\times10^{-7}\ \Omega\cdot\mathrm{m}$, $C_p = 502\ \mathrm{J/(kg\ K)}$ and $d_m = 7.87\times10^3\ \mathrm{kg/m^3}$. In Fig. 6.2 (a), the j of 300 A/mm^2 and 400 A/mm^2 results in a significant increase of maximum T_R due to one or two pulse applications. On the other hand, for the j of 200

A/mm^2, the maximum T_R was controlled even multiple HDPEC was applied. In addition, in Fig. 6.2 (b), it seems that the maximum T_R was greatly affected by the cooling time between pulses. The cooling time increases as the effect of controlled temperature increases. Especially, a stop time of approximately 40 sec between pulses leads to complete cooling conditions. In Fig. 6.2 (c), the maximum T_R calculated by the positions described in Fig. 6.1 was plotted to explain the degree of thermal compressive stress due to both the presence or absence of cracks and the crack profiles such as short and long cracks. In the shape without cracks, there was not much temperature difference enough to cause thermal compressive stress, but as the a was increased, the maximum T_R between the crack tips and the positions 5 mm far from the crack tip was increased. In addition, when continuous pulses with a cooling time of 1 sec were applied, the ΔT_{ct} between positions contributing to the thermal compressive stress was reduced. This means that the thermal compressive stress can be maximized by the first pulse application. Figure 6.2 (d) supports the results presented in Fig. 6.2 (c). The relationship between the ΔT_{ct} associated with the crack length and the p of HDPEC. Certainly, any shape can produce a greater ΔT_{ct} related to thermal compressive stress in the first application of HDPEC, i.e., it was evaluated that it was better to apply a single pulse under an appropriate j for thermal compressive stress that promotes fatigue crack healing. Further, surface oxidation due to maximum T_R in the material can occur at approximately 300°C. Based on the results expected in Fig. 6.2, it could be deemed that applying a single pulse under the j of 200 A/mm^2 can maximize thermal compressive stress while preventing surface oxidation regardless of a/w. Thus, the crack tip temperature-controlled method used in this chapter is determined as the application manner that applies the next multiple pulses through complete cooling under a single pulse application with the j of 200 A/mm^2.

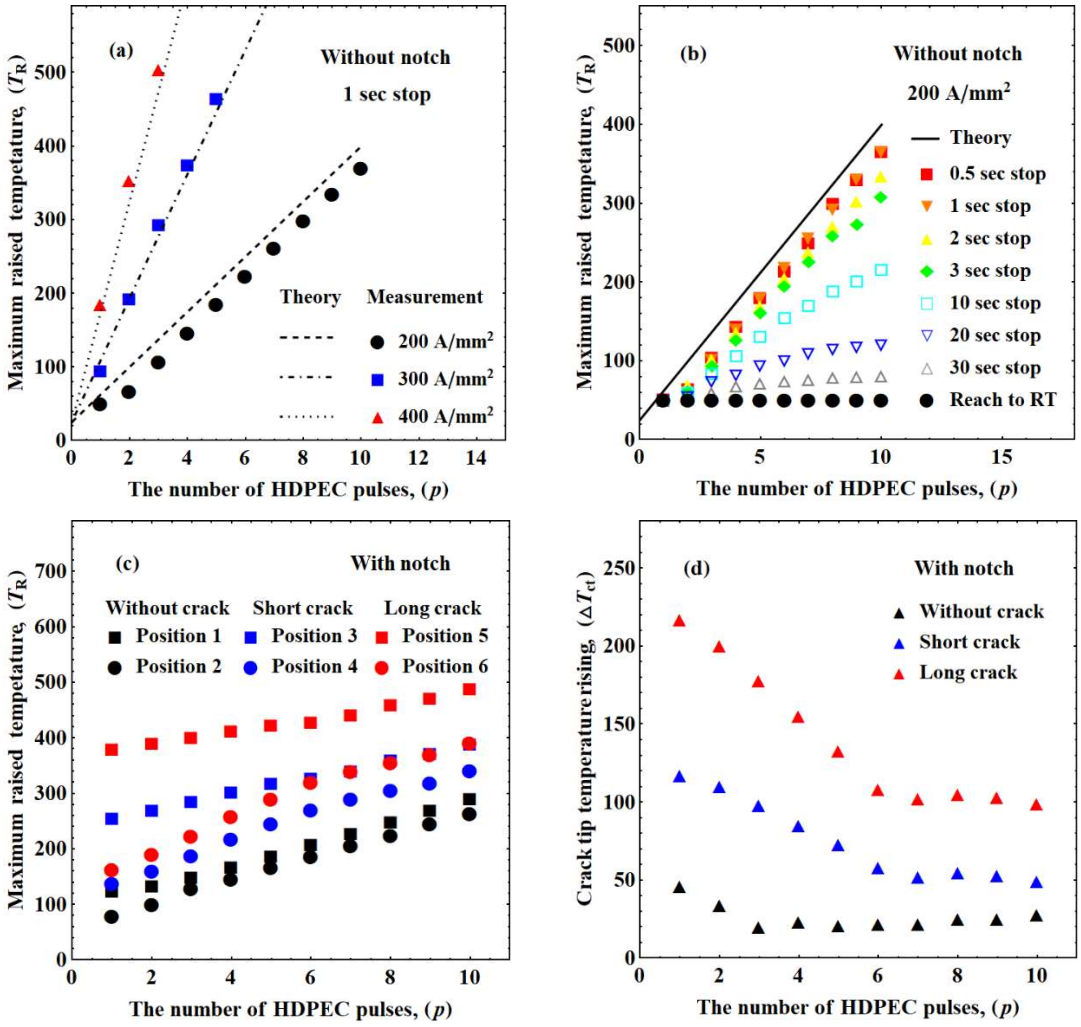

Fig. 6.2 Variation of temperature rising depending on sample profiles, (a) maximum raised temperature versus the number of HDPEC pulses based on HDPEC density in the geometry without the notch, (b) that based on stop time between two consecutive pulses, (c) maximum raised temperature versus the number of HDPEC pulses in the geometry with notch excluding a crack and with notch including short and long cracks and (d) variation of crack tip temperature rising in the geometry of (c).

6.3.2 Fatigue crack healing

Figure 6.3 illustrates the FESEM results in fatigue crack healing based on the application manner proposed by the results in Fig. 6.2. The microstructure observation for the p of

multiple HDPECs listed in Table 6.1 was performed by applying every single pulse after complete cooling. Based on the untreated sample of Fig. 6.3 (a) (case A), it is revealed that the fatigue cracks were healed gradually by increasing the p of HDPEC (Fig. 6.3 (b) and (c)). In enlarged FESEM images of Fig. 6.3 (d, e, and f), the degree of the healing quality of the crack tip is shown. When the p of HDPEC applications is high, fatigue crack healing is strong.

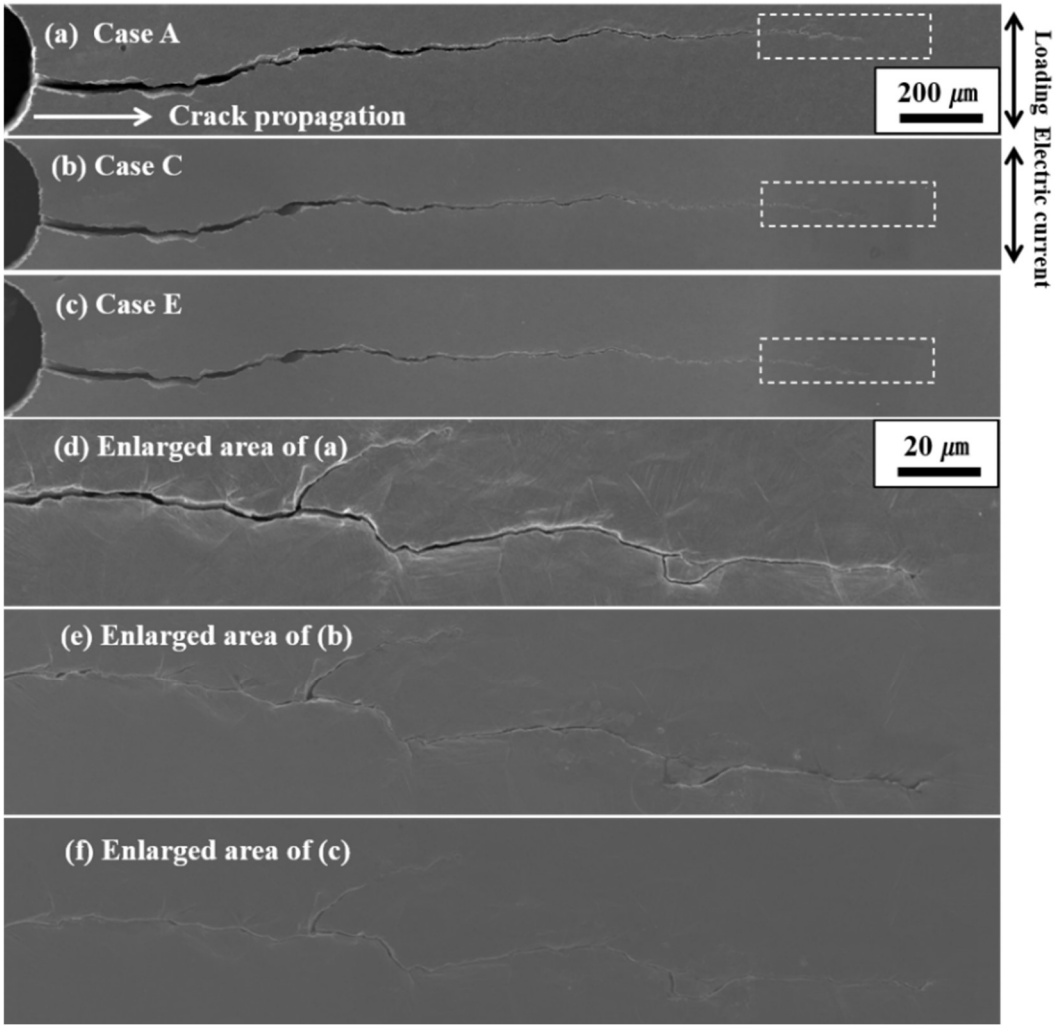

Fig. 6.3 FESEM images of fatigue crack healing, (a) untreated sample (case A), (b) after HDPEC treatment of four pulses under 200 A/mm^2 (case C), (c) that after ten pulses (case E), (d) enlarged images of (a), (e) that of (b) and (f) that of (c).

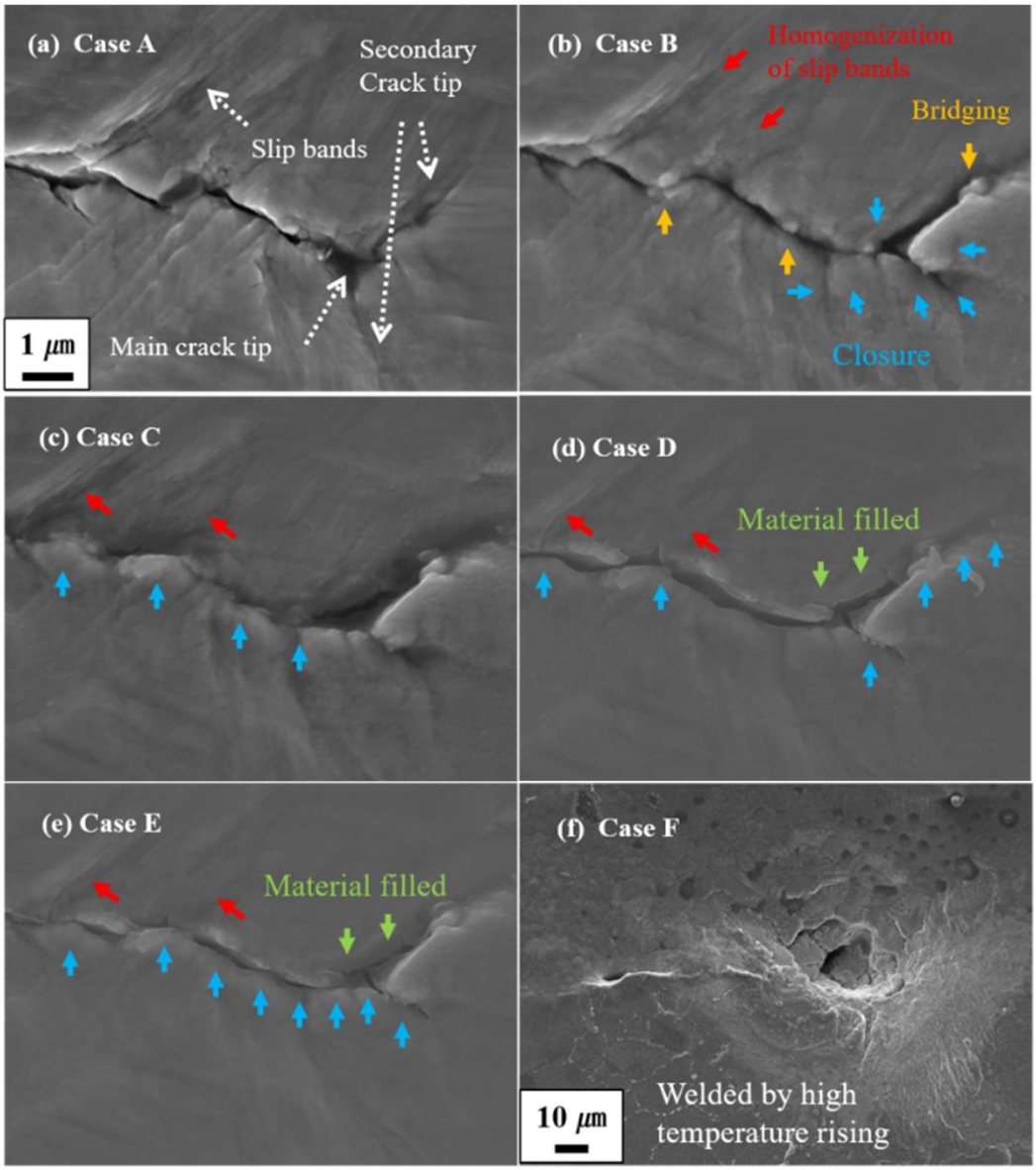

Fig. 6.4 FESEM images of fatigue crack healing near the crack tip, (a) untreated sample (case A), (b) after HDPEC treatment of one pulse under 200 A/mm^2 (case B), (c) that after four pulses (case C), (d) that after seven pulses (case D), (e) that after ten pulses (case E) and (f) that by one pulse of 400 A/mm^2 (case F).

A series of FESEM images for the fatigue crack healing in the vicinity of the crack tip is shown in Fig. 6.4. In Fig. 6.4 (a-e), the main crack closure, the partial bridging, the

secondary crack healing, the homogenization of slip bands and the filling material at the main crack tip were featured. Interestingly, a single pulse condition, which is a crack tip temperature-controlled condition, could make the changed crack profile as shown in Fig. 6.4 (b). Not only did the shape of the main crack tip significantly change but also bridging at the secondary crack tip was revealed. Notably, the homogenization in fatigue slip bands increases also as the p of HDPEC increases. In Fig. 6.4 (e), material migration at the main crack, which has a maximum size of ≈ 800 nm, leads to filling material between crack faces by increasing the p of HDPEC. These features near the crack tip can be thought of owing to the thermal compressive stress and the EWF. It plays an important role in temperature-controlled fatigue crack healing. However, in Fig. 6.4 (f), significant welding near the crack tip occurred due to the high T_R by the j of 400 A/mm^2. Severe partial recrystallization together with creating intermetallic compounds was shown near the pre-existing crack tip. That is, although the crack was partially welded, irregularity according to the location was appeared. This kind of irregularity cannot be thought that it will be improved microstructure feature as the advantage of HDPEC.

In Fig. 6.5, a series of COD profiles was measured based on FESEM images of short crack (cases A-E) and long crack (cases I-V). The evolution of healed CODs at the half crack length is plotted in the inset figure of Fig. 6.5. In cases of the short crack, the degree of crack closure increases and the COD decreases as the effect of the increased p of HDPEC. In cases of long crack, on the other hand, crack closure by the effect of the increased p of HDPEC was not efficiently achieved. Uniquely, Case II applied by one pulse exhibits a decrease in COD at half-crack but applying more than that p opens the crack further. The effect of multiple HDPECs was not efficiently valid.

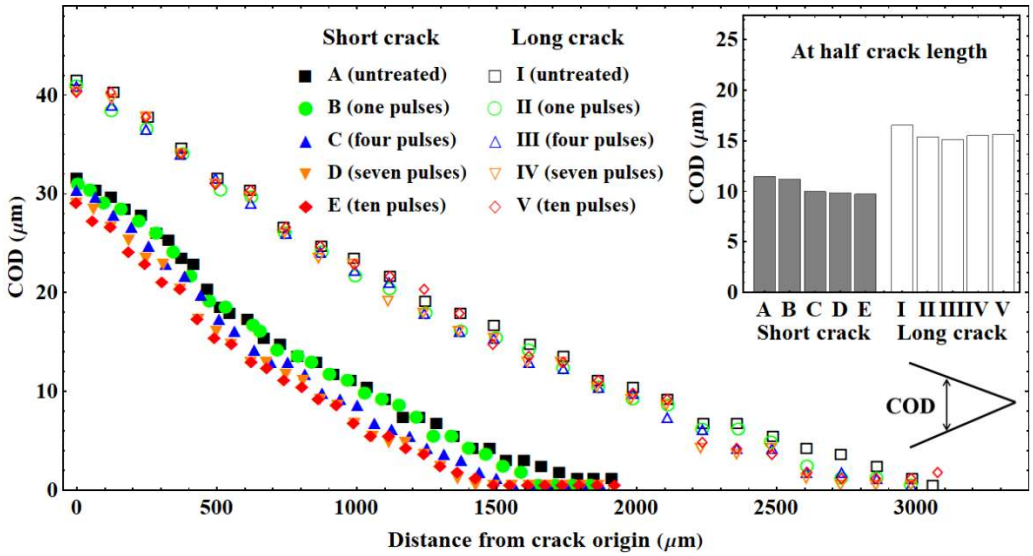

Fig. 6.5 A series of COD profiles measured by FESEM images for short (A-E) and long (I-V) cracks. Inset: evolution of measured CODs at half crack length.

The reason for the presented results in Fig. 6.5 can be explained by Fig. 6.6. As the p of HDPEC increases, crack closure by thermal compressive stress could not be properly affected in-between crack faces as shown in Fig. 6.6 (a-c). It can be thought that the locational irregularity along with the crack faces could occur due to reverse compressive stress, i.e., multiple applications of HDPEC in long crack could make different thermal compressive forces in different locations along with crack, thereby fatigue crack healing could not efficiently be achieved, and it can lead to the adverse effect of fatigue properties. In addition, even at short cracks, locational irregularity appears as shown in Fig. 6.4 (f) and Fig. 6.6 (d) when overflowing j is applied. It can be explained with a recent report. Even at the crack initiation stage, which has less temperature concentration, excessive j could not improve the fatigue properties of aluminum alloy [18]. The present results suggest that it is important to design the conditions of HDPEC. The conditions such as an appropriate manner, j and p of HDPEC can be regarded as adjustable factors to improve the quality of fatigue crack healing based on crack profiles.

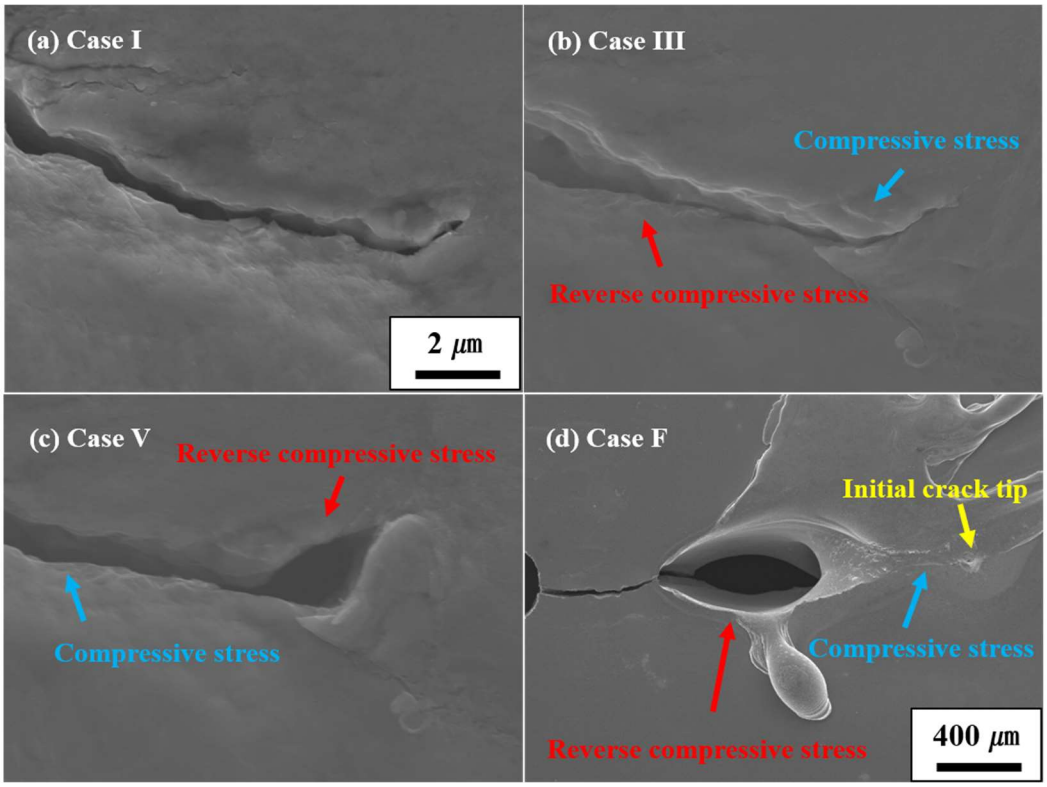

Fig. 6.6 Locational irregularity due to over-application of HDPEC. (a) FESEM image of the untreated sample having a long crack, (b) that after four pulses, (c) that after ten pulses and (d) presence of locational irregularity in short crack by over-application of the density of HDPEC.

Figure. 6.7 presents the EDS results for the elemental irregularity of short crack due to the over-application of the j of HDPEC. Main elements of this material such as Fe, Cr, Ni, Mn, Mo and Si were analyzed. In Fig. 4 (a), the application of a single pulse of HDPEC with the j of 200 A/mm^2 (case B) did not show creating intermetallic compounds, and the recrystallization because the T_R near the crack tip was not reached. A stable fatigue crack healing owing to thermal compressive stress and the EWF can be expected. Case F, on the other hand, became a severe elemental rearrangement due to high T_R by the j of 400 A/mm^2 and allowing the material to be recrystallized only with a single pulse.

That is, irregularities of major alloy compositions such as Fe, Cr, Ni, Mn, Mo and Si were revealed and would result in creating intermetallic compounds. It is certainly due to a sudden high T_R and a state rapidly cooled to T_r near the crack tip. Creating intermetallic compounds from alloys due to elemental rearrangement can adversely affect the successful fatigue crack healing of the material.

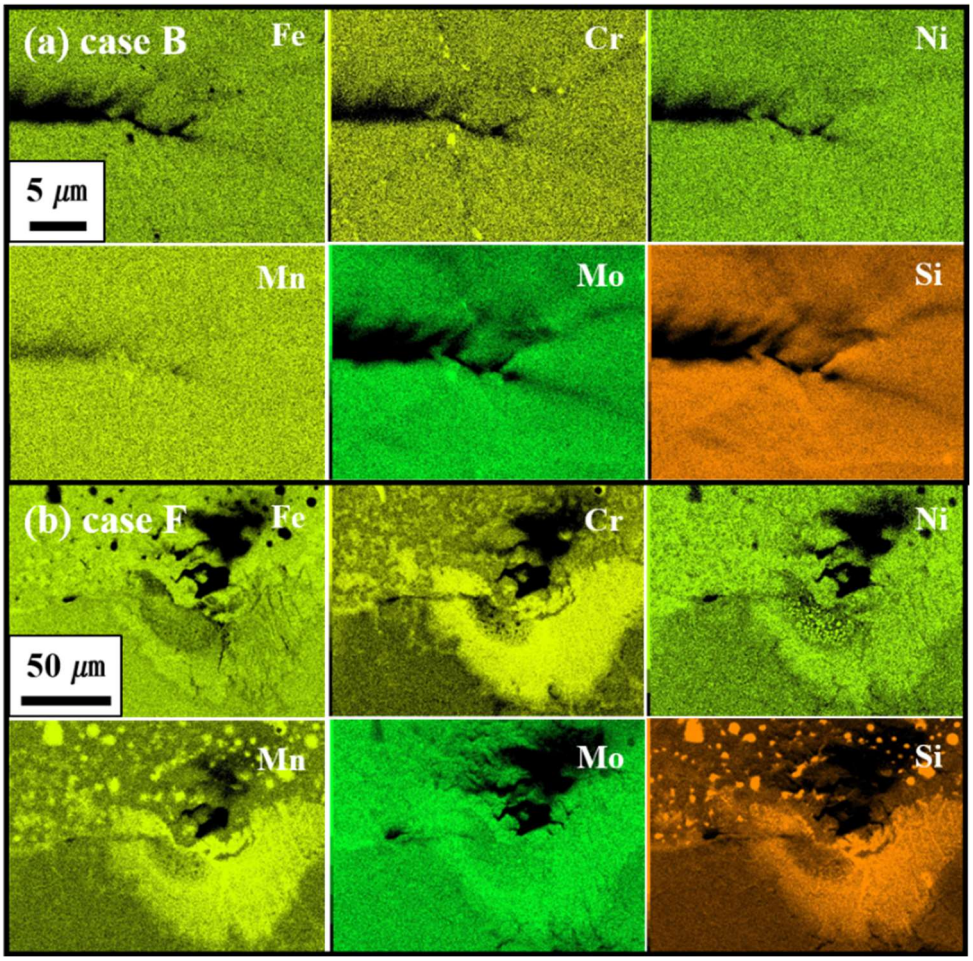

Fig. 6.7 Elemental rearrangement, (a) after one pulse of 200 A/mm^2 (case B) and (b) after one pulse of 400 A/mm^2 (case F).

6.3.3 Evaluation of efficiency of fatigue crack healing

Based on the changed COD by multiple applications of HDPEC, the efficiency of fatigue crack healing was evaluated as shown in Fig. 6.8. Each crack area was obtained by direct measurement from FESEM images. The obtained crack area could give the efficiency of fatigue crack healing, i.e., using a percentage ratio (%) based on the reduced crack area compared to the area of the untreated crack. In the inset figure of Fig. 6.8, the closure ratios at half a were calculated by the obtained COD profiles. Both the plotted crack healing ratios were gradually increased in the group of short crack, while the efficiency of long crack decreased after one pulse application.

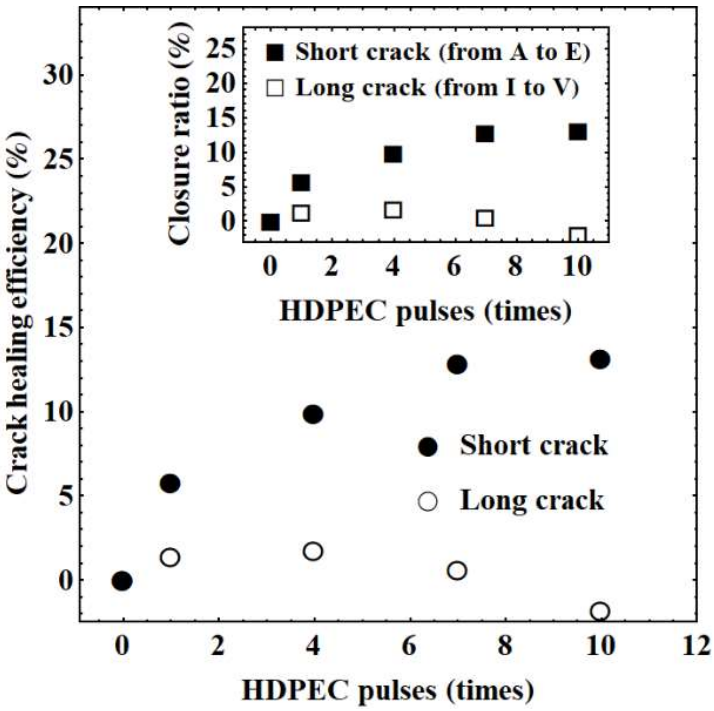

Fig. 6.8 Efficiency of fatigue crack healing as a function of the number of multiple HDPECs. Inset: crack closure ratio versus the number of multiple HDPECs based on the evolution of COD at half crack length.

Even in the case of short crack, it has been found that too many applications of HDPEC show a decrease in the efficiency of fatigue crack healing. This once again reminds us of the disadvantage of excessive application of HDPEC. If too many p are applied or too high j is applied, it is judged that it will show low efficiency or disadvantages compared with appropriate conditions of HDPEC.

6.4 Discussion

6.4.1 Microstructure features

The main point of the temperature-controlled method investigated in this chapter is to realize simultaneously the improved efficiency and the high-quality fatigue crack healing. In general, it is desirable to maintain an appearance other than a crack before the application of HDPEC rather than specific adverse effects by HDPEC, such as surface oxidation. Based on the HDPEC conditions proposed by the temperature measurements shown in Fig. 6.2, the method presented in this chapter could make the advanced fatigue crack healing. Especially, the microstructure features near the crack tip were revealed that crack closure, partial bridging, secondary crack healing, homogenization of slip bands and filling material between crack faces could be presented, thereby can give an improvement of fatigue properties. Under the investigated application manner and short crack profiles, when the p of HDPEC is high, fatigue crack healing is strong. On the other hand, an overflowing j of HDPEC can cause severe partial recrystallization together with creating intermetallic compounds, as well as an over-application of the p can make a decrease in the efficiency of fatigue crack healing, which depends on crack profiles.

6.4.2 Efficiency of fatigue crack healing

It was experimented and verified to understand what the presented results mean according to the crack profiles. If multiple p of HDPEC were applied to the fatigue crack under the condition that the maximum T_{R} was controlled below a certain temperature. It has been found that it is efficient to allow from applying multiple HDPECs if the crack is short, while multiple pulses more than one pulse have refrained if the crack length is long. This can be inferred from the temperature measurement results of sub-chapter 6.3.1. In different shapes in the notch and cracks, it was found that the long crack had a more severe thermal gradient under the same HDPEC condition than that of a short crack. The potential to have multiple p of HDPEC in a crack depends strongly on crack profiles. In terms of the efficiency of fatigue crack healing, it is recommended for a short crack, while it is better to refrain from a long crack.

6.4.3 Irregularity from over-application of HDPEC

In any crack profile, the locational irregularities appear when the j and/or p of HDPEC are excessively applied. In general, it is preferable to induce uniform fatigue crack healing along the crack faces. The j of 200 A/mm^2 proposed in this chapter would be fine if only one pulse was applied in any crack profiles, but multiple p of HDPEC would result in shape constraints, higher shape constraints such as long crack could make the high irregularity of fatigue crack healing. In addition, the formation of intermetallic compounds occurs near the crack tip when excessive j is applied. This never benefits fatigue properties. Adjusting the appropriate j and p of HDPEC in a given crack profile is necessary for optimized fatigue crack healing.

6.5 Summary

A series of experimental works was performed to be proposed high-quality fatigue crack healing by the crack tip temperature-controlled method. High-quality fatigue crack healing was achieved under specific HDPEC conditions and crack profiles. The results presented in this chapter can be summarized as follows: First, the j of 200 A/mm^2 and a single pulse application can be deemed as the best condition in any crack length within $a/w \leq 0.418$. Multiple p of HDPEC at the same place is limited to the short crack within $a/w = 0.258$. The shorter the crack profile, the stronger condition of HDPEC is required, and the longer the crack profile, the weaker condition of HDPEC is recommended. Second, the microstructure features near the tip of the short crack shows crack closure, partial bridging, secondary crack healing, homogenization of slip bands and filling material. These features can play a positive role in the improvement of fatigue properties. The potentiality of multiple p of HDPEC depends strongly on crack profiles. The method, which is that the maximum T_{R} was controlled below a certain temperature, can contribute to optimizing thermal compressive stress leading to the efficiency of fatigue crack healing. Finally, the locational irregularities appear when the over-application of j and p is applied. Abruptly increased and rapidly cooled temperature with a shape gradient will be expected the effect of HDPEC application. Strong effects are good when a shape gradient is weak, but restrained and controlled application manners are also important to promise high-quality fatigue crack healing. In order to apply this method in industrial sites, sometimes, a simpler but relatively enough efficient method is recommended than the most strong method for improving fatigue properties. Whether it is optimized efficiency or cost performance in a simple manner will be an option for engineers.

References

[1] D. Taylor, J. F. Knott, Fatigue crack propagation behavior of short cracks; the effect of microstructure, Fatigue & Fracture of Engineering Materials & Structures. 4 (1981) 147–155. https://doi.org/10.1111/j.1460-2695.1981.tb01116.x.

[2] K. Nakajima, T. Terao, T. Miyata, The effect of microstructure on fatigue crack propagation of α+β titanium alloys; In-situ observation of short fatigue crack growth, Materials Science and Engineering A. 243 (1998) 176–181. https://doi.org/10.1016/S0921-5093(97)00797-1.

[3] K. S. Chan, Roles of microstructure in fatigue crack initiation, International Journal of Fatigue. 32 (2010) 1428–1447. https://doi.org/10.1016/j.ijfatigue.2009.10.005.

[4] V. Mazánová, J. Polák, Initiation and growth of short fatigue cracks in austenitic Sanicro 25 steel, Fatigue & Fracture of Engineering Materials & Structures. 41 (2018) 1529–1545. https://doi.org/10.1111/ffe.12794.

[5] R. O. Ritchie, Mechanisms of fatigue-crack propagation in ductile and brittle solids, International Journal of Fracture. 100 (1999) 55–83. https://doi.org/10.1023/A:1018655917051.

[6] E. Salvati, S. O'Connor, T. Sui, D. Nowell, A. M. Korsunsky, A study of overload effect on fatigue crack propagation using EBSD, FIB–DIC and FEM methods, Engineering Fracture Mechanics. 167 (2016) 210–223. https://doi.org/10.1016/j.engfracmech.2016.04.034.

[7] Y. Sano, M. Obata, T. Kubo, N. Mukai, M. Yoda, K. Masaki, Y. Ochi, Retardation of crack initiation and growth in austenitic stainless steels by laser peening without protective coating, Materials Science and Engineering: A. 417 (2006) 334–340. https://doi.org/10.1016/j.msea.2005.11.017.

[8] S. M. J. Razavi, M. R. Ayatollahi, C. Sommitsch, C. Moser, Retardation of fatigue crack growth in high strength steel S690 using a modified stop-hole technique, Engineering Fracture Mechanics. 169 (2017) 226–237. https://doi.org/10.1016/j.engfracmech.2016.11.013.

[9] H. B. Huntington, A. R. Grone, Current-induced marker motion in gold wires, Journal of Physics and Chemistry of Solids. 20 (1961) 76–87. https://doi.org/10.1016/0022-3697(61)90138-X.

[10] H. Conrad, Electroplasticity in metals and ceramics, Materials Science and Engineering A. 12 (2000) 276–287. https://doi.org/10.1016/S0921-5093(00)00786-3.

[11] A. Hosoi, T. Nagahama, Y. Ju, Fatigue crack healing by a controlled high density electric current field, Materials Science and Engineering: A. 533 (2012) 38–42. https://doi.org/10.1016/j.msea.2011.11.024.

[12] A. Hosoi, T. Yano, Y. Morita, Y. Ju, Quantitative evaluation of the displacement distribution and stress intensity factor of fatigue cracks healed by a controlled high-density electric current field, Fatigue & Fracture of Engineering Materials & Structures. 37 (2014) 1025–1033. https://doi.org/10.1111/ffe.12175.

[13] Y. Tang, A. Hosoi, Y. Iwase, Y. Ju, Effect of High-density electric current on the microstructure and fatigue crack initiation of stainless steel, Materials Transactions. 54 (2013) 2085–2092. https://doi.org/10.2320/matertrans.M2013198.

[14] Y. Tang, A. Hosoi, Y. Morita, Y. Ju, Restoration of fatigue damage in stainless steel by high-density electric current, International Journal of Fatigue. 56 (2013) 69–74. https://doi.org/10.1016/j.ijfatigue.2013.08.012.

[15] X. Suhong, Z. Yizhou, G. Jingdong, The effect of high current pulsing on persistent slip bands in fatigued copper single crystals, Materials Science and Engineering: A. 332

(2002) 351–355. https://doi.org/10.1016/S0921-5093(01)01822-6.

[16] A. Hosoi, T. Kishi, Y. Ju, Healing of fatigue crack by high-density electropulsing in austenitic stainless steel treated with the surface-activated pre-coating, Materials. 6 (2013) 4213–4225. https://doi.org/10.3390/ma6094213.

[17] R. I. Stephens, A. Fatemi, R. R. Stephens and H. O. Fuchs: *Metal fatigue in engineering*, (John Wiley & Sons, New York, 2000).

[18] J. Jung, Y. Ju, Y. Morita, Y. Toku, Enhancement of fatigue life of aluminum alloy affected by the density of pulsed electric current, International Journal of Fatigue. 103 (2017) 419–425. https://doi.org/10.1016/j.ijfatigue.2017.06.021.

Chapter 7 Conclusions

Type 316 austenitic stainless steel is the most widely used steel in various industrial applications such as chemical vessel and piping, power engineering, building construction, etc. In this material, in contrast to excellent anti-corrosion and cost-performance, improvements in tensile strength and fatigue properties have been required but it has not been easily achieved. In that sense, the improvement ways by HDPEC application presented in this thesis is a promising method to replace conventional methods introduced in chapter 1.

This dissertation has been elaborated to aim to establish and evaluate the improvement of mechanical properties using the HDPEC. Experimental, theoretical and simulation approaches have been purposely used to verify such improvements. The main assumption of material modification is considered to be due to the effect of EWF but not the raised temperature induced by Joule heating. If there is no EWF and pulse effects induced by an abruptly increased voltage, this assumption may be useless and the effect of temperature rising should be considered. The results shown in this thesis reasonably verify the assumption. Based on the conclusions described below, the advantages of the HDPEC treatment method are emphasized.

1. In chapter 3, based on a combination of fracture mechanics and FEA, the improvement of fracture characteristics was assessed. The yield stress was increased and the strain hardening exponent was decreased with the increased HDPEC density. The application of HDPEC could give advantages to resist crack propagation subjected to tensile loading owing to the modified mechanical properties. The

improvements of local fracture strength near the crack tip, fracture toughness and critical CTOD were achieved. The increased density and number of HDPEC pulses made it efficient.

2. Based on the tensile behavior presented in chapter 3, strengthening mechanisms of the material as the effect of HDPEC under controlled temperature rising was established in chapter 4. Modification of the GB characteristics and the elemental kinetics were discussed. Interestingly, the partial grain refinement could increase the strength of the material whereas the dissolution of $Cr_{23}C_6$ could prevent a decrease in their ductility, thereby improving simultaneously the yield stress and strain at fracture. The strength-ductility trade-off could be overcome owing to the enhanced role of EWF instead of a thermally activated process.
3. In chapter 5, the improvement of the LCF life in the material was achieved. Multiple applications of HDPEC during fatigue were the best approach for the improvement of LCF properties. Increasing the number of multiple HDPECs and controlling the application timing during the crack propagation stage could significantly lead to high effectiveness in the improvement of the LCF life under the same application number of HDPECs. More strong ductile striations in the fatigue fracture surface were observed than those without HDPEC. The effect of multiple HDPECs could contribute to increasing the degree of ductility owing to the annihilation of dislocations, thereby increasing the LCF life.
4. In chapter 6, the application manner under the temperature-controlled method was proposed to ensure high-quality fatigue crack healing. High-quality fatigue crack healing was achieved under specific HDPEC conditions and crack profiles. The shorter the crack length, the stronger the application condition of HDPEC is required,

on the other hand, the longer the crack length, the weaker condition of HDPEC is recommended. The microstructure features near the tip of the short crack show successfully the crack closure, the partial bridging, the secondary crack healing, the homogenization of slip bands and the filling material. These features can play an important role in fatigue crack healing. The presented application manner under an appropriate crack profile can contribute to improving the efficiency of fatigue crack healing. Abruptly increased and rapidly cooled temperature with a shape gradient will be the expected effect of HDPEC application.

Finally, the conclusions listed above describe the advantages of HDPEC treatment for the improvement of tensile and fatigue properties. A series of microstructural advantages were simultaneously proposed. It can not only overcome the relatively low tensile strength, which is a typical disadvantage of this material, but also contributes to struggling microstructural disadvantages. This method has a good cost performance and can also be easily applied to industrial sites. Further, it can be a post-processing method used for running mechanical components. However, it remains still difficult to fully understand a series of complex phenomena associated with various factors. Therefore, it is believed that the presented method must be interestingly dealt with a wide range of materials, structural responses and application methods.

Acknowledgements

First of all, I would like to sincerely express my greatest gratitude to my principal supervisor, Professor Yang Ju. He allowed me an opportunity for my Ph.D. course and gave also me generous support academically and economically for research work and living in Japan. He also gave me research guidance to establish a diligent attitude and research philosophy. In addition, he warmly and unlimitedly embraced my special family state as a Ph.D. student.

I would like to also sincerely and deeply appreciate Professor Koji Mizuno for his time and suggestions in this dissertation. Also, I express my greatest thanks to Professor Atsushi Hosoi of Waseda University for providing his time and advice in this thesis.

In addition, I sincerely express my greatest gratitude to Senior lecturer Yuhki Toku. He guided me in the best direction of what research topic I should go to organize my doctoral thesis well, thereby the direction could make storytelling in my thesis. Further, I express my greatest thanks to him because his help made me smooth in laboratory works.

I would like to also express my greatest appreciation to Assistant professor Yasuhiro Kimura. He is known to guide all students well at the closest distance and cares for international students. In particular, he taught me a lot of research philosophy and detailed research skills. In addition, I express my greatest thanks to him because I have done important experiments under his guidance.

I deeply appreciate Assistant professor Yi Cui. His fruitful and experienced comments were always helpful and insightful. He provided new research trends and highlight news from the research community. I thank also my colleagues, Mr. Shaojie Gu, Mr. Rui Iwase, Mr. Yuki Marumoto and all other members. Research and group activities with them were

enjoyable. I learned different but similarly interesting cultures among the three countries.

Further, I would like to express deep appreciation to my previous supervisors, Professor Yunhae Kim and Emeritus Professor Changmin Suh. Especially, I appreciate Professor Yunhae Kim for his long-term research and emotional supports.

Finally, above all, I must express my best appreciation to my family members, parents (Jaewook Yoon and Younghee Jung), parents-in-law (Mooyak Kim and Hyunjeong Kim), wife (Uila Kim), children (Arin Yoon and Jisan Yoon) and little brother and brother-in-law (Sangmin Yoon and Tanil Kim). I have a lot of loopholes and I am clumsy. However, when I said I will try this doctorate, I had a family who supported me with believable encouragement, thereby could start and finish this Ph.D. course. In particular, I would like to attribute all the honor to my wife, Uila Kim. You have had a hard time supporting me, taking care of our children and managing family economics. Thanks to our strong companionship, this doctoral dissertation is one of our most valuable achievements in our whole life. I also acknowledge the Japanese government (Monbukagakusho, MEXT) scholarship for supporting my doctorate study.

Fully respectfully yours, this is to all the people mentioned above.

Sungmin Yoon

Nagoya University, March, 2022